A TWO–DIMENSIONAL ELECTRON–HOLE SYSTEM UNDER THE INFLUENCE OF THE CHERN–SIMONS GAUGE FIELD CREATED BY QUANTUM POINT VORTICES

Sveatoslav A. Moskalenko[1], Vsevolod A. Moskalenko[1], Igor V. Podlesny[1], and Michael A. Liberman[2]

[1]*Institute of Applied Physics, Academiei str.5, Chisinau, MD-2028 Republic of Moldova*
[2]*Nordic* Institute *for Theoretical Physics (NORDITA) KTH and Stockholm University, Roslagstullsbacken 23, Stockholm, SE–106 91 Sweden*
E-mail: *sveatoslav.moscalenco@ifa.md, mliber@nordita.org*

Abstract

In the present work, the Chern–Simons (CS) gauge field theory developed by Jackiw and Pi [8] and widely used to interpret the fractional quantum Hall effects, is applied to describe a two-dimensional (2D) electron–hole (e–h) system in a strong perpendicular magnetic field and under the influence of quantum point vortices creating the CS gauge field. Composite particles formed by electrons and holes with equal integer positive numbers ϕ of attached quantum point vortices are described by dressed field operators, which obey the Fermi or Bose statistics depending on even or odd numbers ϕ. It is shown that the phase operators, as well as the vector and scalar potentials of the CS gauge field, depend on the difference between the electron and hole density operators. They vanish in the mean field approximation, when the average values of electron and hole densities coincide. Nevertheless, even in this case, the quantum fluctuations of the CS gauge field lead to new physics of the 2D e–h system.

Keywords: Chern–Simons gauge field, quantum point vortices, electron–hole system, two-dimensional (2D), strong magnetic field.

Rezumat

În lucrarea de față, teoria câmpului de etalonare de tip Chern–Simons (CS), dezvoltată de Jackiw și Pi [8] și pe larg utilizată pentru a explica efectele cuantice fracționale de tip Hall, a fost aplicată pentru a descrie sistemul bidimensional (2D) compus din electroni și goluri (e–h) supuse unui câmp magnetic perpendicular puternic și sub influența vârtejurilor punctiforme cuantice care creează câmpul de etalonare de tip CS. Particulele compozite formate din electroni și din goluri cu numere pozitive întregi egale ϕ de vârtejuri punctiforme cuantice atașate sunt descrise de operatorii de câmp modificați, care se supun statisticilor Fermi sau Bose în dependență de numerele pare sau impare ϕ ale vârtejurilor atașate. Operatorii, care descriu fază, precum și potențialele vectoriale și scalare ale câmpului de etalonare de tip CS depind de diferența dintre operatorii de densitate ale electronilor și golurilor. Ele se anihilează în aproximarea câmpului mediu atunci când valorile medii ale densităților electronilor și golurilor coincid. Totuși, chiar și

în acest caz, fluctuațiile cuantice ale câmpului de etalonare de tip CS aduc la noi fenomene fizice în sistemul 2D e–h.

Cuvinte cheie: câmp de etalonare Chern–Simons, vârtejuri punctiforme cuantice, sistem din electroni și goluri bidimensionali (2D), câmp magnetic puternic.

1. Introduction

The Chern–Simons (CS) theory [1] is a quantum gauge theory using which some problems can be viewed from a different point of view providing better understanding. The most prominent of these problems are the change in the statistics of charged particles coupled to the CS field and the occurrence of a transverse conductivity, which directly makes the theory useful for describing the Hall effect. There is a deep analogy between CS gauge theories and quantum mechanical Landau levels of charge particles (electrons) in a magnetic field which have led to the understanding of the fractional quantum Hall effect [2–4] and simple understanding of the origin of massive gauge excitations in CS theories. It is worth mentioning that CS theories have important applications in the quantum field theory; the CS gauge theory can arise as a string theory, CS gravity theory, etc. The statistical transmutation leads to the physics of "anyons" [4], which are particles with generalized statistics neither fermionic nor bosonic that occur as excitations upon the ground state wave function (Laughlin wave function) of a quantum Hall system.

The CS Lagrangian for the (2+1)–dimensional space–time is $L_{CS} = -1/2\,\kappa\varepsilon^{\mu\nu\rho}a_\mu\partial_\nu a_\rho$, where $\varepsilon^{\mu\nu\rho}$ is a U(1) gauge field and κ is a constant. The CS Lagrangian is invariant for the gauge transformation $a_\mu \to a_\rho + \partial_\mu\chi$, which is seen from $\varepsilon^{\mu\nu\rho}a_\mu\partial_\nu a_\rho \to \varepsilon^{\mu\nu\rho}a_\mu\partial_\nu a_\rho + \varepsilon^{\mu\nu\rho}\partial_\mu\chi\partial_\nu a_\rho$. The last term here can be written as total derivative $dS = \int d^3x\varepsilon^{\mu\nu\rho}\partial_\mu(\chi\partial_\nu a_\rho)$, which means that it vanishes if there is no boundary, or we can neglect the boundary effect. The equation of motion for the a_μ fields is $\kappa\varepsilon^{\mu\nu\rho}\partial_\nu a_\rho = 0$; for the field strength tensor $f_{\mu\nu} = \partial_\mu a_\nu - \partial_\nu a_\mu$, we have $f_{\mu\nu} = 0$. This is a trivial result, which is of no interest from the point of view of physics until the a_μ CS field is coupled to a J^μ source, which is the conserved current of another real physical field.

Using a simple example, we recall the gauge theory notation for a planar system of electrons. The usual Lagrangian of the Maxwell gauge theory is

$$L_M = -\frac{1}{4}F_{\mu\nu}F^{\mu\nu} - A_\mu J^\mu, \tag{1}$$

where $A_\mu = (A_0, \vec{A})$ is the gauge field, $F_{\mu\nu} = \partial_\mu A_\nu - \partial_\nu A_\mu$ is the field antisymmetric tensor, J^μ is the conserved current, $\partial_\mu J^\mu = 0$. Lagrangian (1) is invariant under the $A_\mu \to A_\mu + \partial_\mu\Lambda$ gauge transformation and, accordingly, the Euler–Lagrange equations of motion $\partial_\mu F^{\mu\nu} = J^\nu$ are gauge invariant. The new situation is for 2+1 dimensions. In this case, the CS theory is a

completely different type of gauge theory. It satisfies our usual criteria for a sensible gauge theory: it is Lorentz invariant, gauge invariant, and local. The CS Lagrangian is defined as follows:

$$L_{CS} = \frac{\kappa}{2}\varepsilon^{\mu\nu\rho}A_\mu\partial_\nu A_\rho - A_\mu J^\mu. \tag{2}$$

A gauge transformation changes the CS Lagrangian by a total space–time derivative:

$$\delta L_{CS} = \frac{\kappa}{2}\partial_\mu(\lambda\varepsilon^{\mu\nu\rho}\partial_\nu A_\rho). \tag{3}$$

Therefore, if we can neglect boundary terms, then the respective CS action $S_{CS} = \int d^3x L_{CS}$ is gauge invariant. Another important feature of CS Lagrangian (2) is that it is of the first order in space–time derivatives and, in 2+1 dimensions, the Lagrangian is quadratic in the gauge field. The Euler–Lagrange equations for CS Lagrangian are

$$\frac{\kappa}{2}\varepsilon^{\mu\nu\rho}F_{\nu\rho} = J^\mu, \text{ or } F_{\mu\nu} = \frac{1}{\kappa}\varepsilon_{\mu\nu\rho}J^\rho. \tag{4}$$

If we introduce a matter current $J^\mu = (\rho, \vec{J})$ and consider CS equations (4) coupled to matter fields, then the components of equation (4) are

$$\rho = \kappa B, \ J^i = \kappa\varepsilon^{ij}E_j. \tag{5}$$

The first equation (5) suggests that the charge density is locally proportional to the magnetic field, which means that the effect of a CS field is to relate magnetic flux to electric charge. Using the time derivative of the first equation in (5) $\dot{\rho} = \kappa\dot{B} = \kappa\varepsilon^{ij}\partial_i\dot{A}_j$ and the current conservation equation $\dot{\rho} + \partial_i J^i = 0$, we obtain

$$J^i = \kappa\varepsilon^{ij}\dot{A}_j + \varepsilon^{ij}\partial_j\chi, \tag{6}$$

which is the second equation in (5), transverse piece χ that can be identified with κA_0.

In this way, the effect of the CS coupling can be considered as a magnetic flux attached to the charge density in such a way that it everywhere follows the matter charge density. A feature of the CS theory is a magnetic flux attached to the charged particle fields together with the statistics transmutation. This feature is responsible for the appearance of CS fields in the composite boson or composite fermion models for the fractional quantum Hall effect, which involve quasiparticles that have magnetic fluxes attached to charged particles [5, 6].

Consider coupling of the Maxwell and CS Lagrangians, both of them producing gauge theories in 2+1 dimensions:

$$L_{MCS} = -\frac{1}{4e^2}F_{\mu\nu}F^{\mu\nu} + \frac{\kappa}{2}\varepsilon^{\mu\nu\rho}A_\mu\partial_\nu A_\rho. \tag{7}$$

The respective field equations

$$\partial_\mu F^{\mu\nu} + \frac{\kappa e^2}{2}\varepsilon^{\nu\alpha\beta}F_{\alpha\beta} = 0, \tag{8}$$

describe the propagation of a single degree of freedom with mass

$$m_{MCS} = \kappa e^2. \tag{9}$$

Here, κ is dimensionless and e^2 has mass dimension. If we write the equation of motion (8) in terms of the pseudovector "dual" field $\tilde{F}^\mu \equiv \varepsilon^{\mu\nu\rho}F_{\nu\rho}$, then we obtain

$$\left[\partial_\mu\partial^\mu + (\kappa e^2)^2\right]\tilde{F}^\nu = 0. \tag{10}$$

The origin of mass κe^2 is clearly seen from equation (10).

To better understand the importance of the CS theory, we consider the quantum mechanical analogy following [7]. In the gauge, $A_0 = 0$, the spatial components of gauge field $\vec{A}$ are conjugated to electric field $\vec{E}$, which satisfied equation $\nabla \cdot \vec{E} = \rho$, for which the "nondynamical" field A_0 is a Lagrange multiplier. We consider the structure of the Maxwell–CS theory Lagrangian:

$$\mathsf{L}_{MCS} = \frac{1}{2e^2}E_i^2 - \frac{1}{2e^2}B^2 + \frac{\kappa}{2}\varepsilon^{ij}A_iA_j + kA_0B. \tag{11}$$

The "nondynamical" field A_0 is a Lagrange multiplier that can be regarded as a Lagrange multiplier in the Gauss law constraint:

$$\partial_i F^{i0} + \kappa e^2\varepsilon^{ij}\partial_i A_j = 0. \tag{12}$$

This is the $\nu = 0$ component of the Euler–Lagrange equations (8). In the $A_0 = 0$ gauge, we identify A_i as "coordinate" fields with respective 'momentum' fields:

$$\Pi^i \equiv \frac{\partial\mathsf{L}}{\partial\dot{A}_i} = \frac{1}{e^2}\dot{A}_i + \frac{\kappa}{2}\varepsilon^{ij}A_j. \tag{13}$$

Using the Legendre transformation, we write down the Hamiltonian

$$\mathcal{H}_{MCS} = \Pi^i\dot{A}_i - \mathsf{L} =$$
$$\left(\frac{e^2}{2}\Pi^i - \frac{\kappa}{2}\varepsilon^{ij}A_j\right)^2 + \frac{1}{2e^2}B^2 + A_0(\partial_i\Pi^i + \kappa B). \tag{14}$$

If we consider the long wavelength limit of the Maxwell–CS Lagrangian, in which we can drop all spatial derivatives, then the resulting Lagrangian will be as follows:

$$L = \frac{1}{2e^2}\dot{A}_i^2 + \frac{\kappa}{2}\varepsilon^{ij}\dot{A}_iA_j. \tag{15}$$

This is exactly the Lagrangian for a nonrelativistic charged particle moving in the plane in the presence of a uniform external magnetic field B perpendicular to the plane:

$$L = \frac{1}{2}\dot{x}_i^2 + \frac{b}{2}\varepsilon^{ij}\dot{x}_ix_j. \tag{16}$$

For momentum, we have

$$p_i = \frac{\partial L}{\partial\dot{x}_i} = m\dot{x}_i + \frac{B}{2}\varepsilon^{ij}x_j, \tag{17}$$

and the Hamiltonian is

$$H = p_i \dot{x}_i - L = \frac{1}{2m}(p_i - \frac{b}{2}\varepsilon^{ij}x_j)^2 = \frac{m}{2}u_i^2. \tag{18}$$

The quantum commutation relations $[x_i, p_j] = i\delta_{ij}$ imply that the velocities do not commute, i.e. $[v_i, v_j] = -i\varepsilon_{ij}b/m^2$. This shows the quantum mechanical analogy to the classic Landau problem of electrons moving in the plane in the presence of an external uniform magnetic field perpendicular to the plane. In the latter case, fields $A_i(\bar{x}, t)$ and $\Pi^i(\bar{x}, t)$ in Hamiltonian (14) satisfy classical equal-time Poisson brackets: $\left[A_i(x), \Pi^j(y) \right] = i\delta_i^j\delta(\bar{x} - \bar{y})$ and $\left[E_i(x), E_j(y) \right] = i\kappa e^4\delta(\bar{x} - \bar{y})$.

There is a useful quantum mechanical analogy to the Landau problem of electrons moving in the plane with an external uniform magnetic field perpendicular to the plane; it is of special interest in quantum Hall systems.

It is now necessary to introduce density operators for the CS gauge field in a two-component electron–hole (e–h) system. We use the classical and quantum nonrelativistic CS theory for a two-dimensional N–body system of point particles, which was developed by Jackiw and Pi [8], to describe a 2D e–h system in a strong perpendicular magnetic field under the influence of quantum point vortices creating the CS gauge field. Phase operator $\hat{\omega}(\bar{r})$ of the CS field was introduced as a coherent summation of angles $\theta(\bar{r} - \bar{r}')$ formed with the in-plane *x*-axis by reference vectors $(\bar{r} - \bar{r}')$, which determine positions $\bar{r}'$ of the particles creating the gauge field at point $\bar{r}$. It was pointed in [8] that angles $\theta(\bar{r} - \bar{r}')$ are ill determined because arctangent is a multivalued function. However, this deficiency was compensated by the fact that the summation of the angles was weighted in [8] by density operators $\hat{\rho}(\bar{r}')$ of the charged particles as follows:

$$\hat{\omega}(\bar{r}) = -\frac{\phi e}{\alpha}\int d\bar{r}'\theta(\bar{r} - \bar{r}')\hat{\rho}(\bar{r}'); \quad \theta(\bar{r} - \bar{r}') = \arctan\left(\frac{y - y'}{x - x'}\right). \tag{19}$$

Here, ϕ is an integer, positive number and α is the fine structure constant $\alpha = e^2 / \hbar c = 1/137$. The integer value of ϕ is another factor, which makes the dressed field operators to be well defined. Since we are interested in the generalization of the CS theory from a one-component electron gas to a two–component e–h system, we repeat the main statements of the CS theory in a new version by introducing a supplementary label $i = e, h$ denoting electrons and holes from the very beginning. Partial field operators $\Psi_i(r)$ and $\Psi_i^+(r)$ lead to partial phase operators $\hat{\omega}_i(\bar{r})$ and to partial vector potential operators $\hat{\bar{a}}_i(\bar{r})$ taking into account the electrical charges of the electrons (-*e*) and the holes (+*e*).

The bare field operators will be denoted as $\hat{\Psi}_i^0(\bar{r})$ and $\Psi_i^{0+}(\bar{r})$ with supplementary label zero, whereas the dressed field operator $\hat{\Psi}_i(\bar{r})$ and $\Psi_i^+(\bar{r})$ will be written without it. Note that, while the bare and dressed field operators are different, their density operators $\hat{\rho}_i(\bar{r})$ and $\hat{\rho}_i^0(\bar{r})$

coincide:

$$\hat{\rho}_i(\vec{r}) = \hat{\Psi}_i^+(\vec{r})\hat{\Psi}_i(\vec{r}) = \hat{\Psi}_i^{+0}(\vec{r})\hat{\Psi}_i^0(\vec{r}) = \hat{\rho}_i^0(\vec{r}) \tag{20}$$

Below, we will show that this property is a consequence of the unitary transformation $\hat{u}^+(r)\hat{u}(r) = 1$ and it concerns any operators, which are analytical functions of the density operators as follows: $f(\hat{\rho}_i(\vec{r})) = f(\hat{\rho}_i^0(\vec{r}))$.

For example, partial phase operators $\hat{\omega}_i(\vec{r})$ and partial vector potential operators $\hat{\vec{a}}_i(\vec{r})$ show this property:

$$\hat{\omega}_i(\vec{r}) = -\frac{\phi e}{\alpha}\int d^2\vec{r}'\,\theta(\vec{r}-\vec{r}')\hat{\rho}_i(\vec{r}') = \hat{\omega}_i^0(\vec{r}),$$

$$\hat{\vec{a}}_i(\vec{r}) = \vec{\nabla}_{\vec{r}}\hat{\omega}_i(\vec{r}) = -\frac{\phi e}{\alpha}\int d^2\vec{r}'\,\vec{\nabla}_{\vec{r}}\theta(\vec{r}-\vec{r}')\hat{\rho}_i(\vec{r}') = \hat{\vec{a}}_i^0(\vec{r}), \tag{21}$$

$$\hat{\omega}(\vec{r}) = \hat{\omega}_e(\vec{r}) - \hat{\omega}_h(\vec{r}), \quad \hat{\vec{a}}(\vec{r}) = \hat{\vec{a}}_e(\vec{r}) - \hat{\vec{a}}_h(\vec{r}),$$

and, as was pointed in [8], the $\theta(\vec{r}-\vec{r}')$ function is ill determined. The differences added in (21) give rise to the resultant phase [9, 10] and vector potential operators [11] created by the integer e–h system [12].

Phase operators $\hat{\omega}_i(\vec{r})$ and $\hat{\omega}(\vec{r})$ are singular values because they are expressed in terms of a multivalued function, such as arctangent, and therefore as follows:

$$\vec{\nabla}_{\vec{r}}\theta(\vec{r}-\vec{r}') = -\vec{\nabla}_{\vec{r}}\times\ln|\vec{r}-\vec{r}'|; \quad \vec{\nabla}\times\theta(\vec{r}-\vec{r}') = \vec{\nabla}\ln(\vec{r}-\vec{r}'),$$

$$\Delta_{\vec{r}}\theta(\vec{r}-\vec{r}') = 0, \quad \Delta_{\vec{r}}\ln|\vec{r}-\vec{r}'| = 2\pi\delta^2(\vec{r}-\vec{r}');$$

where

$$\vec{\nabla}\times = \vec{e}_x\frac{\partial}{\partial y} - \vec{e}_y\frac{\partial}{\partial x}; \quad \vec{\nabla} = \vec{e}_x\frac{\partial}{\partial x} + \vec{e}_y\frac{\partial}{\partial y} = \frac{\vec{\in}_\theta}{r}\frac{\partial}{\partial\theta} + \vec{\in}_{\vec{r}}\frac{\partial}{\partial r}; \quad \vec{\in}_\theta = \frac{-\vec{e}_x y + \vec{e}_y x}{r}; \quad \vec{\in}_{\vec{r}} = \frac{\vec{r}}{r},$$

$$\vec{\nabla}\times\vec{V} = \in^{ij}\partial_i V_j = \frac{\partial}{\partial x}V_y - \frac{\partial}{\partial y}V_x = S,$$

$$(\vec{\nabla}\times S)^i = \in^{ij}\partial_j S; \quad \in^{12} = -\in^{21} = 1, \quad \in^{11} = \in^{22} = 0.$$

$$\vec{\nabla}\hat{\vec{a}}(\vec{r}) = 0,$$

$$\vec{\nabla}\times\hat{\vec{a}}(\vec{r}) = \hat{\vec{b}}(\vec{r}) = \vec{\nabla}_{\vec{r}}\times\frac{\phi e}{\alpha}\int d^2\vec{r}'\,\vec{\nabla}_{\vec{r}}\times\ln|\vec{r}-\vec{r}'|\hat{\rho}(\vec{r}') =$$

$$= \frac{\phi e}{\alpha}\int d^2\vec{r}'\,\Delta_{\vec{r}}\ln|\vec{r}-\vec{r}'|\hat{\rho}(\vec{r}') = 2\pi\frac{\phi e}{\alpha}\hat{\rho}(\vec{r}), \tag{22}$$

$$\hat{\vec{b}}(\vec{r}) = 2\pi\frac{\phi e}{\alpha}\hat{\rho}(\vec{r}) = 2\pi\frac{\phi e}{\alpha}(\hat{\rho}_e(\vec{r}) - \hat{\rho}_h(\vec{r})).$$

It was pointed out in [8] that, in the 2D space, the curl of the vector is a scalar, whereas the curl of the scalar is a vector. These properties are shows by formulas (22), in particular, the Green function of the Laplacian in the 2D space is $(\ln\vec{r})/2\pi$. Other important data provided by

formulas (22) is the effective magnetic field $\hat{\vec{b}}(\vec{r})$ expressed by $\vec{\nabla} \times \hat{\vec{a}}(\vec{r})$. It was shown in [8] that this magnetic field is created by quantum point vortices. In the case of a one-component electron gas, this supplementary magnetic field can compensate the external magnetic field. It will be shown below that, in the case of a two-component e–h system, this effective magnetic field has a special interesting property. It seems to vanish in the mean-field approximation when the average values of the density operators coincide $\langle \hat{\rho}_e(\vec{r}) \rangle = \langle \hat{\rho}_h(\vec{r}) \rangle$; however, its quantum fluctuations lead to unexpected physics of the 2D e–h system in a strong external magnetic field. Jackiw and Pi [8] gave a special attention to calculations involving the ill determined angle function $\theta(\vec{r} - \vec{r}')$. They emphasized that, in the nonrelativistic quantum mechanics, the particles are points and density operator $\hat{\rho}(\vec{r})$ is localized at these points being a superposition of the δ functions. This fact plays a critical role in calculations involving the CS gauge field. For example, it permits interchanging the integration and the differentiation in the definition of the CS vector potential $\hat{\vec{a}}(\vec{r})$. Otherwise, it would be impossible to move the gradient with respect to $\vec{r}$ out of the integral on variable $\vec{r}'$. In the general case, operators (21) are singular, because the $\theta(\vec{r} - \vec{r}')$ angle is a multivalued function and the integration over the 2D $\vec{r}'$ plane requires specifying the cut in $\vec{r}'$ beginning in $\vec{r}$. However, the presence of density operator $\hat{\rho}(\vec{r}')$ in the integral with δ-function eigenvalues leads to an exceptional situation, when $\vec{r}$ -gradient can be moved with impunity outside the integral. Since the derivative of the $\theta(\vec{r} - \vec{r}')$ function at point $\vec{r} = \vec{r}'$ is ill defined, the authors of [8] proposed its regularization: $\vec{\nabla}_{\vec{r}} = \theta(\vec{r} - \vec{r}')\big|_{\vec{r}=\vec{r}'} = 0$.

To confirm the affirmation concerning the eigenvalues of the density operators, it is necessary to use the commutation relations between the field operators and the density operator:

$$\left[\Psi_i(r), \hat{\rho}_i(\vec{r}') \right] = \delta^2(\vec{r} - \vec{r}') \hat{\Psi}_i(\vec{r}'); \quad \left[\Psi_i^+(r), \hat{\rho}_i(\vec{r}') \right] = -\delta^2(\vec{r} - \vec{r}') \hat{\Psi}_i^+(\vec{r}'),$$

$$\left[\hat{\rho}_i(\vec{r}), \hat{\rho}_j(\vec{r}') \right] = 0, \quad \left[\hat{\rho}_i(\vec{r}), \hat{\omega}(\vec{r}') \right] = 0, \quad \left[\hat{\omega}(\vec{r}'), \hat{\vec{a}}(\vec{r}) \right] = 0. \tag{23}$$

The proper functions of density operators $\hat{\rho}_i(\vec{r})$ can be introduced as follows:

$$\left| \hat{\Psi}_i(\vec{r}') \right\rangle = \hat{\Psi}_i^+(\vec{r}') |0\rangle, \quad \left\langle \hat{\Psi}_i(\vec{r}') \right| = \langle 0| \hat{\Psi}_i(\vec{r}'), \tag{24}$$

where $|0\rangle$ is the ground state of the system. The action of the density operator on the $\left| \hat{\Psi}_i(\vec{r}') \right\rangle$ function gives rise to the result

$$\hat{\rho}_i(\vec{r}) \left| \hat{\Psi}_i(\vec{r}') \right\rangle = \hat{\Psi}_i^+(\vec{r}) \hat{\Psi}_i(\vec{r}) \hat{\Psi}_i^+(\vec{r}') |0\rangle =$$

$$= \delta^2(\vec{r} - \vec{r}') \hat{\Psi}_i^+(\vec{r}) |0\rangle = \delta^2(\vec{r} - \vec{r}') \left| \hat{\Psi}_i(\vec{r}') \right\rangle. \tag{25}$$

It confirms that the eigenvalues of density operators $\hat{\rho}_i(\vec{r})$ have the form of δ-functions and that these operators play a decisive role in combating the deficiencies associated with the presence of the $\theta(\vec{r} - \vec{r}')$ angle function. The integer, positive values of numbers ϕ in the definitions of operators (21) contribute also to the removal of the incertitude associated with the

multivaluedness of the $\theta\left(\vec{r}-\vec{r}^{\,\prime}\right)$ angles.

The paper is organized as follows. Section 2 describes the unitary transformation operators that introduce the CS field into a two-component e–h system. In Section 3, we derive the Hamiltonian and the equations of motion for dressed field operators. The new properties of 2D magnetoexcitons under the influence of the CS gauge field are revealed in Section 4. Conclusions are given in Section 5.

2. Unitary Transformation Introducing the CS Gauge Field in a Two-Component Electron–Hole System

In a two-component e–h system, the electrons and the holes equally contribute to the creation of a unique and common CS gauge field, each of them acting with a proper electric charge. The resultant phase operator $\hat{\omega}(\vec{r})$ and its gradient are algebraic sums of the partial electron and hole contributions

$$\hat{\omega}(\vec{r}) = \hat{\omega}_e(\vec{r}) - \hat{\omega}_h(\vec{r}) = -\frac{\phi e}{\alpha}\int d^2\vec{r}^{\,\prime}\,\theta\left(\vec{r}-\vec{r}^{\,\prime}\right)\hat{\rho}\left(\vec{r}^{\,\prime}\right) = \hat{\omega}^+(\vec{r}),$$

$$\hat{\vec{a}}(\vec{r}) = \hat{\vec{a}}_e(\vec{r}) - \hat{\vec{a}}_h(\vec{r}) = -\frac{\phi e}{\alpha}\int d^2\vec{r}^{\,\prime}\,\vec{\nabla}_{\vec{r}}\,\theta\left(\vec{r}-\vec{r}^{\,\prime}\right)\hat{\rho}\left(\vec{r}^{\,\prime}\right) = \hat{\vec{a}}^+(\vec{r}),$$ (26)

$$\hat{\rho}(\vec{r}) = \hat{\rho}_e(\vec{r}) - \hat{\rho}_h(\vec{r}) = \hat{\rho}^+(\vec{r});$$

$$\hat{\rho}_i(\vec{r}) = \hat{\Psi}_i^+(\vec{r})\hat{\Psi}_i(\vec{r}) = \hat{\rho}_i^{\,+}(\vec{r}).$$

These expressions are true in the bare and dressed representations, no matter to which statistics—Fermi or Bose—obey the field operators. Unlike a one-component two-dimensional electron gas (2DEG), in this case, there are two subsystems with different electric charges. As a consequence, the resultant phase and vector potential operators compensate each other, so as to obtain a zero-gauge field in the mean-field approximation. It opens up the possibility of neglecting the effects arising due to the influence of the CS gauge field in the zero-order approximation and taking them into account in the next orders of the perturbation theory. In the case of a two-component e–h system, the unitary transformation introducing the CS gauge field looks as follows:

$$\hat{u}(r) = e^{\frac{ie}{\hbar c}\hat{\omega}(\vec{r})}; \quad \hat{u}^+(r) = e^{-\frac{ie}{\hbar c}\hat{\omega}(\vec{r})}; \quad \hat{u}^+(r)\hat{u}(r) = 1. \quad (27)$$

The bare electron and hole field operators will be denoted as $\hat{\Psi}_i^0(\vec{r})$ and $\hat{\Psi}_i^{0+}(\vec{r})$ with the supplementary zero label. They obey the Fermi statistics with the Fermi commutation relations

$$\hat{\Psi}_i^0(\vec{r})\hat{\Psi}_j^{0+}(\vec{r}) + \hat{\Psi}_j^{0+}(\vec{r})\hat{\Psi}_i^0(\vec{r}) = \delta_{ij}\delta^2\left(\vec{r}-\vec{r}^{\,\prime}\right),$$

$$\hat{\Psi}_i^0(\vec{r})\hat{\Psi}_j^0\left(\vec{r}^{\,\prime}\right) + \hat{\Psi}_j^0\left(\vec{r}^{\,\prime}\right)\hat{\Psi}_i^0(\vec{r}) = 0. \quad (28)$$

The dressed electron and hole field operators creating the CS gauge field are written without the zero label and they are introduced in the form

$$\hat{\Psi}_e(\vec{r}) = u^+(\vec{r})\hat{\Psi}_e^0(\vec{r}), \quad \hat{\Psi}_e^+(\vec{r}) = \hat{\Psi}_e^{0+}(\vec{r})u(\vec{r}),$$

$$\hat{\Psi}_h(\vec{r}) = \hat{u}(\vec{r})\hat{\Psi}_h^0(\vec{r}), \quad \hat{\Psi}_h^+(\vec{r}) = \hat{\Psi}_h^{0+}(\vec{r})u^+(\vec{r}),$$

$$\hat{\rho}_i(\vec{r}) = \hat{\Psi}_i^+(\vec{r})\hat{\Psi}_i(\vec{r}) = \hat{\rho}_i^0(\vec{r}) = \hat{\Psi}_i^{0+}(\vec{r})\hat{\Psi}_i^0(\vec{r}), i = e, h;$$

$$\hat{\rho}_i^+(\vec{r}) = \hat{\rho}_i(\vec{r}), \quad \hat{\rho}_i^{0+}(\vec{r}) = \hat{\rho}_i^0(\vec{r}), \quad \left[\hat{\rho}_i(\vec{r}), \hat{\rho}_j(\vec{r}')\right] = 0, \tag{29}$$

$$\hat{\rho}(\vec{r}) = \hat{\rho}_e(\vec{r}) - \hat{\rho}_h(\vec{r}) = \hat{\rho}^0(\vec{r}) = \hat{\rho}_e^0(\vec{r}) - \hat{\rho}_h^0(\vec{r}).$$

Due to the equality $\hat{\rho}(\vec{r}) = \hat{\rho}^0(\vec{r})$, the phase and vector potential operators determined by formulas (26) are the same in the bare and in the dressed representations:

$$\hat{\omega}(\vec{r}) = \hat{\omega}^0(\vec{r}), \quad \hat{\omega}_i(\vec{r}) = \hat{\omega}_i^0(\vec{r}),$$

$$\hat{\vec{a}}(\vec{r}) = \hat{\vec{a}}^0(\vec{r}), \quad \hat{\vec{a}}_i(\vec{r}) = \hat{\vec{a}}_i^0(\vec{r}), \quad \hat{\rho}(\vec{r}) = \hat{\rho}^0(\vec{r}). \tag{30}$$

This also concerns other operators expressed as analytic functions depending on density operator $\hat{\rho}(\vec{r})$. Despite the fact that bare electron and hole field operators $\hat{\Psi}_i^0(\vec{r})$ and $\hat{\Psi}_i^{0+}(\vec{r})$ obey Fermi commutation relations (28), dressed field operators $\hat{\Psi}_i(\vec{r})$ and $\hat{\Psi}_i^+(\vec{r})$ satisfy the Fermi or Bose statistics depending on the even or odd integer, positive numbers ϕ introduced into the definitions of operators (26). To prove this statement, it is necessary to derive first the commutation relations between field operators $\hat{\Psi}_i(\vec{r})$ and $\hat{\Psi}_i^+(\vec{r})$ with density operators $\hat{\rho}_i(\vec{r})$ and the commutation relations between the field operators and unitary transformations operators $u(\vec{r})$ and $u^+(\vec{r})$. The first of them are as follows:

$$\left[\hat{\Psi}_i(\vec{r}), \hat{\rho}_i(\vec{r}')\right] = \delta^2(\vec{r}-\vec{r}')\hat{\Psi}_i(\vec{r}'); \quad \left[\hat{\Psi}_i^+(\vec{r}'), \hat{\rho}_i(\vec{r}')\right] = -\delta^2(\vec{r}-\vec{r}')\hat{\Psi}_i^+(\vec{r}'). \tag{31}$$

They are the same as those in the case of the Fermi or Bose statistics. Thereupon, the following commutation relations can be obtained:

$$\hat{\Psi}_e(\vec{r})\hat{\omega}^n(\vec{r}') = \left[\hat{\omega}(\vec{r}') - \frac{\phi e}{\alpha}\theta(\vec{r}'-\vec{r})\right]^n \hat{\Psi}_e(\vec{r}),$$

$$\hat{\Psi}_h(\vec{r})\hat{\omega}^n(\vec{r}') = \left[\hat{\omega}(\vec{r}') + \frac{\phi e}{\alpha}\theta(\vec{r}'-\vec{r})\right]^n \hat{\Psi}_h(\vec{r}),$$

$$\hat{\Psi}_e^+(\vec{r})\hat{\omega}^n(\vec{r}') = \left[\hat{\omega}(\vec{r}') + \frac{\phi e}{\alpha}\theta(\vec{r}'-\vec{r})\right]^n \hat{\Psi}_e^+(\vec{r}), \tag{32}$$

$$\hat{\Psi}_h^+(\vec{r})\hat{\omega}^n(\vec{r}') = \left[\hat{\omega}(\vec{r}') - \frac{\phi e}{\alpha}\theta(\vec{r}'-\vec{r})\right]^n \hat{\Psi}_h^+(\vec{r}).$$

In this case, the commutation relations of field operators $\hat{\Psi}_i(\vec{r})$ with unitary transformation operators $\exp(\pm ie\hat{\omega}(\vec{r}')/(\hbar c))$ will be

$$\hat{\Psi}_e(\vec{r})e^{\pm\frac{ie}{\hbar c}\hat{\omega}(\vec{r}')} = \sum_{n=0}^{\infty}\left(\frac{\pm ie}{\hbar c}\right)^n \frac{1}{n!}\hat{\Psi}_e(\vec{r})\hat{\omega}^n(\vec{r}') =$$

$$= \sum_{n=0}^{\infty}\left(\frac{\pm ie}{\hbar c}\right)^n \frac{1}{n!}\left[\hat{\omega}(\vec{r}') - \frac{\phi e}{\alpha}\theta(\vec{r}'-\vec{r})\right]^n \hat{\Psi}_e(\vec{r}) =$$

$$= e^{\mp i\phi\theta(\vec{r}'-\vec{r})}e^{\frac{\pm ie}{\hbar c}\hat{\omega}(\vec{r}')}\hat{\Psi}_e(\vec{r}),$$

$$\hat{\Psi}_h(\vec{r})e^{\pm\frac{ie}{\hbar c}\hat{\omega}(\vec{r}')} = e^{\pm i\phi\theta(\vec{r}'-\vec{r})}e^{\frac{\pm ie}{\hbar c}\hat{\omega}(\vec{r}')}\hat{\Psi}_h(\vec{r}),$$

$$\hat{\Psi}_e^+(\vec{r})e^{\frac{\pm ie}{\hbar c}\hat{\omega}(\vec{r}')} = e^{\pm i\phi\theta(\vec{r}'-\vec{r})}e^{\frac{\pm ie}{\hbar c}\hat{\omega}(\vec{r}')}\hat{\Psi}_e^+(\vec{r}), \tag{33}$$

$$\hat{\Psi}_h^+(\vec{r})e^{\frac{\pm ie}{\hbar c}\hat{\omega}(\vec{r}')} = e^{\mp i\phi\theta(\vec{r}'-\vec{r})}e^{\frac{\pm ie}{\hbar c}\hat{\omega}(\vec{r}')}\hat{\Psi}_h^+(\vec{r}).$$

To prove the main statement concerning the statistics of the dressed field operators, we will start with the first equation (28) and transcribe it from the bare to dressed operators as follows:

$$\hat{\Psi}_e^0(\vec{r})\hat{\Psi}_e^{0+}(\vec{r}') + \hat{\Psi}_e^{0+}(\vec{r}')\hat{\Psi}_e^0(\vec{r}) = \delta^2(\vec{r}-\vec{r}') =$$

$$= u(\vec{r})\hat{\Psi}_e(\vec{r})\hat{\Psi}_e^+(\vec{r}')u^+(\vec{r}') + \hat{\Psi}_e^+(\vec{r}')u^+(\vec{r}')u(\vec{r})\hat{\Psi}_e(\vec{r}) =$$

$$= \hat{\Psi}_e(\vec{r})\hat{\Psi}_e^+(\vec{r}')u(\vec{r})u^+(\vec{r}')e^{i\phi\theta(0)}e^{-i\phi\theta(\vec{r}-\vec{r}')} +$$

$$+ \hat{\Psi}_e^+(\vec{r}')\hat{\Psi}_e(\vec{r})u^+(\vec{r}')u(\vec{r})e^{i\phi\theta(0)}e^{-i\phi\theta(\vec{r}'-\vec{r})}, \tag{34}$$

$$u(\vec{r})u^+(\vec{r}') = u^+(\vec{r}')u(\vec{r}),$$

$$\theta(\vec{r}'-\vec{r}) = \theta(\vec{r}-\vec{r}') + \pi.$$

With account of the last two relations, equation (34) can be transcribed in the form

$$e^{i\phi\theta(0)}e^{-i\phi\theta(\vec{r}-\vec{r}')}\left[\hat{\Psi}_e(\vec{r})\hat{\Psi}_e^+(\vec{r}') + e^{-i\phi\pi}\hat{\Psi}_e^+(\vec{r}')\hat{\Psi}_e(\vec{r})\right]\times$$

$$\times u(\vec{r})u^+(\vec{r}') = \delta^2(\vec{r}-\vec{r}'). \tag{35}$$

It is equivalent to the commutation relation

$$\hat{\Psi}_e(\vec{r})\hat{\Psi}_e^+(\vec{r}') + e^{-i\phi\pi}\hat{\Psi}_e^+(\vec{r}')\hat{\Psi}_e(\vec{r}) = \delta^2(\vec{r}-\vec{r}'),$$

$$e^{-i\phi\pi} = \cos\phi\pi - i\sin(\phi\pi) = \begin{cases} 1, \phi = 0,2,4...,F \\ -1, \phi = 1,3,5..,B \end{cases}. \tag{36}$$

The most important result of these calculation is the affirmation that CS gauge field operators $\hat{\Psi}_i^+(\vec{r})$ and $\hat{\Psi}_i(\vec{r})$ with $i = e,h$ obey the Fermi statistics in the case of the even integer, positive pair numbers ϕ and the Bose statistics in the case of odd integer positive numbers ϕ. It is an important result of the CS gauge field theory developed by Jackiw and Pi in [8].

3. Hamiltonian and Equations of Motion Describing the Dressed Operators of the CS Gauge Field

To obtain a Hamiltonian describing the interaction of the composite particles expressed in terms of dressed field operators $\hat{\Psi}_i^+(\vec{r})$ and $\hat{\Psi}_i(\vec{r})$ and deduce their equations of motion, we will start with the respective expressions for bare field operators $\hat{\Psi}_i^{0+}(\vec{r})$ and $\hat{\Psi}_i^0(\vec{r})$. The Hamiltonian describing bare 2D electrons and holes in an external perpendicular magnetic field and interacting by the Coulomb forces obtained in [13] looks as follows:

$$\hat{H}^0 = \hat{K}^0 + \hat{H}_{Coul}^0,$$

$$\hat{K}^0 = \frac{\hbar^2}{2m_e} \int d^2\vec{r}' \hat{\Psi}_e^{0+}(\vec{r}') \left(-i\vec{\nabla}' + \frac{e}{\hbar c}\vec{A}(\vec{r}')\right)^2 \hat{\Psi}_e^{0+}(\vec{r}') +$$

$$+ \frac{\hbar^2}{2m_h} \int d^2\vec{r}' \hat{\Psi}_h^{0+}(\vec{r}') \left(-i\vec{\nabla}' - \frac{e}{\hbar c}\vec{A}(\vec{r}')\right)^2 \hat{\Psi}_h^{0+}(\vec{r}'),$$

$$\hat{H}_{Coul}^0 = \frac{1}{2} \int d^2\vec{r}' \int d^2\vec{r}'' V_{Coul}(\vec{r}' - \vec{r}'') \hat{\Psi}_e^{0+}(\vec{r}') \hat{\rho}_e^0(\vec{r}'') \hat{\Psi}_e^0(\vec{r}') +$$

$$+ \frac{1}{2} \int d^2\vec{r}' \int d^2\vec{r}'' V_{Coul}(\vec{r}' - \vec{r}'') \hat{\Psi}_h^{0+}(\vec{r}') \hat{\rho}_h^0(\vec{r}'') \hat{\Psi}_h^0(\vec{r}') -$$

$$- \int d^2\vec{r}' \int d^2\vec{r}'' V_{Coul}(\vec{r}' - \vec{r}'') \hat{\Psi}_e^{0+}(\vec{r}') \hat{\rho}_h^0(\vec{r}'') \hat{\Psi}_e^0(\vec{r}'). \tag{37}$$

Here, $\vec{A}(\vec{r}')$ is the vector potential created by an external magnetic field perpendicular to the layer. In the Landau gauge description, it has the form of $\vec{A}(\vec{r}) = (-B \cdot y, 0, 0)$, where B is the magnetic field strength. The vector potential obeys the following condition: $\vec{\nabla}\vec{A}(\vec{r}) = 0$. The Coulomb interaction potential in a 2D system can be represented as

$$V_{Coul}(\vec{r}) = \sum_{\vec{Q}} V_{\vec{Q}} e^{i\vec{Q}\vec{r}}, \ V(\vec{Q}) = \frac{2\pi e^2}{\varepsilon_0 S|\vec{Q}|}, \ W(\vec{Q}) = V(\vec{Q}) e^{-\frac{Q^2 l_0^2}{2}}; \ l_0^2 = \frac{\hbar c}{eB}. \tag{38}$$

Here, S is the layer surface area, ε_0 is the effective dielectric constant, and l_0 is the magnetic length. Coefficient $W(\vec{Q})$, along with coefficient $V(\vec{Q})$, was introduced into (38); it will be used below.

Bare density operators $\hat{\rho}_i^0(\vec{r})$ were introduced by formula (20). Schrodinger equations for bare operators $\hat{\Psi}_e^0(\vec{r})$ and $\hat{\Psi}_h^0(\vec{r})$ were derived in [13], and we just recall them:

$$i\hbar \frac{d\hat{\Psi}_e^0(\vec{r})}{dt} = \left[\hat{\Psi}_e^0(\vec{r}), \hat{H}^0\right] = \frac{\hbar^2}{2m_e}\left(-i\vec{\nabla} + \frac{e}{\hbar c}\vec{A}(\vec{r})\right)^2 \hat{\Psi}_e^0(\vec{r}) +$$

$$+ \int d^2\vec{r}' V_{Coul.}(\vec{r} - \vec{r}')\hat{\rho}^0(\vec{r}')\hat{\Psi}_e^0(\vec{r}),$$

$$i\hbar \frac{d\hat{\Psi}_h^0(\vec{r})}{dt} = \left[\hat{\Psi}_h^0(\vec{r}), \hat{H}^0\right] = \frac{\hbar^2}{2m_h}\left(-i\vec{\nabla} - \frac{e}{\hbar c}\vec{A}(\vec{r})\right)^2 \hat{\Psi}_h^0(\vec{r}) -$$

$$- \int d^2\vec{r}' V_{Coul.}(\vec{r} - \vec{r}')\hat{\rho}^0(\vec{r}')\hat{\Psi}_h^0(\vec{r}),$$

$$i\hbar \frac{d\hat{\Psi}_e^{0+}(\vec{r})}{dt} = \left[\hat{\Psi}_e^{0+}(\vec{r}), \hat{H}^0\right] = -\frac{\hbar^2}{2m_e}\left(i\vec{\nabla} + \frac{e}{\hbar c}\vec{A}(\vec{r})\right)^2 \hat{\Psi}_e^{0+}(\vec{r}) - \qquad (39)$$

$$- \int d^2\vec{r}' V_{Coul.}(\vec{r} - \vec{r}')\hat{\Psi}_e^{0+}(\vec{r})\hat{\rho}^0(\vec{r}'),$$

$$i\hbar \frac{d\hat{\Psi}_h^{0+}(\vec{r})}{dt} = -\frac{\hbar^2}{2m_h}\left(i\vec{\nabla} - \frac{e}{\hbar c}\vec{A}(\vec{r})\right)^2 \hat{\Psi}_h^{0+}(\vec{r}) + \int d^2\vec{r}' V_{Coul.}(\vec{r} - \vec{r}')\hat{\Psi}_h^{0+}(\vec{r})\hat{\rho}^0(\vec{r}');$$

$$\hat{\rho}^{0+}(\vec{r}') = \hat{\rho}^0(\vec{r}').$$

Time derivatives $d(\hat{\rho}_i^0(\vec{r}))/dt$ and the continuity equations were derived using equations of motion

$$\frac{d}{dt}\hat{\rho}_i^0(\vec{r}) = \frac{d}{dt}\left(\hat{\Psi}_i^{0+}(\vec{r})\hat{\Psi}_i^0(\vec{r})\right) = -\vec{\nabla}\hat{\vec{J}}_i^0(\vec{r}); \quad i = e, h.$$

$$\hat{\vec{J}}_e^0(\vec{r}) = \frac{\hbar}{2m_e i}\left(\hat{\Psi}_e^{0+}(\vec{r})\vec{\nabla}\hat{\Psi}_e^0(\vec{r}) - \vec{\nabla}\hat{\Psi}_e^{0+}(\vec{r})\hat{\Psi}_e^0(\vec{r})\right) + \frac{e}{m_e c}\vec{A}(\vec{r})\hat{\rho}_e^0(\vec{r}),$$

$$\hat{\vec{J}}_h^0(\vec{r}) = \frac{\hbar}{2m_h i}\left(\hat{\Psi}_h^{0+}(\vec{r})\vec{\nabla}\hat{\Psi}_h^0(\vec{r}) - \vec{\nabla}\hat{\Psi}_h^{0+}(\vec{r})\hat{\Psi}_h^0(\vec{r})\right) - \frac{e}{m_h c}\vec{A}(\vec{r})\hat{\rho}_h^0(\vec{r}). \qquad (40)$$

The equations of motion for dressed field operators $\hat{\Psi}_i^+(\vec{r})$ and $\hat{\Psi}_i(\vec{r})$ can be obtained taking into account equation (39) and time derivatives of unitary transformation operators $\hat{u}(\vec{r}) = \hat{u}^0(\vec{r})$ and $\hat{u}^+(\vec{r}) = \hat{u}^{0+}(\vec{r})$, which coincide in the bare and dressed representations as well as operators $\hat{\rho}_i(\vec{r}) = \hat{\rho}_i^0(\vec{r})$, $\hat{\omega}_i(\vec{r}) = \hat{\omega}_i^0(\vec{r})$. Therefore, one of them can be used in calculations without supplementary specifications.

Following the procedure used in [13], we obtain two equations:

$$\frac{i\hbar d\hat{\Psi}_e(\vec{r})}{dt} = i\hbar \frac{d}{dt}\left(\hat{u}^+(\vec{r})\hat{\Psi}_e^0(\vec{r})\right) = i\hbar \frac{d}{dt}\hat{u}^+(\vec{r}) \cdot \hat{\Psi}_e^0(\vec{r}) + \hat{u}^+(\vec{r})\frac{i\hbar d}{dt}\hat{\Psi}_e^0(\vec{r}),$$

$$\frac{i\hbar d\hat{\Psi}_h(\vec{r})}{dt} = i\hbar \frac{d}{dt}\left(\hat{u}(\vec{r})\hat{\Psi}_h^0(\vec{r})\right) = i\hbar \frac{d}{dt}\hat{u}(\vec{r}) \cdot \hat{\Psi}_h^0(\vec{r}) + \hat{u}(\vec{r})\frac{i\hbar d}{dt}\hat{\Psi}_h^0(\vec{r}). \qquad (41)$$

To obtain time derivatives of unitary transformation operators $\exp(\pm ie\hat{\omega}(\vec{r})/(\hbar c))$, we take into account that operators $d\hat{\omega}(\vec{r})/dt$ and $\hat{\omega}(\vec{r})$ do not commute. This was pointed out by Jackiw

and Pi in [8] and demonstrated in [13] as follows:

$$\left[\frac{d\hat{\omega}(\vec{r})}{dt},\hat{\omega}(\vec{r})\right]=-i\hat{L}(\vec{r})=\left(\frac{\phi e}{\alpha}\right)^2\int d^2\vec{r}'\int d^2\vec{r}''\theta(\vec{r}-\vec{r}')\times$$

$$\times\theta(\vec{r}-\vec{r}'')\left[\frac{d\hat{\rho}(\vec{r}')}{dt},\hat{\rho}(\vec{r}'')\right]=\left(\frac{\phi e}{\alpha}\right)^2\int d^2\vec{r}'\int d^2\vec{r}''\theta(\vec{r}-\vec{r}')\theta(\vec{r}-\vec{r}'')\times$$

$$\times\left\{\left[\frac{d\hat{\rho}_e(\vec{r}')}{dt},\hat{\rho}_e(\vec{r}'')\right]+\left[\frac{d\hat{\rho}_h(\vec{r}')}{dt},\hat{\rho}_h(\vec{r}'')\right]\right\}=\left(\frac{\phi e}{\alpha}\right)^2\int d^2\vec{r}'\int d^2\vec{r}''\times$$

$$\times\vec{\nabla}'\theta(\vec{r}-\vec{r}')\theta(\vec{r}-\vec{r}'')\left\{\left[\hat{\vec{J}}_e(\vec{r}'),\hat{\rho}_e(\vec{r}'')\right]+\left[\hat{\vec{J}}_h(\vec{r}')\hat{\rho}_h(\vec{r}'')\right]\right\},\tag{42}$$

where we used expressions (40), which lead to the form

$$\hat{L}(\vec{r})=\frac{\hbar}{2m_e}\hat{M}_e(\vec{r})+\frac{\hbar}{2m_h}\hat{M}_h(\vec{r}),$$

$$\hat{M}_i(\vec{r})=\left(\frac{\phi e}{\alpha}\right)^2\int d^2\vec{r}'\int d^2\vec{r}''\vec{\nabla}'\theta(\vec{r}-\vec{r}')\theta(\vec{r}-\vec{r}'')\times$$

$$\times\left\{\left[\hat{\Psi}_i^{0+}(\vec{r}')\vec{\nabla}'\hat{\Psi}_i^0(\vec{r}'),\hat{\rho}_i^0(\vec{r}'')\right]-\left[\vec{\nabla}'\hat{\Psi}_i^{0+}(\vec{r}')\hat{\Psi}_i^0(\vec{r}'),\hat{\rho}_i^0(\vec{r}'')\right]\right\};\ i=e,h.\tag{43}$$

The commutation relations that were substituted into formulas (43) were calculated in [13] and look as follows:

$$\left[\hat{\Psi}_i^{0+}(\vec{r}')\vec{\nabla}'\hat{\Psi}_i^0(\vec{r}'),\hat{\rho}_i^0(\vec{r}'')\right]=\hat{\Psi}_i^{0+}(\vec{r}')\vec{\nabla}'\left(\delta^2(\vec{r}'-\vec{r}'')\hat{\Psi}_i^0(\vec{r}'')\right)-$$

$$-\delta^2(\vec{r}'-\vec{r}'')\hat{\Psi}_i^{0+}(\vec{r}'')\vec{\nabla}'\hat{\Psi}_i^0(\vec{r}'),$$

$$\left[\vec{\nabla}'\hat{\Psi}_i^{0+}(\vec{r}')\hat{\Psi}_i^0(\vec{r}'),\hat{\rho}_i^0(\vec{r}'')\right]=-\vec{\nabla}'\left(\delta^2(\vec{r}'-\vec{r}'')\hat{\Psi}_i^{0+}(\vec{r}'')\right)\hat{\Psi}_i^0(\vec{r}')+$$

$$+\vec{\nabla}'\hat{\Psi}_i^{0+}(\vec{r}')\delta^2(\vec{r}'-\vec{r}'')\hat{\Psi}_i^0(\vec{r}''),\ i=e,h.\tag{44}$$

The $\Delta'\theta(\vec{r}-\vec{r}')=0$ and $\left(\vec{\nabla}'\theta(\vec{r}-\vec{r}')\right)^2=\left|\vec{r}-\vec{r}'\right|^{-2}$ properties help to effectuate the next calculations, which lead to the expressions

$$\hat{M}_i(\vec{r})=2\left(\frac{\phi e}{\alpha}\right)^2\int d^2\vec{r}'\frac{\hat{\rho}_i^0(\vec{r}')}{\left|\vec{r}-\vec{r}'\right|^2},\ i=e,h;$$

$$\hat{L}(\vec{r})=\left(\frac{\phi e}{\alpha}\right)\hbar\left[\frac{1}{m_e}\int d^2\vec{r}'\frac{\hat{\rho}_e^0(\vec{r}')}{\left|\vec{r}-\vec{r}'\right|^2}+\frac{1}{m_h}\int d^2\vec{r}'\frac{\hat{\rho}_h^0(\vec{r}')}{\left|\vec{r}-\vec{r}'\right|^2}\right],$$

$$\left[\hat{L}(\vec{r}),\hat{\omega}(\vec{r})\right]=\left[\hat{L}(\vec{r}),\hat{\rho}_i(\vec{r})\right]=0.\tag{45}$$

To derive time derivatives of the unitary transformation operators, we will use the following formula:

$$\frac{d}{dt}e^{\pm\frac{ie}{\hbar c}}\hat{\omega}(\vec{r}) = \sum_{n=0}^{\infty}\left(\pm\frac{ie}{\hbar c}\right)^{n}\frac{1}{n!}\frac{d}{dt}\hat{\omega}^{n}(\vec{r}). \tag{46}$$

The first steps are the following results:

$$\frac{d}{dt}\hat{\omega}^{2}(\vec{r}) = 2\hat{\omega}(\vec{r})\frac{d\hat{\omega}(\vec{r})}{dt} - i\hat{L}(\vec{r}) = 2\frac{d\hat{\omega}(\vec{r})}{dt}\hat{\omega}(\vec{r}) + i\hat{L}(\vec{r}),$$

$$\frac{d}{dt}\hat{\omega}^{3}(\vec{r}) = 3\omega^{2}(\vec{r})\frac{d\omega(\vec{r})}{dt} - 3i\hat{L}(\vec{r})\hat{\omega}(\vec{r}) = 3\frac{d\omega(\vec{r})}{dt}\hat{\omega}^{2}(\vec{r}) + 3i\hat{L}(\vec{r})\hat{\omega}(\vec{r}),$$

$$\frac{d}{dt}\hat{\omega}^{n}(\vec{r}) = n\omega^{(n-1)}(\vec{r})\frac{d\omega(\vec{r})}{dt} - iX_{n}\hat{L}(\vec{r})\hat{\omega}^{(n-2)}(\vec{r}) =$$

$$= n\frac{d\omega(\vec{r})}{dt}\hat{\omega}^{(n-1)}(\vec{r}) + iX_{n}\hat{L}(\vec{r})\hat{\omega}^{(n-2)}(\vec{r}),$$

$$X_{n} = (n-1) + X_{n-1} + \frac{n(n-1)}{2}, \quad n \geq 2. \tag{47}$$

The last equation was used as follows:

$$\frac{d}{dt}e^{\pm\frac{ie}{\hbar c}\hat{\omega}(\vec{r})} = \left(\pm\frac{ie}{\hbar c}\right)\frac{d\hat{\omega}(\vec{r})}{dt} + \sum_{n=2}^{\infty}\left(\pm\frac{ie}{\hbar c}\right)^{n}\frac{1}{n!}\frac{d}{dt}\hat{\omega}(\vec{r})^{n} =$$

$$= \left(\pm\frac{ie}{\hbar c}\right)\frac{d\hat{\omega}(\vec{r})}{dt} + \sum_{k=1}^{\infty}\left(\pm\frac{ie}{\hbar c}\right)^{(k+1)}\frac{1}{k!}\hat{\omega}^{k}(\vec{r})\frac{d\hat{\omega}(\vec{r})}{dt} -$$

$$- i\hat{L}(\vec{r})\sum_{m=0}^{\infty}\left(\pm\frac{ie}{\hbar c}\right)^{(m+2)}\frac{X_{(m+2)}}{(m+2)!}\hat{\omega}^{m}(\vec{r}) =$$

$$= \left(\pm\frac{ie}{\hbar c}\right)\frac{d\hat{\omega}(\vec{r})}{dt} + \frac{d\hat{\omega}(\vec{r})}{dt}\sum_{k=1}^{\infty}\left(\pm\frac{ie}{\hbar c}\right)^{(k+1)}\frac{1}{k!}\hat{\omega}^{k}(\vec{r}) +$$

$$+ i\hat{L}(\vec{r})\sum_{m=0}^{\infty}\left(\pm\frac{ie}{\hbar c}\right)^{(m+2)}\frac{X_{(m+2)}}{(m+2)!}\hat{\omega}^{m}(\vec{r}) =$$

$$= e^{\pm\frac{ie}{\hbar c}\hat{\omega}(\vec{r})}\left[\left(\pm\frac{ie}{\hbar c}\right)\frac{d\hat{\omega}(\vec{r})}{dt} + \frac{i}{2}\left(\frac{e}{\hbar c}\right)^{2}\hat{L}(\vec{r})\right] =$$

$$= \left[\left(\pm\frac{ie}{\hbar c}\right)\frac{d\hat{\omega}(\vec{r})}{dt} - \frac{i}{2}\left(\frac{e}{\hbar c}\right)^{2}\hat{L}(\vec{r})\right]e^{\pm\frac{ie}{\hbar c}\hat{\omega}(\vec{r})} \times$$

$$\times\frac{X_{(m+2)}}{(m+2)!} = \frac{1}{2}\cdot\frac{1}{m!}, \quad m \geq 0. \tag{48}$$

We can now calculate the commutation relation between time derivative $d\hat{\omega}(\vec{r})/dt$ and unitary transformation operators $\exp(\pm ie\hat{\omega}(\vec{r})/(\hbar c))$:

$$\left[\frac{d\hat{\omega}(\vec{r})}{dt}, e^{\pm\frac{ie}{\hbar c}\hat{\omega}(\vec{r})}\right] = \sum_{n=0}^{\infty}\left(\pm\frac{ie}{\hbar c}\right)^n \cdot \frac{1}{n!}\left[\frac{d\hat{\omega}(\vec{r})}{dt}, \hat{\omega}^n(\vec{r})\right]. \tag{49}$$

To clarify this issue, we recall the basic equalities

$$\left[\frac{d\hat{\omega}(\vec{r})}{dt}, \hat{\omega}(\vec{r})\right] = -i\hat{L}(\vec{r}), \quad \left[\frac{d\hat{\omega}^2(\vec{r})}{dt}, \hat{\omega}(\vec{r})\right] = -2i\hat{L}(\vec{r})\hat{\omega}(\vec{r}).$$

They lead to the recurrent formula

$$\left[\frac{d\hat{\omega}(\vec{r})}{dt}, \hat{\omega}^n(\vec{r})\right] = -in\hat{L}(\vec{r})\hat{\omega}^{n-1}(\vec{r}), \tag{50}$$

which solves the problem:

$$\left[\frac{d\hat{\omega}(\vec{r})}{dt}, e^{\pm\frac{ie}{\hbar c}\hat{\omega}(\vec{r})}\right] = \left(\pm\frac{ie}{\hbar c}\right)\hat{L}(\vec{r})e^{\pm\frac{ie}{\hbar c}\hat{\omega}(\vec{r})}. \tag{51}$$

Next, to derive the equations of motion for dressed field operators $\hat{\Psi}_i(\vec{r})$ and $\hat{\Psi}_i^+(\vec{r})$, we consider equations

$$i\hbar\frac{d}{dt}\hat{\Psi}_e(\vec{r}) = i\hbar\frac{d}{dt}\left(\hat{u}^+(\vec{r})\hat{\Psi}_e^0(\vec{r})\right) = i\hbar\frac{d\hat{u}^+(\vec{r})}{dt}\hat{\Psi}_e^0(\vec{r}) + \hat{u}^+(\vec{r})i\hbar\frac{d\hat{\Psi}_e^0(\vec{r})}{dt},$$

$$i\hbar\frac{d}{dt}\hat{\Psi}_h(\vec{r}) = i\hbar\frac{d}{dt}\left(\hat{u}(\vec{r})\hat{\Psi}_h^0(\vec{r})\right) = i\hbar\frac{d\hat{u}(\vec{r})}{dt}\hat{\Psi}_h^0(\vec{r}) + \hat{u}(\vec{r})i\hbar\frac{d\hat{\Psi}_h^0(\vec{r})}{dt}. \tag{52}$$

We recall that operators $\hat{\omega}(\vec{r})$ and $d\hat{\omega}(\vec{r})/dt$ do not commute and their commutation equals to

$$\left[\frac{d\hat{\omega}(\vec{r})}{dt}, \hat{\omega}(\vec{r})\right] = -i\hat{L}(\vec{r}), \tag{53}$$

$$\hat{L}^+(\vec{r}) = \hat{L}(\vec{r}), \quad \left[\hat{L}(\vec{r}), \hat{\rho}_i(\vec{r})\right] = 0, \quad \left[\hat{L}(\vec{r}), \hat{\omega}(\vec{r}')\right] = 0.$$

Similar to as it was done in the derivation of equation (48), we can write

$$i\hbar\frac{d\hat{u}(\vec{r})}{dt} = \hat{u}(\vec{r})\left[-\frac{e}{c}\frac{d\hat{\omega}(\vec{r})}{dt} - \frac{e^2}{2\hbar c^2}\hat{L}(\vec{r})\right] =$$

$$= \left[-\frac{e}{c}\frac{d\hat{\omega}(\vec{r})}{dt} + \frac{e^2}{2\hbar c^2}\hat{L}(\vec{r})\right]\hat{u}(\vec{r}),$$

$$\hat{u}(\vec{r}) = e^{\frac{ie}{\hbar c}\hat{\omega}(\vec{r})},$$

$$i\hbar\frac{d\hat{u}^{+}\left(\vec{r}\right)}{dt}=\hat{u}^{+}\left(\vec{r}\right)\left[\frac{e}{c}\frac{d\hat{\omega}\left(\vec{r}\right)}{dt}-\frac{e^{2}}{2\hbar c^{2}}\hat{L}\left(\vec{r}\right)\right]=$$

$$=\left[\frac{e}{c}\frac{d\hat{\omega}\left(\vec{r}\right)}{dt}+\frac{e^{2}}{2\hbar c^{2}}\hat{L}\left(\vec{r}\right)\right]\hat{u}^{+}\left(\vec{r}\right), \tag{54}$$

$$\hat{u}^{+}\left(\vec{r}\right)=e^{-\frac{ie}{\hbar c}\hat{\omega}\left(\vec{r}\right)}.$$

Below, we will use formulas describing the action of operator $\left(-i\vec{\nabla}\right)$ on unitary transformation operators $\exp(\pm ie\hat{\omega}(\vec{r})/(\hbar c))$:

$$\left(-i\vec{\nabla}\right)e^{\pm\frac{ie}{\hbar c}\hat{\omega}\left(\vec{r}\right)}=\pm\frac{e}{\hbar c}\hat{\vec{a}}\left(\vec{r}\right)e^{\pm\frac{ie}{\hbar c}\hat{\omega}\left(\vec{r}\right)};\;\;\hat{\vec{a}}\left(\vec{r}\right)=\vec{\nabla}\hat{\omega}\left(\vec{r}\right),$$

$$e^{-\frac{ie}{\hbar c}\hat{\omega}\left(\vec{r}\right)}\left(-i\vec{\nabla}+\frac{e}{\hbar c}\vec{A}\left(\vec{r}\right)\right)^{2}\hat{\Psi}_{e}^{0}\left(\vec{r}\right)=\left(-i\vec{\nabla}+\frac{e}{\hbar c}\vec{A}\left(\vec{r}\right)+\frac{e}{\hbar c}\hat{\vec{a}}\left(\vec{r}\right)\right)^{2}\hat{\Psi}_{e}\left(\vec{r}\right),$$

$$e^{\frac{ie}{\hbar c}\hat{\omega}\left(\vec{r}\right)}\left(-i\vec{\nabla}-\frac{e}{\hbar c}\vec{A}\left(\vec{r}\right)\right)^{2}\hat{\Psi}_{h}^{0}\left(\vec{r}\right)=\left(-i\vec{\nabla}-\frac{e}{\hbar c}\vec{A}\left(\vec{r}\right)-\frac{e}{\hbar c}\hat{\vec{a}}\left(\vec{r}\right)\right)^{2}\hat{\Psi}_{h}\left(\vec{r}\right). \tag{55}$$

$$\hat{\Psi}_{e}\left(\vec{r}\right)=u^{+}\left(\vec{r}\right)\hat{\Psi}_{e}^{0}\left(\vec{r}\right),\hat{\Psi}_{h}\left(\vec{r}\right)=\hat{u}\left(\vec{r}\right)\hat{\Psi}_{e}^{0}\left(\vec{r}\right),\left[\vec{a}\left(\vec{r}\right),\hat{\omega}\left(\vec{r}'\right)\right]=0.$$

The time derivatives of the dressed field operators can be expressed in terms of derivatives of their components:

$$i\hbar\frac{d}{dt}\hat{\Psi}_{e}\left(\vec{r}\right)=i\hbar\frac{d\hat{u}^{+}\left(\vec{r}\right)}{dt}\hat{\Psi}_{e}^{0}\left(\vec{r}\right)+\hat{u}^{+}\left(\vec{r}\right)i\hbar\frac{d\hat{\Psi}_{e}^{0}\left(\vec{r}\right)}{dt},$$

$$i\hbar\frac{d}{dt}\hat{\Psi}^{h}\left(\vec{r}\right)=i\hbar\frac{d\hat{u}\left(\vec{r}\right)}{dt}\hat{\Psi}_{h}^{0}\left(\vec{r}\right)+\hat{u}\left(\vec{r}\right)i\hbar\frac{d\hat{\Psi}_{h}^{0}\left(\vec{r}\right)}{dt}. \tag{56}$$

Using formulas (39), (54), and (55), we obtain

$$i\hbar\frac{d\hat{\Psi}_{e}\left(\vec{r}\right)}{dt}=\frac{\hbar^{2}}{2m_{e}}\left(-i\vec{\nabla}-\frac{e}{\hbar c}\vec{A}\left(\vec{r}\right)+\frac{e}{\hbar c}\hat{\vec{a}}\left(\vec{r}\right)\right)^{2}\hat{\Psi}_{e}\left(\vec{r}\right)+$$

$$+\frac{e}{c}\frac{d\hat{\omega}\left(\vec{r}\right)}{dt}\hat{\Psi}_{e}\left(\vec{r}\right)+\frac{e^{2}}{2\hbar c^{2}}\hat{L}\left(\vec{r}\right)\hat{\Psi}_{e}\left(\vec{r}\right)+\int d^{2}\vec{r}'V_{Coul.}\left(\vec{r}-\vec{r}'\right)\hat{\rho}\left(\vec{r}'\right)\hat{\Psi}_{e}\left(\vec{r}\right),$$

$$i\hbar\frac{d\hat{\Psi}_{h}\left(\vec{r}\right)}{dt}=\frac{\hbar^{2}}{2m_{h}}\left(-i\vec{\nabla}-\frac{e}{\hbar c}\vec{A}\left(\vec{r}\right)-\frac{e}{\hbar c}\hat{\vec{a}}\left(\vec{r}\right)\right)^{2}\hat{\Psi}_{h}\left(\vec{r}\right)-$$

$$-\frac{e}{c}\frac{d\hat{\omega}\left(\vec{r}\right)}{dt}\hat{\Psi}_{h}\left(\vec{r}\right)+\frac{e^{2}}{2\hbar c^{2}}\hat{L}\left(\vec{r}\right)\hat{\Psi}_{h}\left(\vec{r}\right)-\int d^{2}\vec{r}'V_{Coul.}\left(\vec{r}-\vec{r}'\right)\hat{\rho}\left(\vec{r}'\right)\hat{\Psi}_{h}\left(\vec{r}\right), \tag{57}$$

$$\hat{\rho}\left(\vec{r}'\right)=\hat{\rho}_{e}\left(\vec{r}'\right)-\hat{\rho}_{h}\left(\vec{r}'\right);\hat{\rho}_{i}\left(\vec{r}'\right)=\hat{\Psi}_{i}^{+}\left(\vec{r}'\right)\hat{\Psi}_{i}\left(\vec{r}'\right),\;i=e,h.$$

Unlike equations of motion (39) for bare field operators $\hat{\Psi}_{i}^{0}\left(\vec{r}\right)$, equations (57) contain new

operators, such as $\hat{\omega}(\vec{r})$, $\hat{\omega}(\vec{r})/dt$, and $\vec{\nabla}\hat{\omega}(\vec{r}) = \hat{\vec{a}}(\vec{r})$, which characterize the CS gauge field. Similar to the case of a one-component 2DEG, in a two-component 2D e–h system, the quantum point vortices also give rise to vector potential $\vec{a}(\vec{r})$ and scalar potential $d\hat{\omega}/(cdt)$, which appear supplementary to vector potential $\vec{A}(\vec{r})$ of the external magnetic field. However, as noted above, they depend on the difference of the density operators $\hat{\rho}(\vec{r}) = \hat{\rho}_e(\vec{r}) - \hat{\rho}_h(\vec{r})$ due to different signs of the electrical charges of electrons and holes.

In the case under discussion, vector potential $\vec{a}(\vec{r})$ cannot compensate vector potential $\vec{A}(\vec{r})$ created by an external magnetic field. Chern–Simons vector potential $\vec{a}(\vec{r})$ vanishes in the mean-field approximation, if the average densities $\langle\rho_e\rangle$ and $\langle\rho_h\rangle$ coincide. Nevertheless, numbers ϕ of the quantum point vortices attached to each electron and each hole can be different from zero; in the zero-order approximation, the composite particles will be subjected only to an external magnetic field. In the zero-order approximation, they undergo the Landau quantization under the influence of an external magnetic field and will undergo perturbations in the next orders of the perturbation theory. In addition to the equations of motion (57) characterizing the time evolution of dressed field operators, we need a Hamiltonian describing a 2D e–h system in the presence of the CS gauge field. It can be easily obtained by substituting bare field operators $\hat{\Psi}_i^{0+}(\vec{r})$ and $\hat{\Psi}_i^0(\vec{r})$ into Hamiltonian (37) by the dressed field operators

$$\hat{\Psi}_e^0(\vec{r}) = u(\vec{r})\hat{\Psi}_e(\vec{r}),\ \hat{\Psi}_h^0(\vec{r}) = u^+(\vec{r})\hat{\Psi}_h(\vec{r}),\ \hat{\Psi}_e^{0+}(\vec{r}) = \hat{\Psi}_e^+(\vec{r})\hat{u}^+(\vec{r}),$$

$$\hat{\Psi}_h^{0+}(\vec{r}) = \hat{\Psi}_h^+(\vec{r})\hat{u}(\vec{r}),\ \hat{u}(\vec{r}) = e^{\frac{ie}{\hbar c}\hat{\omega}(\vec{r})},\ \hat{u}^+(\vec{r}) = e^{-\frac{ie}{\hbar c}\hat{\omega}(\vec{r})}. \tag{58}$$

For example, the first two terms of Hamiltonian (37) are transformed as follows:

$$\hat{K}^0 = \frac{\hbar^2}{2m_e}\int d^2\vec{r}'\hat{\Psi}_e^{0+}(\vec{r}')\left(-i\vec{\nabla}' + \frac{e}{\hbar c}\vec{A}(\vec{r})\right)^2\hat{\Psi}_e^0(\vec{r}') +$$

$$+\frac{\hbar^2}{2m_h}\int d^2\vec{r}'\hat{\Psi}_h^{0+}(\vec{r}')\left(-i\vec{\nabla}' - \frac{e}{\hbar c}\vec{A}(\vec{r})\right)^2\hat{\Psi}_h^0(\vec{r}') =$$

$$= \frac{\hbar^2}{2m_e}\int d^2\vec{r}'\hat{\Psi}_e^+(\vec{r}')e^{-\frac{ie}{\hbar c}\hat{\omega}(\vec{r}')}\left(-i\vec{\nabla}' + \frac{e}{\hbar c}\vec{A}(\vec{r}')\right)^2 e^{\frac{ie}{\hbar c}\hat{\omega}(\vec{r}')}\hat{\Psi}_e(\vec{r}') +$$

$$+\frac{\hbar^2}{2m_h}\int d^2\vec{r}'\hat{\Psi}_h^+(\vec{r}')e^{\frac{ie}{\hbar c}\hat{\omega}(\vec{r}')}\left(-i\vec{\nabla}' - \frac{e}{\hbar c}\vec{A}(\vec{r}')\right)^2 e^{-\frac{ie}{\hbar c}\hat{\omega}(\vec{r}')}\hat{\Psi}_h^0(\vec{r}') =$$

$$= \frac{\hbar^2}{2m_e}\int d^2\vec{r}'\hat{\Psi}_e^+(\vec{r}')\left(-i\vec{\nabla}' + \frac{e}{\hbar c}\vec{A}(\vec{r}') + \frac{e}{\hbar c}\hat{\vec{a}}(\vec{r}')\right)^2\hat{\Psi}_e(\vec{r}') + \tag{59}$$

$$+\frac{\hbar^2}{2m_h}\int d^2\vec{r}'\hat{\Psi}_h^+(\vec{r}')\left(-i\vec{\nabla}' - \frac{e}{\hbar c}\vec{A}(\vec{r}') - \frac{e}{\hbar c}\hat{\vec{a}}(\vec{r}')\right)^2\hat{\Psi}_h(\vec{r}') = \hat{K}$$

$$\hat{\vec{a}}(\vec{r}') = \vec{\nabla}'\hat{\omega}(\vec{r}'),$$

where we use relationships (55):

$$
e^{-\frac{ie}{\hbar c}\hat{\omega}(\vec{r}')}\left(-i\vec{\nabla}' + \frac{e}{\hbar c}\vec{A}(\vec{r}')\right)^2 = \left(-i\vec{\nabla}' + \frac{e}{\hbar c}\vec{A}(\vec{r}') + \frac{e}{\hbar c}\hat{\vec{a}}(\vec{r}')\right)^2 e^{-\frac{ie}{\hbar c}\hat{\omega}(\vec{r}')},
$$

$$
e^{\frac{ie}{\hbar c}\hat{\omega}(\vec{r}')}\left(-i\vec{\nabla}' - \frac{e}{\hbar c}\vec{A}(\vec{r}')\right)^2 = \left(-i\vec{\nabla}' - \frac{e}{\hbar c}\vec{A}(\vec{r}') - \frac{e}{\hbar c}\hat{\vec{a}}(\vec{r}')\right)^2 e^{\frac{ie}{\hbar c}\hat{\omega}(\vec{r}')}.
$$

(60)

Hamiltonian $\hat{H}^0_{Coul}$ of the Coulomb interaction of bare electrons and holes can be transcribed in the dressed field operator representation, taking into account that

$$
\hat{\rho}^0_i(\vec{r}) = \hat{\Psi}^{0+}_i(\vec{r})\hat{\Psi}^0_i(\vec{r}) = \hat{\rho}(\vec{r}) = \hat{\Psi}^+_i(\vec{r})\hat{\Psi}_i(\vec{r}), \ \ i = e, h,
$$

$$
\hat{H}^0_{Coul} = \hat{H}_{Coul}.
$$

(61)

The Hamiltonian of the e–h system in the presence of the CS gauge field looks as

$$
\hat{H} = \hat{K} + \hat{H}_{Coul} = \frac{\hbar^2}{2m_e}\int d^2\vec{r}'\hat{\Psi}^+_e(\vec{r}')\left(-i\vec{\nabla}' + \frac{e}{\hbar c}\vec{A}(\vec{r}') + \frac{e}{\hbar c}\hat{\vec{a}}(\vec{r}')\right)^2 \hat{\Psi}_e(\vec{r}') +
$$

$$
+ \frac{\hbar^2}{2m_h}\int d^2\vec{r}'\hat{\Psi}^+_h(\vec{r}')\left(-i\vec{\nabla}' - \frac{e}{\hbar c}\vec{A}(\vec{r}') - \frac{e}{\hbar c}\hat{\vec{a}}(\vec{r}')\right)^2 \hat{\Psi}_h(\vec{r}') +
$$

$$
+ \frac{1}{2}\int d^2\vec{r}'\int d^2\vec{r}'' V_{Coul}(\vec{r}' - \vec{r}'')\hat{\Psi}^+_e(\vec{r}')\hat{\rho}_e(\vec{r}'')\hat{\Psi}_e(\vec{r}') +
$$

$$
+ \frac{1}{2}\int d^2\vec{r}'\int d^2\vec{r}'' V_{Coul}(\vec{r}' - \vec{r}'')\hat{\Psi}^+_h(\vec{r}')\hat{\rho}_h(\vec{r}'')\hat{\Psi}_h(\vec{r}') -
$$

$$
- \int d^2\vec{r}'\int d^2\vec{r}'' V_{Coul}(\vec{r}' - \vec{r}'')\hat{\Psi}^+_e(\vec{r}')\hat{\rho}_h(\vec{r}'')\hat{\Psi}_e(\vec{r}').
$$

(62)

Hamiltonian (62) is much more complicated than its bare counterpart (37), because it contains a nonlinear form of vector potential operator $\hat{\vec{a}}(\vec{r}')$ created by the CS gauge field. To obtain equations of motion for dressed field operators, we start with the Schrodinger equations for electrons and holes

$$
i\hbar\frac{d\hat{\Psi}_i(\vec{r})}{dt} = \left[\hat{\Psi}_i(\vec{r}), \hat{H}\right], \ \ i = e, h.
$$

(63)

In this case, it is necessary to calculate commutation relations of the field operators with operator $\hat{\vec{a}}(\vec{r}')$

$$\left[\hat{\Psi}_e(\vec{r}), \hat{a}(\vec{r}\,')\frac{e}{\hbar c}\right] = -\phi\vec{\nabla}'\theta(\vec{r}\,'-\vec{r})\hat{\Psi}_e(\vec{r}),$$

$$\left[\hat{\Psi}_h(\vec{r}), \hat{a}(\vec{r}\,')\frac{e}{\hbar c}\right] = \phi\vec{\nabla}'\theta(\vec{r}\,'-\vec{r})\hat{\Psi}_h(\vec{r}),$$

$$\left[\hat{\Psi}_e^+(\vec{r}), \hat{a}(\vec{r}\,')\frac{e}{\hbar c}\right] = \phi\vec{\nabla}'\theta(\vec{r}\,'-\vec{r})\hat{\Psi}_e^+(\vec{r}),$$

$$\left[\hat{\Psi}_h^+(\vec{r}), \hat{a}(\vec{r}\,')\frac{e}{\hbar c}\right] = -\phi\vec{\nabla}'\theta(\vec{r}\,'-\vec{r})\hat{\Psi}_h^+(\vec{r}),$$

$$\left[\hat{\Psi}_i(\vec{r}), \hat{a}(\vec{r})\right] = \left[\hat{\Psi}_i^+(\vec{r}), \hat{a}(\vec{r})\right] = 0, \ i = e - h,$$

$$\vec{\nabla}'\theta(\vec{r}\,'-\vec{r})\Big|_{\vec{r}-\vec{r}\,'} = 0.$$

(64)

Using these equations, we can write

$$\hat{\Psi}_e(\vec{r})\left(-i\vec{\nabla}' + \frac{e}{\hbar c}\vec{A}(\vec{r}\,') + \frac{e}{\hbar c}\hat{a}(\vec{r}\,')\right)^2 =$$

$$= \left(-i\vec{\nabla}' + \frac{e}{\hbar c}\vec{A}(\vec{r}\,') + \frac{e}{\hbar c}\hat{a}(\vec{r}\,') - \phi\vec{\nabla}'\theta(\vec{r}\,'-\vec{r})\right)^2 \hat{\Psi}_e(\vec{r}),$$

$$\hat{\Psi}_h(\vec{r})\left(-i\vec{\nabla}' - \frac{e}{\hbar c}\vec{A}(\vec{r}\,') - \frac{e}{\hbar c}\hat{a}(\vec{r}\,')\right)^2 =$$

$$= \left(-i\vec{\nabla}' - \frac{e}{\hbar c}\vec{A}(\vec{r}\,') - \frac{e}{\hbar c}\hat{a}(\vec{r}\,') - \phi\vec{\nabla}'\theta(\vec{r}\,'-\vec{r})\right)^2 \hat{\Psi}_h(\vec{r}),$$

$$\hat{\Psi}_e^+(\vec{r})\left(-i\vec{\nabla}' + \frac{e}{\hbar c}\vec{A}(\vec{r}\,') + \frac{e}{\hbar c}\hat{a}(\vec{r}\,')\right)^2 =$$

$$= \left(-i\vec{\nabla}' + \frac{e}{\hbar c}\vec{A}(\vec{r}\,') + \frac{e}{\hbar c}\hat{a}(\vec{r}\,') + \phi\vec{\nabla}'\theta(\vec{r}\,'-\vec{r})\right)^2 \hat{\Psi}_e^+(\vec{r}),$$

(65)

$$\hat{\Psi}_h^+(\vec{r})\left(-i\vec{\nabla}' - \frac{e}{\hbar c}\vec{A}(\vec{r}\,') - \frac{e}{\hbar c}\hat{a}(\vec{r}\,')\right)^2 =$$

$$= \left(-i\vec{\nabla}' - \frac{e}{\hbar c}\vec{A}(\vec{r}\,') - \frac{e}{\hbar c}\hat{a}(\vec{r}\,') + \phi\vec{\nabla}'\theta(\vec{r}\,'-\vec{r})\right)^2 \hat{\Psi}_h^+(\vec{r}).$$

It should be borne in mind that dressed field operators $\hat{\Psi}_i(\vec{r})$ and $\hat{\Psi}_i^+(\vec{r})$ obey the Fermi or Bose statistics with commutation relations

$$\hat{\Psi}_i(\vec{r})\hat{\Psi}_j^+(\vec{r}) \pm \hat{\Psi}_j^+(\vec{r})\hat{\Psi}_i(\vec{r}) = \delta_{ij}\delta^2(\vec{r}-\vec{r}\,'), \quad (F)$$

$$\hat{\Psi}_i(\vec{r})\hat{\Psi}_j^+(\vec{r}) \pm \hat{\Psi}_j^+(\vec{r})\hat{\Psi}_i(\vec{r}) = 0, \qquad (B)$$

(66)

and all the formulas obtained above are valid in both cases. For example, to derive the next commutation relations, we have to use both formulas (65) and (66) as follows:

$$
\left[\hat{\Psi}_e(\vec{r}), \hat{\Psi}_e^+(\vec{r}') \left(-i\vec{\nabla}' + \frac{e}{\hbar c}\vec{A}(\vec{r}') + \frac{e}{\hbar c}\hat{a}(\vec{r}') \right)^2 \hat{\Psi}_e(\vec{r}') \right] =
$$

$$
= \delta^2(\vec{r}-\vec{r}')\left(-i\vec{\nabla}' + \frac{e}{\hbar c}\vec{A}(\vec{r}') + \frac{e}{\hbar c}\hat{a}(\vec{r}') \right)^2 \hat{\Psi}_e(\vec{r}') + \left(\phi\vec{\nabla}'\theta(\vec{r}'-\vec{r}) \right)^2 \times
$$

$$
\times \hat{\rho}_e(\vec{r}')\hat{\Psi}_e(\vec{r}),
$$

$$
\left[\hat{\Psi}_e(\vec{r}), \frac{\hbar^2}{2m_e}\int d^2\vec{r}'\hat{\Psi}_e^+(\vec{r}')\left(-i\vec{\nabla}' + \frac{e}{\hbar c}\vec{A}(\vec{r}') + \frac{e}{\hbar c}\hat{a}(\vec{r}') \right)^2 \hat{\Psi}_e(\vec{r}') \right] =
$$

$$
= \frac{\hbar^2}{2m_e}\left(-i\vec{\nabla} + \frac{e}{\hbar c}\vec{A}(\vec{r}) + \frac{e}{\hbar c}\hat{a}(\vec{r}) \right)^2 \hat{\Psi}_e(\vec{r}) +
$$

$$
+\phi^2 \frac{\hbar^2}{2m_e}\int d^2\vec{r}' \frac{\hat{\rho}_e(\vec{r}')}{\left|\vec{r}-\vec{r}'\right|^2} \hat{\Psi}_e(\vec{r}) -
$$

$$
-\phi\frac{\hbar^2}{m_e}\int d^2\vec{r}'\vec{\nabla}'\theta(\vec{r}'-\vec{r})\hat{\Psi}_e^+(\vec{r}')\left(-i\vec{\nabla}' + \frac{e}{\hbar c}\vec{A}(\vec{r}') + \frac{e}{\hbar c}\hat{a}(\vec{r}') \right)\hat{\Psi}_e(\vec{r}')\hat{\Psi}_e(r),
$$

$$
\left[\hat{\Psi}_h(\vec{r}), \frac{\hbar^2}{2m_h}\int d^2\vec{r}'\hat{\Psi}_h^+(\vec{r}')\left(-i\vec{\nabla}' - \frac{e}{\hbar c}\vec{A}(\vec{r}') - \frac{e}{\hbar c}\hat{a}(\vec{r}') \right)^2 \hat{\Psi}_h(\vec{r}') \right] =
$$

$$
= \frac{\hbar^2}{2m_h}\left(-i\vec{\nabla} - \frac{e}{\hbar c}\vec{A}(\vec{r}) - \frac{e}{\hbar c}\hat{a}(\vec{r}) \right)^2 \hat{\Psi}_h(\vec{r}) +
$$

$$
+\phi^2 \frac{\hbar^2}{2m_h}\int d^2\vec{r}' \frac{\hat{\rho}_h(\vec{r}')}{\left|\vec{r}-\vec{r}'\right|^2} \hat{\Psi}_h(\vec{r}) - \tag{67}
$$

$$
-\phi\frac{\hbar^2}{m_h}\int d^2\vec{r}'\vec{\nabla}'\theta(\vec{r}'-\vec{r})\hat{\Psi}_h^+(\vec{r}')\left(-i\vec{\nabla}' - \frac{e}{\hbar c}\vec{A}(\vec{r}') - \frac{e}{\hbar c}\hat{a}(\vec{r}') \right)\hat{\Psi}_h(\vec{r}')\hat{\Psi}_h(r).
$$

Here, we took into account the properties described by formulas (64) and the equalities written below

$$
\vec{\nabla}'\vec{A}(\vec{r}') = \vec{\nabla}'\hat{a}(\vec{r}') = 0; \quad \left[\hat{\Psi}_i(\vec{r}), \hat{a}(\vec{r}) \right] = 0;
$$

$$
\left(\vec{\nabla}'\theta(\vec{r}'-\vec{r}) \right)^2 = \frac{1}{\left|\vec{r}-\vec{r}'\right|^2}; \quad \Delta'\theta(\vec{r}'-\vec{r}) = 0. \tag{68}
$$

Both integrals proportional to ϕ in equation (67) can be transformed introducing the dressed current density operators for electrons $\hat{\vec{J}}_e(\vec{r})$ and holes $\hat{\vec{J}}_h(\vec{r})$ and the respective continuity equations as follows:

$$\hat{\vec{J}}_e(\vec{r}) = \frac{\hbar^2}{2m_e i}\left(\hat{\Psi}_e^+(\vec{r})\vec{\nabla}\hat{\Psi}_e(\vec{r}) - \vec{\nabla}\hat{\Psi}_e^+(\vec{r})\hat{\Psi}_e(\vec{r})\right) +$$

$$+\left(\frac{e}{m_e c}\vec{A}(\vec{r}) + \frac{e}{m_e c}\hat{\vec{a}}(\vec{r})\right)\hat{\rho}_e(\vec{r}),$$

$$\hat{\vec{J}}_h(\vec{r}) = \frac{\hbar^2}{2m_h i}\left(\hat{\Psi}_h^+(\vec{r})\vec{\nabla}\hat{\Psi}_h(\vec{r}) - \vec{\nabla}\hat{\Psi}_h^+(\vec{r})\hat{\Psi}_h(\vec{r})\right) - \tag{69}$$

$$-\left(\frac{e}{m_h c}\vec{A}(\vec{r}) + \frac{e}{m_h c}\hat{\vec{a}}(\vec{r})\right)\hat{\rho}_h(\vec{r}).$$

$$\frac{d\hat{\rho}_e(\vec{r})}{dt} = -\vec{\nabla}\hat{\vec{J}}_e(\vec{r}), \frac{d\hat{\rho}_h(\vec{r})}{dt} = -\vec{\nabla}\hat{\vec{J}}_h(\vec{r}).$$

Condition $\Delta'\theta(\vec{r}' - \vec{r}) = 0$ is useful for a simple integral transformation:

$$-i\int d^2\vec{r}'\vec{\nabla}'\theta(\vec{r}' - \vec{r})\hat{\Psi}_i^+(\vec{r}')\vec{\nabla}'\hat{\Psi}_i(\vec{r}') =$$

$$= \frac{i}{2}\int d^2\vec{r}'\vec{\nabla}'\theta(\vec{r}' - \vec{r})\left(\nabla'\hat{\Psi}_i^+(\vec{r}')\hat{\Psi}_i(\vec{r}') - \hat{\Psi}_i^+(\vec{r}')\vec{\nabla}'\hat{\Psi}_i(\vec{r}')\right).$$

The obtained relations allow us to write the above-mentioned integrals in equations (67) as follows:

$$\phi\frac{\hbar^2}{m_e}\int d^2\vec{r}'\vec{\nabla}'\theta(\vec{r}' - \vec{r})\hat{\Psi}_e^+(\vec{r}')\left(-i\vec{\nabla}' + \frac{e}{\hbar c}\vec{A}(\vec{r}') + \frac{e}{\hbar c}\hat{\vec{a}}(\vec{r}')\right)\hat{\Psi}_e(\vec{r}')\hat{\Psi}_e(\vec{r}) =$$

$$= \phi\hbar\int d^2\vec{r}'\vec{\nabla}'\theta(\vec{r}' - \vec{r})\hat{\vec{J}}_e(\vec{r}')\hat{\Psi}_e(\vec{r}) = -\phi\hbar\int d^2\vec{r}'\theta(\vec{r}' - \vec{r})\times$$

$$\times\vec{\nabla}'\hat{\vec{J}}_e(\vec{r}')\hat{\Psi}_e(\vec{r}) = \phi\hbar\int d^2\vec{r}'\theta(\vec{r}' - \vec{r})\frac{d\hat{\rho}_e(\vec{r}')}{dt}\hat{\Psi}_e(\vec{r}) = -\frac{e}{c}\frac{d\hat{\omega}_e(\vec{r})}{dt}\hat{\Psi}_e(\vec{r}),$$

$$\phi\frac{\hbar^2}{m_h}\int d^2\vec{r}'\vec{\nabla}'\theta(\vec{r}' - \vec{r})\hat{\Psi}_h^+(\vec{r}')\left(-i\vec{\nabla}' - \frac{e}{\hbar c}\vec{A}(\vec{r}') - \frac{e}{\hbar c}\hat{\vec{a}}(\vec{r}')\right)\hat{\Psi}_h(\vec{r}')\hat{\Psi}_h(\vec{r}) = \tag{70}$$

$$= \phi\hbar\int d^2\vec{r}'\vec{\nabla}'\theta(\vec{r}' - \vec{r})\hat{\vec{J}}_h(\vec{r}')\hat{\Psi}_h(\vec{r}) = -\phi\hbar\int d^2\vec{r}'\theta(\vec{r}' - \vec{r})\times$$

$$\times\vec{\nabla}'\hat{\vec{J}}_h(\vec{r}')\hat{\Psi}_h(\vec{r}) = \phi\hbar\int d^2\vec{r}'\theta(\vec{r}' - \vec{r})\frac{d\hat{\rho}_h(\vec{r}')}{dt}\hat{\Psi}_h(\vec{r}) = -\frac{e}{c}\frac{d\hat{\omega}_h(\vec{r})}{dt}\hat{\Psi}_h(\vec{r}),$$

$$\hat{\omega}_i(\vec{r}) = -\frac{\phi e}{\alpha}\int d^2\vec{r}'\theta(\vec{r} - \vec{r}')\hat{\rho}_i(\vec{r}'), \quad i = e, h.$$

Combining the results expressed by equations (67)–(70), we can formulate the main result of our calculations:

$$\left[\hat{\Psi}_e(\vec{r}), \frac{\hbar^2}{2m_e} \int d^2\vec{r}' \hat{\Psi}_e^+(\vec{r}') \left(-i\vec{\nabla}' + \frac{e}{\hbar c} \vec{A}(\vec{r}') + \frac{e}{\hbar c} \hat{\vec{a}}(\vec{r}') \right)^2 \hat{\Psi}_e(\vec{r}') \right] =$$

$$= \frac{\hbar^2}{2m_e} \left(-i\vec{\nabla}' + \frac{e}{\hbar c} \vec{A}(\vec{r}) + \frac{e}{\hbar c} \hat{\vec{a}}(\vec{r}) \right)^2 \hat{\Psi}_e(\vec{r}) + \phi^2 \frac{\hbar^2}{2m_e} \int d^2\vec{r}' \frac{\hat{\rho}_e(\vec{r}')}{|\vec{r} - \vec{r}'|^2} \times$$

$$\times \hat{\Psi}_e(\vec{r}) + \frac{e}{c} \frac{d\hat{\omega}_e(\vec{r})}{dt} \hat{\Psi}_e(\vec{r}),$$

$$\left[\hat{\Psi}_h(\vec{r}), \frac{\hbar^2}{2m_h} \int d^2\vec{r}' \hat{\Psi}_h^+(\vec{r}') \left(-i\vec{\nabla}' - \frac{e}{\hbar c} \vec{A}(\vec{r}') - \frac{e}{\hbar c} \hat{\vec{a}}(\vec{r}') \right)^2 \hat{\Psi}_h(\vec{r}') \right] =$$

$$= \frac{\hbar^2}{2m_h} \left(-i\vec{\nabla}' - \frac{e}{\hbar c} \vec{A}(\vec{r}) - \frac{e}{\hbar c} \hat{\vec{a}}(\vec{r}) \right)^2 \hat{\Psi}_h(\vec{r}) + \phi^2 \frac{\hbar^2}{2m_h} \int d^2\vec{r}' \frac{\hat{\rho}_h(\vec{r}')}{|\vec{r} - \vec{r}'|^2} \times \tag{71}$$

$$\times \hat{\Psi}_h(\vec{r}) + \frac{e}{c} \frac{d\hat{\omega}_h(\vec{r})}{dt} \hat{\Psi}_h(\vec{r}).$$

In a similar way, the following commutations can be derived:

$$\left[\hat{\Psi}_e(\vec{r}), \frac{\hbar^2}{2m_h} \int d^2\vec{r}' \hat{\Psi}_h^+(\vec{r}') \left(-i\vec{\nabla}' - \frac{e}{\hbar c} \vec{A}(\vec{r}') - \frac{e}{\hbar c} \hat{\vec{a}}(\vec{r}') \right)^2 \hat{\Psi}_h(\vec{r}') \right] =$$

$$= \phi^2 \frac{\hbar^2}{2m_h} \int d^2\vec{r}' \frac{\hat{\rho}_h(\vec{r}')}{|\vec{r} - \vec{r}'|^2} \hat{\Psi}_e(\vec{r}) - \frac{e}{c} \frac{d\hat{\omega}_h(\vec{r})}{dt} \hat{\Psi}_e(\vec{r}),$$

$$\left[\hat{\Psi}_h(\vec{r}), \frac{\hbar^2}{2m_e} \int d^2\vec{r}' \hat{\Psi}_h^+(\vec{r}') \left(-i\vec{\nabla}' + \frac{e}{\hbar c} \vec{A}(\vec{r}') + \frac{e}{\hbar c} \hat{\vec{a}}(\vec{r}') \right)^2 \hat{\Psi}_e(\vec{r}') \right] = \tag{72}$$

$$= \phi^2 \frac{\hbar^2}{2m_e} \int d^2\vec{r}' \frac{\hat{\rho}_e(\vec{r}')}{|\vec{r} - \vec{r}'|^2} \hat{\Psi}_h(\vec{r}) - \frac{e}{c} \frac{d\hat{\omega}_e(\vec{r})}{dt} \hat{\Psi}_h(\vec{r}).$$

Formulas (71) and (72) constitute the basis for the main statements:

$$\left[\hat{\Psi}_e(\vec{r}),\hat{K}\right] = \frac{\hbar^2}{2m_e}\left(-i\vec{\nabla} + \frac{e}{\hbar c}\vec{A}(\vec{r}) + \frac{e}{\hbar c}\hat{\vec{a}}(\vec{r})\right)^2 \hat{\Psi}_e(\vec{r}) +$$

$$+\phi^2 \hat{L}(\vec{r})\hat{\Psi}_e(\vec{r}) + \frac{e}{c}\frac{d\hat{\omega}(\vec{r})}{dt}\hat{\Psi}_e(\vec{r}),$$

$$\left[\hat{\Psi}_h(\vec{r}),\hat{K}\right] = \frac{\hbar^2}{2m_h}\left(-i\vec{\nabla} - \frac{e}{\hbar c}\vec{A}(\vec{r}) - \frac{e}{\hbar c}\hat{\vec{a}}(\vec{r})\right)^2 \hat{\Psi}_h(\vec{r}) +$$

$$+\phi^2 \hat{L}(\vec{r})\hat{\Psi}_h(\vec{r}) - \frac{e}{c}\frac{d\hat{\omega}(\vec{r})}{dt}\hat{\Psi}_h(\vec{r}),$$

$$\hat{L}(\vec{r}) = \frac{\hbar^2}{2m_e}\int d^2\vec{r}\,'\frac{\hat{\rho}_e(\vec{r}\,')}{\left|\vec{r}-\vec{r}\,'\right|^2} + \frac{\hbar^2}{2m_h}\int d^2\vec{r}\,'\frac{\hat{\rho}_h(\vec{r}\,')}{\left|\vec{r}-\vec{r}\,'\right|^2},$$

$$\hat{\omega}(\vec{r}) = \hat{\omega}_e(\vec{r}) - \hat{\omega}_h(\vec{r}), \hat{\omega}_i(\vec{r}) = -\frac{\phi e}{\alpha}\int d^2\vec{r}\,'\theta(\vec{r}-\vec{r}\,')\hat{\rho}_i(\vec{r}\,').$$

(73)

The obtained results confirm the earlier derived equations of motion (57) for dressed field operators.

4. Influence of the CS Gauge Field on the Energy Level of a Two-Dimensional Magnetoexciton

In the Landau gauge description, two-dimensional electrons and holes are described as free particles moving along the in-plane x-axis and undergoing the Landau quantization along the in-plane *y*-axis perpendicular to the *x*-axis. The free motion is represented by the plane wave functions with unidimensional (1D) wave vectors p and q as quantum numbers, whereas the Landau quantization takes place in the form of harmonic oscillations around the gyration points situated on the *y*-axis at distances pl_0^2 and $-ql_0^2$ from the origin, where l_0 is the magnetic length. The displacements of electrons and holes in the opposite parts of the *y*-axis are due to the different signs of their electric charges. The single particle wave functions corresponding to the lowest energy level of the Landau quantization are as follows:

$$\varphi_e(\vec{r}) = \frac{e^{ipx}}{\sqrt{L_x l_0 \sqrt{\pi}}}\exp\left[-\frac{\left(y - pl_0^2\right)^2}{2l_0^2}\right],$$

$$\varphi_h(\vec{r}) = \frac{e^{iqx}}{\sqrt{L_x l_0 \sqrt{\pi}}}\exp\left[-\frac{\left(y + ql_0^2\right)^2}{2l_0^2}\right].$$

(74)

Here, we consider the 2D layer with a surface area of $S = L_x L_y$. Wave functions (74) belong to the lowest levels of Landau quantization with quantum numbers $n_e = n_h = 0$; in this paper, we do not consider the excited Landau quantization energy levels. This approach is known

as the lowest Landau Levels (LLL) approximation and labels n_e and n_h at electron field operators a_p^+, a_p and hole field operators b_p^+, b_p will be dropped. Bare electron and hole field operators obey the Fermi statistics. The energies of the electrons and holes are $\hbar\omega_{c,i}/2$, with $i = e, h$, where $\hbar\omega_{c,i}$ are the cyclotron frequencies. The electron and hole field operators in the coordinate representation in the LLL–approximation are as follows:

$$\hat{\Psi}_e(\vec{r}) = \frac{1}{\sqrt{L_x l_0 \sqrt{\pi}}} \sum_p e^{ipx} \exp\left[-\frac{\left(y - pl_0^2\right)^2}{2l_0^2} \right] a_p,$$

$$\hat{\Psi}_h(\vec{r}) = \frac{1}{\sqrt{L_x l_0 \sqrt{\pi}}} \sum_q e^{iqx} \exp\left[-\frac{\left(y + ql_0^2\right)^2}{2l_0^2} \right] b_q,$$

(75)

where we introduced the electron and hole density operators

$$\hat{\rho}_e(\vec{r}) = \hat{\Psi}_e^+(\vec{r})\hat{\Psi}_e(\vec{r}) = \frac{1}{L_x l_0 \sqrt{\pi}} \sum_{p,q} e^{i(p-q)x} \exp\left[-\frac{\left(y - pl_0^2\right)^2}{2l_0^2} - \frac{\left(y - ql_0^2\right)^2}{2l_0^2} \right] a_q^+ a_p,$$

$$\hat{\rho}_h(\vec{r}) = \hat{\Psi}_h^+(\vec{r})\hat{\Psi}_h(\vec{r}) = \frac{1}{L_x l_0 \sqrt{\pi}} \sum_{u,v} e^{i(u-v)x} \exp\left[-\frac{\left(y + ul_0^2\right)^2}{2l_0^2} - \frac{\left(y + vl_0^2\right)^2}{2l_0^2} \right] b_v^+ b_u,$$

$$\hat{\rho}(\vec{r}) = \hat{\rho}_e(\vec{r}) - \hat{\rho}_h(\vec{r}).$$

(76)

Here, the density operator of the e–h system $\hat{\rho}(\vec{r})$ was defined as the algebraic sum of the electron and hole density operators. This algebraic sum determines the CS gauge field vector potential operator $\hat{\vec{a}}(\vec{r})$ as follows:

$$\hat{\vec{a}}(\vec{r}) = -\frac{\phi e}{\alpha} \int d^2\vec{r}' \vec{\nabla}_{\vec{r}} \theta(\vec{r} - \vec{r}') \hat{\rho}(\vec{r}'),$$

$$\frac{e^2}{2m_e c^2} \hat{\vec{a}}^2(\vec{r}) = -\frac{\hbar^2\phi^2}{2m_e} \int d^2\vec{r}' \int d^2\vec{r}'' \frac{(\vec{r} - \vec{r}')(\vec{r} - \vec{r}'')}{|\vec{r} - \vec{r}'|^2 |\vec{r} - \vec{r}''|^2} \hat{\rho}(\vec{r}')\hat{\rho}(\vec{r}''),$$

$$\theta(\vec{r} - \vec{r}') = \arctan\left(\frac{y - y'}{x - x'} \right);$$

(77)

$$\vec{\nabla}_{\vec{r}} = \vec{e}_x \frac{\partial}{\partial x} + \vec{e}_y \frac{\partial}{\partial x},$$

$$\vec{\nabla}_{\vec{r}} \theta(\vec{r} - \vec{r}') = \frac{-\vec{e}_x(y - y') + \vec{e}_y(x - x')}{|\vec{r} - \vec{r}'|^2}, \quad \alpha = \frac{e^2}{\hbar c} = \frac{1}{137}.$$

To determine the influence of the CS gauge field on the 2D magnetoexciton energy level, it is

necessary to calculate the average value of Hamiltonian (62) using magnetoexciton wave function $\left| \Psi_{ex}(\vec{k}) \right\rangle$, which was obtained in [13]:

$$\left| \Psi_{ex}(\vec{k}) \right\rangle = \Psi_{ex}^+(\vec{k}) \left| 0 \right\rangle,$$

$$\Psi_{ex}^+(\vec{k}) = \frac{1}{\sqrt{N}} \sum_t e^{ik_y t l_0^2} a_{t+\frac{k_x}{2}}^+ b_{-t+\frac{k_x}{2}}^+, \tag{78}$$

$$N = \frac{S}{2\pi l_0^2}.$$

First, we will discuss the influence of the terms in Hamiltonian (62), which are proportional to the square of CS vector potential $\hat{\vec{a}}(\vec{r})$ in the form

$$\frac{e^2}{2m_{e,h}c^2} \int d^2\vec{r}' \hat{\Psi}_{e,h}^+(\vec{r}) \hat{\vec{a}}^2(\vec{r}) \hat{\Psi}_{e,h}(\vec{r}). \tag{79}$$

Their average value calculated with the magnetoexciton wave function with wave vector $\vec{k} = 0$ is as follows:

$$\Delta_e = \left\langle \Psi_{ex}(0) \left| \frac{e}{2m_e c^2} \int d^2\vec{r} \hat{\Psi}_e^+(\vec{r}) \hat{\vec{a}}^2(\vec{r}) \hat{\Psi}_e(\vec{r}) \right| \Psi_{ex}(0) \right\rangle =$$

$$= \frac{\hbar^2 \phi^2}{m_e l_0^2} \cdot \frac{1}{8\pi^2} \int d^2\vec{\rho}_1 \int d^2\vec{\rho}_2 \frac{\vec{\rho}_1 \cdot \vec{\rho}_2}{\vec{\rho}_1^2 \cdot \vec{\rho}_2^2} \exp\left\{ -\frac{1}{4}\left(\vec{\rho}_1^2 + \vec{\rho}_2^2 + |\vec{\rho}_1 - \vec{\rho}_2|^2 \right) + \right.$$

$$\left. + \frac{i}{2}[\vec{\rho}_2 \times \vec{\rho}_1] \right\} = \frac{\hbar^2 \phi^2}{m_e l_0^2} \cdot \frac{1}{8\pi^2} \int_0^\infty d\rho_1 \int_0^\infty d\rho_2 \int_0^{2\pi} d\varphi_1 \int_0^{2\pi} d\varphi_2 \cos(\varphi_1 - \varphi_2) \times \tag{80}$$

$$\times \exp\left\{ -\frac{1}{2}\left[\rho_1^2 + \rho_2^2 - \rho_1\rho_2 \cos(\varphi_1 - \varphi_2) \right] + \frac{i}{2}\rho_2\rho_1 \sin(\varphi_1 - \varphi_2) \right\}.$$

The Fourier series expansions of exponents $\exp(iz\sin t)$ and $\exp(z\cos t)$ contain coefficients expressed in terms of Bessel functions $J_\nu(z)$ and modified Bessel functions $I_\nu(z)$ [14]:

$$e^{iz\sin t} = J_0(z) + 2\sum_{k=1}^\infty \left[J_{2k}(z)\cos 2kt + iJ_{2k-1}(z)\sin(2k-1)t \right],$$

$$e^{z\cos t} = I_0(z) + 2\sum_{k=1}^\infty I_k(z)\cos kt. \tag{81}$$

Substitution of them into the previous expression leads to its transformation

$$\Delta_e = \frac{\hbar^2\phi^2}{m_e l_0^2}\left\{\frac{1}{4\pi^2}\int_0^\infty d\rho_1\int_0^\infty d\rho_2 \exp\left[-\frac{1}{2}\left(\rho_1^2+\rho_2^2\right)\right]J_0\left(\frac{1}{2}\rho_1\cdot\rho_2\right)\times\right.$$

$$\times I_1\left(\frac{1}{2}\rho_1\cdot\rho_2\right)+\frac{1}{2}\sum_{m=1}^\infty\int_0^\infty d\rho_1\int_0^\infty d\rho_2 \exp\left[-\frac{1}{2}\left(\rho_1^2+\rho_2^2\right)\right]J_{2m}\left(\frac{1}{2}\rho_1\cdot\rho_2\right)\times$$

$$\left.\times\left[I_{2m+1}\left(\frac{1}{2}\rho_1\cdot\rho_2\right)+I_{2m-1}\left(\frac{1}{2}\rho_1\cdot\rho_2\right)\right]\right\}. \tag{82}$$

In subsequent calculations, we will use integrals with two Bessel functions [14]:

$$\int_0^\infty x^{\alpha-1}e^{-px^2}J_\mu(bx)I_\nu(cx)\,dx = \frac{b^\mu c^\nu (p)^{-\frac{(\alpha+\mu+\nu)}{2}}}{2^{\mu+\nu+1}\Gamma(\mu+1)}\times$$

$$\times\sum_{k=0}^\infty\frac{1}{k!}\Gamma\left[\begin{matrix}k+\dfrac{(\alpha+\mu+\nu)}{2}\\ \nu+k+1\end{matrix}\right]\left(\frac{c}{2p}\right)^{2k}\cdot {}_2F_1\left(-k,-(\nu+k),\mu+1,-\frac{b^2}{c^2}\right). \tag{83}$$

Their applications give rise to energy shift Δ_e of the magnetoexciton energy level

$$\Delta_e = \frac{\hbar^2\phi^2}{m_e l_0^2}\left\{\frac{1}{16\pi^2}\sum_{k=0}^\infty\frac{1}{2^k(k+1)}\times\right.$$

$$\times {}_2F_1\left(-k,-(k+1),1,-1\right)+\frac{1}{2}\sum_{m=1}^\infty\sum_{k=0}^\infty\frac{(2m+k)!}{2^{4m+k+2}\Gamma(2m+1)}\times$$

$$\times\frac{1}{k!(k+2m+1)}\cdot {}_2F_1\left(-k,-(k+2m+1),2m+1,-1\right)+$$

$$+\frac{1}{2}\sum_{m=1}^\infty\sum_{k=0}^\infty\frac{(2m+k-1)!}{2^{4m+k}\Gamma(2m+1)}\frac{1}{k!}\times$$

$$\left.\times {}_2F_1\left(-k,-(k+2m-1),2m+1,-1\right)\right\}. \tag{84}$$

It is possible to estimate, along with terms (79) containing the square of the CS vector potential $\hat{\vec{a}}^2(\vec{r})$, the contribution of the mixed term proportional to the scalar product of two vector potentials $\hat{\vec{a}}(\vec{r})$ and $\vec{A}(\vec{r})$. It is expressed by the average value

$$\left\langle\Psi_{ex}\left(\vec{k}\right)\left|\frac{e^2}{m_e c^2}\int d^2\vec{r}\,'\hat{\Psi}_e^+\left(\vec{r}\,'\right)\hat{\vec{a}}^2\left(\vec{r}\,'\right)\vec{A}\left(\vec{r}\,'\right)\hat{\Psi}_e\left(\vec{r}\,'\right)\right|\Psi_{ex}\left(\vec{k}\right)\right\rangle =$$

$$= \frac{\hbar eB\phi}{4\pi^2 m_e c l_0^4 N}\cdot\int d^2\vec{r}\,'\int d^2\vec{r}\,''\frac{y'\left(y'-y''\right)}{\left|\vec{r}\,'-\vec{r}\,''\right|^2}\exp\left[-\frac{1}{2}\left|\frac{\vec{r}\,'-\vec{r}\,''}{l_0}\right|^2 -\right.$$

$$\left.-\frac{\left(\vec{k}l_0\right)^2}{2}+\left(y'-y''\right)k_x-\left(x'-x''\right)k_y\right]. \tag{85}$$

The shift of the magnetoexciton energy level Δ'_e at point $\vec{k} = 0$ due this term can be calculated exactly:

$$\Delta'_e = \frac{\hbar e B \phi}{4 m_e c}. \tag{86}$$

In the case of electron effective mass m_e equal to free electron mass m_0 at a magnetic field strength of $B = 10\,\text{T}$ and $\phi = 1$, the shift of the magnetoexciton energy level at point $\vec{k} = 0$ due to the influence of the CS gauge field can be estimated as $\Delta'_e = 1/4\,\text{meV}$.

5. Conclusions

The origin of the CS gauge field, as well as quantum point vortices, is associated with a collective motion in the 2D system, where the main role is played by angles $\theta(\vec{r} - \vec{r}')$ created by reference vectors $(\vec{r} - \vec{r}')$ with a selected axis. The reference vectors describe positions of the particles at points $\vec{r}'$ with density operator $\hat{\rho}(\vec{r}')$. The coherent summation of the angles weighted with the density operator gives rise to phase operator $\hat{\omega}(\vec{r})$, whereas the gradients of the angles and their weighted summation give rise to vector potential $\hat{\vec{a}}(\vec{r})$ of the CS gauge field.

Unitary transformation operators $\exp(\pm i e \hat{\omega}(\vec{r})/(\hbar c))$ acting on bare electron and hole field operators lead to the formation of dressed field operators representing composite particles with number ϕ of attached quantum point vortices. Dressed field operators obey the Fermi or Bose statistics depending on the parity of numbers ϕ of attached vortices. A Hamiltonian describing the composite particles and their interactions through the Coulomb forces and under the influence of the CS gauge field has been deduced; equations of motion for dressed field operators have been derived. The influence of the CS gauge field on the energy levels of 2D magnetoexcitons has been estimated.

References

[1] S. S. Chern and J. Simons, Ann. Math. 99, 48 (1974).
[2] B. I. Halperin, P. A. Lee, and N. Read, Phys. Rev. B 47, 7312 (1993).
[3] N. Read, Phys. Rev. B 58, 16262 (1998).
[4] F. Wilczek, Phys. Rev. Lett. 48, 1144, (1982); 49, 957 (1982).
[5] S. C. Zhang, T. H. Hansson, and S. Kivelson, Phys. Rev. Lett. 62, 82 (1989).
[6] J. K. Jain, Phys. Rev. Lett. 63, 199 (1989).
[7] G. Dunne, R. Jackiw, and C. Trugenberger, Phys. Rev. D 41, 661 (1990).
[8] R. Jackiw and So Young Pi, Phys. Rev. D 42, 3500 (1990).
[9] S. A. Moskalenko and V. A. Moskalenko, Mold. J. Phys. Sci. 16 (3–4), 133 (2017).
[10] S. A. Moskalenko, V. A. Moskalenko, D. F. Digor, and I. A. Lelyakov, Mold. J. Phys. Sci. 16 (3–4), 173 (2017).
[11] S. A. Moskalenko and V. A. Moskalenko, Mold. J. Phys. Sci. 17 (1–2), 41 (2018).

[12] S. A. Moskalenko, V. A. Moskalenko, I. V. Podlesny, and I. A. Zubac, Semiconductors 53, 2055 (2019).

[13] S. A. Moskalenko, V. A. Moskalenko, P. I. Khadzhi, I. V. Podlesny, M. A. Liberman, and I. A. Zubac, Mold. J. Phys. Sci. 17, 52 (2018).

[14] A. P. Prudnikov, Yu. A. Brychkov, and O. I. Marichev, Integrals and Series: Special Functions, Gordon and Breach Science Publishers, New York, 1986.

PARTIAL WAVE BASIS ADAPTED TO EXTERIOR BOUNDARY CONDITIONS OF AN ELASTIC PLATE

Sergiu Cojocaru

Department of Theoretical Physics,
Horia Hulubei National Institute for Physics and Nuclear Engineering,
077125 Magurele, Romania
E-mail: scojocaru@theory.nipne.ro

Abstract

An approach to describing normal elastic vibration modes in confined systems is presented. In a standard treatment of the problem, the displacement field is represented by a superposition of partial waves of a general form, e.g., plane waves. The unknown coefficients of superposition are then obtained from the equation of motion and the full set of boundary conditions. In the proposed approach, the functional form of partial waves is chosen in such a way as to satisfy the boundary conditions on exterior surfaces identically, i.e., even if the unknown quantities determined by the remaining constraints are found in an approximation, numerically or analytically. Some examples of solutions for composite elastic plates are discussed to illustrate the efficiency of the approach and its relevance for applications.

Keywords: wave propagation, confined systems, boundary conditions

Rezumat

Este prezentată o metodă nouă pentru descrierea modurilor proprii de vibrații elastice în sisteme confinate. Într-o abordare standard a problemei, câmpul de deplasări este reprezentat de o superpoziție a undelor parțiale de formă generală, de exemplu, unde plane. Coeficienții necunoscuți ai superpoziției sunt apoi obținuți din ecuația de mișcare și din setul complet de condiții la limită. În abordarea propusă, forma funcțională a undelor parțiale este construită astfel încât condițiile la limită de pe suprafețele exterioare să fie îndeplinite în mod identic, adică chiar dacă valorile necunoscute, ce urmeaza a fi determinate de restul constrângerilor, sunt obținute într-o aproximare, numerică sau analitică. Eficiența și relevanța metodei pentru aplicații este demonstrată prin câteva exemple de soluții pentru plăci elastice compuse.

Cuvinte cheie: propagarea undelor, sisteme confinate, condiții la limită

1. Introduction

We consider an infinite composite plate with layers of homogeneous materials labeled with index $\gamma = 1, 2, \ldots$ (e.g., layer thickness h_γ) and briefly outline the general formalism [e.g., 1–5]. The stress–strain relation in a given material is as follows:

$$\Sigma_{ij,\gamma} = \lambda_\gamma \delta_{ij} \varepsilon_{kk} + 2\mu_\gamma \varepsilon_{ij}$$

where δ_{ij} is the Kronecker symbol, $i = 1, 2, 3$, double index implies summation, λ, μ are the two Lamé stiffness parameters and the strain tensor at a given point $r = (x_1{=}x,\ x_2{=}y,\ x_3{=}z)$ and time t is defined by respective space derivatives of the displacement field $U(r, t)$ components

$$\varepsilon_{km}(r, t) = \left(\frac{\partial U_k}{\partial x_m} + \frac{\partial U_m}{\partial x_k} \right) \Big/ 2 .$$

Solutions of elastodynamic equations

$$\rho \frac{\partial^2 U_i(r,t)}{\partial t^2} = \frac{\partial \Sigma_{ij}(r,t)}{\partial r_j} \tag{1}$$

are represented by a superposition of normal modes propagating in-plane with the wave vector $q_{//}$ and indexed by $n = 1, 2, \ldots$:

$$u_n\big(z, q, \omega_n(q)\big) \exp(iqx - i\omega_n t) \frac{dq}{2\pi}.$$

Here we have set the x - axis collinear to the wave vector, so that $r q_{//} = q_x x + q_y y = qx$ and plate thickness is spanned by the z - axis. Equations are then decoupled according to the polarization pattern into the shear horizontal, $u = (0, u_y, 0)$, and mixed (shear vertical and longitudinal [6]), $u = (u_x, 0, u_z)$. The latter, which are referred to as Rayleigh-Lamb waves, are examined in the following. The relevant components of the stress tensor are as follows:

$$i\sigma_{zz}(z) = \left(\lambda_\gamma + 2\mu_\gamma \right) \frac{\partial (iu_z)}{\partial z} - \lambda_\gamma q u_x,$$

$$\sigma_{xz}(z) = \mu_\gamma \left(\frac{\partial u_x}{\partial z} + q(iu_z) \right).$$

From Eq. (1) we then obtain for the mode amplitudes

$$s_\gamma^2 \frac{\partial^2 u_{x,\gamma}}{\partial z^2} - \ell_\gamma^2 q^2 w_\gamma^2 u_{x,\gamma} + \left(\ell_\gamma^2 - s_\gamma^2\right)q \frac{\partial \mathrm{i} u_{z,\gamma}}{\partial z} = 0,$$

$$\ell_\gamma^2 \frac{\partial^2 \mathrm{i} u_{z,\gamma}}{\partial z^2} - s_\gamma^2 q^2 v_\gamma^2 \mathrm{i} u_{z,\gamma} - \left(\ell_\gamma^2 - s_\gamma^2\right)q \frac{\partial u_{x,\gamma}}{\partial z} = 0, \tag{2}$$

where $\ell = \sqrt{(\lambda + 2\mu)/\rho}$, $s = \sqrt{\mu/\rho}$ are the bulk longitudinal and transverse sound velocities in the respective materials of mass density ρ. Quantities v_γ and w_γ defined as

$$w_\gamma = \sqrt{1 - \left(c/\ell_\gamma\right)^2}, v_\gamma = \sqrt{1 - \left(c/s_\gamma\right)^2}.$$

contain phase velocities $c = \omega/q$ of normal modes (n index is dropped).

2. Basis Set Functions

Equations (2) are to be solved by specifying the displacement and/or stress fields at the external boundaries, $z - d_\gamma = 0$. In addition, these fields are subject to continuity conditions at the interfaces between different media: for a double layer, the interface is chosen at $z = 0$, so that the upper bound is at $z = d_1 = h_1$ and the lower bound at $z = d_2 = -h_2$. The standard approach is to use a universal basis set of incoming and outgoing plane waves, which does not depend on details of the structure. It is well suited for treating systems embedded in an infinite medium, and the problem is then mapped into one of a linear algebra for the expansion coefficients by applying the complete set of boundary conditions. Dispersion curves are obtained from the respective secular equation in an analytical or numerical approximation. The proposed alternative necessarily produces the same frequency spectrum; however, the basis set functions will not be universal, since their functional form is required to transform some of the boundary conditions into identities. To this end, equations defining the exterior surfaces are introduced as arguments of the basis set functions. In this case, exterior boundary conditions allow reducing the number of independent coefficients by the number of constraint equations. As a consequence, the expressions of the wave fields in terms of these independent algebraic variables automatically satisfy the above boundary conditions.

For flat boundaries, we can start with the following general form of the partial wave superposition:

$$u_{x,\gamma} = \xi_{w,\gamma}\sinh\left((z - d_\gamma)qw_\gamma\right) + \xi_{v,\gamma}\sinh\left((z - d_\gamma)qv_\gamma\right) + \theta_{w,\gamma}\cosh\left((z - d_\gamma)qw_\gamma\right)$$
$$+ \theta_{v,\gamma}\cosh\left((z - d_\gamma)qv_\gamma\right).$$

$$\mathrm{i} u_{z,\gamma} = \zeta_{w,\gamma}\sinh\left((z - d_\gamma)qw_\gamma\right) + \zeta_{v,\gamma}\sinh\left((z - d_\gamma)qv_\gamma\right) + \eta_{w,\gamma}\cosh\left((z - d_\gamma)qw_\gamma\right)$$
$$+ \eta_{v,\gamma}\cosh\left((z - d_\gamma)qv_\gamma\right).$$

It is evident that the substitution of these expressions into the governing equations (2) reduces the number of variables by half (in what follows, the γ index identifying the layers will be occasionally dropped for brevity):

$$\eta_w = w\xi_w, \ \eta_v = \xi_v/v, \ \theta_w = \zeta_w/w, \ \theta_v = \zeta_v v.$$

By introducing the new notations

$$X = \xi_v, \ Y = \theta_v, R = \xi_w, S_\gamma = \theta_w,$$

we get the final general form of the partial wave expansion:

$$u_{x,\gamma} = X_\gamma \sinh\left((z - d_\gamma)qv_\gamma\right) + Y_\gamma \cosh\left((z - d_\gamma)qv_\gamma\right)$$
$$+ S_\gamma \cosh\left((z - d_\gamma)qw_\gamma\right) + R_\gamma \sinh\left((z - d_\gamma)qw_\gamma\right) \tag{3}$$

$$iu_{z,\gamma} = \frac{1}{v_\gamma}\left[X_\gamma \cosh\left((z - d_\gamma)qv_\gamma\right) + Y_\gamma \sinh\left((z - d_\gamma)qv_\gamma\right)\right]$$
$$+ w_\gamma \left[R_\gamma \cosh\left((z - d_\gamma)qw_\gamma\right) + S_\gamma \sinh\left((z - d_\gamma)qw_\gamma\right)\right] \tag{4}$$

$$\frac{i\sigma_{zz,\gamma}(q,z)}{2\mu_\gamma q} = X_\gamma \sinh qv_\gamma(z - d_\gamma) + Y_\gamma \cosh qv_\gamma(z - d_\gamma)$$
$$+ \frac{(1+v_\gamma^2)}{2}\left[R_\gamma \sinh qw_\gamma(z - d_\gamma) + S_\gamma \cosh\left((z - d_\gamma)qw_\gamma\right)\right] \tag{5}$$

$$\frac{v_\gamma \sigma_{xz,\gamma}(q,z)}{(1+v_\gamma^2)\mu_\gamma q} = X_\gamma \cosh qv_\gamma(z - d_\gamma) + Y_\gamma \sinh qv_\gamma(z - d_\gamma)$$
$$+ \frac{2v_\gamma w_\gamma}{(1+v_\gamma^2)}\left[R_\gamma \cosh qw_\gamma(z - d_\gamma) + S_\gamma \sinh qw_\gamma(z - d_\gamma)\right]. \tag{6}$$

We have also used the following identity:

$$\ell_\gamma(1 - w_\gamma^2) = s_\gamma(1 - v_\gamma^2).$$

3. Traction-Free Plate

To illustrate the procedure, we first consider the case of a traction-free composite plate. Relations that come from the zero stress requirement $\sigma(z = d_\beta) = 0$ reduce the number of variables by four when applied to the general equations (5, 6)

$$S_\beta = -Y_\beta \frac{2}{1+v_\beta^2}, R_\beta = -X_\beta \frac{1+v_\beta^2}{2v_\beta w_\beta},$$

here, $\gamma = \beta = 1,2 = \text{top, bottom}$. Note that if we consider a bilayered plate, then S, R variables are completely removed from consideration and we are left with only $\{X_\gamma, Y_\gamma\}$ as unknowns. It can then be verified that, in terms of these variables, the traction-free BC are indeed satisfied automatically:

$$u_x(z) = X_\gamma \left(\sinh\left((z-d_\gamma)qv_\gamma\right) - \frac{(1+v_\gamma^2)}{2v_\gamma w_\gamma} \sinh\left((z-d_\gamma)qw_\gamma\right) \right)$$
$$+Y_\gamma \left(\cosh\left((z-d_\gamma)qv_\gamma\right) - \frac{2}{(1+v_\gamma^2)} \cosh\left((z-d_\gamma)qw_\gamma\right) \right), \tag{7}$$

$$iu_z(z) = \frac{1}{v_\gamma} X_\gamma \left(\cosh\left((z-d_\gamma)qv_\gamma\right) - \frac{(1+v_\gamma^2)}{2} \cosh\left((z-d_\gamma)qw_\gamma\right) \right)$$
$$+\frac{1}{v_\gamma} Y_\gamma \left[\sinh\left((z-d_\gamma)qv_\gamma\right) - \frac{2w_\gamma v_\gamma}{(1+v_\gamma^2)} \sinh\left((z-d_\gamma)qw_\gamma\right) \right], \tag{8}$$

$$\frac{i\sigma_{zz}(z)}{2\mu_\gamma q} = X_\gamma \left(\sinh\left((z-d_\gamma)qv_\gamma\right) - \frac{(1+v_\gamma^2)^2}{4v_\gamma w_\gamma} \sinh\left((z-d_\gamma)qw_\gamma\right) \right)$$
$$+Y_\gamma \left(\cosh\left((z-d_\gamma)qv_\gamma\right) - \cosh\left((z-d_\gamma)qw_\gamma\right) \right), \tag{9}$$

$$\frac{v_\gamma \sigma_{xz}(z)}{(1+v_\gamma^2)\mu_\gamma q} = X_\gamma \left(\cosh\left((z-d_\gamma)qv_\gamma\right) - \cosh\left((z-d_\gamma)qw_\gamma\right) \right)$$
$$+Y_\gamma \left(\sinh\left((z-d_\gamma)qv_\gamma\right) - \frac{4v_\gamma w_\gamma}{(1+v_\gamma^2)^2} \sinh\left((z-d_\gamma)qw_\gamma\right) \right). \tag{10}$$

The physical meaning of variables $\{X_\beta, Y_\beta\}$ is that they are proportional to the components of the displacement field on the outer surfaces. The secular equation is then a result of matching the continuity of the four fields in Eqs. (7)–(10) at the interface $z = 0$. It can be verified that the complete set of equations, including normalization of the amplitudes, coincides with those obtained in [7]. If a plate is composed of a larger number of materials, then the inner layers will be subject to continuity conditions only and the R_γ and S_γ variables for $\gamma \neq \beta$ will be included.

It is also instructive to see how Lamb equations for a homogeneous free plate and their symmetry properties emerge as a limiting case of the obtained expressions, $\beta = 1,2$. To avoid lengthier arguments, we take $d_1 = -d_2 = h$ so that the interface $z = 0$ is at the middle plane.

In this case, equations resulting from continuity of (7)–(10) are decoupled into a 2×2 pair with symmetric and antisymmetric combinations of variables: $\{X_2 + X_1, Y_2 - Y_1\}$ for Eqs. (7, 9) and $\{X_2 - X_1, Y_2 + Y_1\}$ for Eqs. (8, 10). Namely,

$$(X_2 + X_1)\left(\sinh(hqv) - \frac{(1 + v^2)}{2vw}\sinh(hqw)\right)$$

$$+ (Y_2 - Y_1)\left(\cosh(hqv) - \frac{2}{(1 + v^2)}\cosh(hqw)\right) = 0,$$

$$\mu q\left((X_2 + X_1)\left(\sinh(hqv) - \frac{(1+v^2)^2}{4vw}\sinh(hqw)\right) + (Y_2 - Y_1)(\cosh(hqv) - \cosh(hqw))\right) = 0,$$

and

$$\frac{(X_2 - X_1)}{v}\left(\cosh(hqv) - \frac{(1 + v^2)}{2}\cosh(hqw)\right)$$

$$+ \frac{(Y_2 + Y_1)}{v}\left(\sinh(hqv) - \frac{2wv}{(1 + v^2)}\sinh(hqw)\right) = 0,$$

$$\frac{\mu q(1 + v^2)}{v}\left((X_2 - X_1)(\cosh(hqv) - \cosh(hqw))\right.$$

$$\left. + (Y_2 + Y_1)\left(\sinh(hqv) - \frac{4vw}{(1 + v^2)^2}\sinh(hqw)\right)\right) = 0.$$

Solutions are given by equating the product of the two determinants to zero. It is obvious the two systems of equations above are different and can only produce the same eigenvalues at the points of intersection between the two corresponding sets of dispersion curves. Therefore, nontrivial solutions of the secular equation, i.e., the whole set of four equations, are generally found when one of the 2×2 pairs has a non-trivial and the other has a trivial solution. This gives only two possibilities: $\{X_2 = X_1, Y_2 = -Y_1\}$ (A) and $\{X_2 = -X_1, Y_2 = Y_1\}$ (S). In this case, we find for the case (A):

$$\frac{\mu q(1 - v^2)}{vw(1 + v^2)}\left(4\,(vw)\cosh(hqw)\sinh(hqv) - (1 + v^2)^2\sinh(hqw)\cosh(hqv)\right) = 0,$$

and for the case (S)

$$\frac{\mu q(1 - v^2)}{v^2(1 + v^2)}\left(4\,(vw)\cosh(hqv)\sinh(hqw) - (1 + v^2)^2\sinh(hqv)\cosh(hqw)\right) = 0.$$

These expressions are the well-known Lamb equations. Their transformation properties with respect to reflection in the $z-$ plane are then easily obtained from the explicit form of the fields in $(7)-(10)$:

$$\{X_2 = X_1, Y_2 = -Y_1\}_A: u_x(z) = -u_x(-z), \sigma_{zz}(z) = -\sigma_{zz}(-z);$$
$$u_z(z) = u_z(-z), \sigma_{xz}(z) = \sigma_{xz}(-z). \tag{11}$$

$$\{X_2 = -X_1, Y_2 = Y_1\}_S: u_x(z) = u_x(-z), \sigma_{zz}(z) = \sigma_{zz}(-z);$$
$$u_z(z) = -u_z(-z), \sigma_{xz}(z) = -\sigma_{xz}(-z). \tag{12}$$

Thus, we have *derived* the transformation properties of the Lamb modes directly from our approach instead of introducing symmetry relations (11, 12) from the outset, based on general theorems, in order to derive the Lamb equations in the end.

4. Clamped Plate

To illustrate the approach using another example, let us now examine a bilayered plate clamped at the top and bottom surfaces, $\gamma = \beta$. From zero-displacement condition applied to the general expressions in (3) and (4) we find:

$$S_\beta = -Y_\beta, R_\beta = -X_\beta \frac{1}{v_\beta w_\beta}.$$

It can be seen again that the exterior boundary conditions at $z = d_\gamma$ are accounted for by our basis set.

$$u_x(z) = X_\gamma \left(\sinh\left((z - d_\gamma)\mathrm{qv}_\gamma\right) - \frac{1}{v_\gamma w_\gamma} \sinh\left((z - d_\gamma)\mathrm{qw}_\gamma\right) \right)$$
$$+ Y_\gamma \left(\cosh\left((z - d_\gamma)\mathrm{qv}_\gamma\right) - \cosh\left((z - d_\gamma)\mathrm{qw}_\gamma\right) \right),$$

$$\mathrm{i}u_z(z) = \frac{1}{v_\gamma} X_\gamma \left(\cosh\left((z - d_\gamma)\mathrm{qv}_\gamma\right) - \cosh\left((z - d_\gamma)\mathrm{qw}_\gamma\right) \right)$$
$$+ \frac{1}{v_\gamma} Y_\gamma \left(\sinh\left((z - d_\gamma)\mathrm{qv}_\gamma\right) - v_\gamma w_\gamma \sinh\left((z - d_\gamma)\mathrm{qw}_\gamma\right) \right),$$

$$\frac{i\sigma_{zz}(z)}{2\mu_\gamma q} = X_\gamma\left(\sinh\left((z-d_\gamma)qv_\gamma\right) - \frac{(1+v_\gamma^2)}{2v_\gamma w_\gamma}\sinh\left((z-d_\gamma)qw_\gamma\right)\right)$$

$$+Y_\gamma\left(\cosh\left((z-d_\gamma)qv_\gamma\right) - \frac{(1+v_\gamma^2)}{2}\cosh\left((z-d_\gamma)qw_\gamma\right)\right),$$

$$\frac{v_\gamma\sigma_{xz}(z)}{(1+v_\gamma^2)\mu_\gamma q} = X_\gamma\left(\cosh\left((z-d_\gamma)qv_\gamma\right) - \frac{2}{(1+v_\gamma^2)}\cosh\left((z-d_\gamma)qw_\gamma\right)\right)$$

$$+Y_\gamma\left(\sinh\left((z-d_\gamma)qv_\gamma\right) - \frac{2v_\gamma w_\gamma}{(1+v_\gamma^2)}\sinh\left((z-d_\gamma)qw_\gamma\right)\right).$$

Similarly to the case of a free plate, the final equations are obtained from continuity of the fields in the above expressions at the internal boundary $z = 0$. Likewise, the single layer limit leads to the decoupling of the secular equation into a 2×2 pair corresponding to S (Eq. (12)), and A modes (Eq. (11)), their spectra being determined by

(S)

$$\mu q\frac{1-v^2}{v^2}(\cosh(hqw)\sinh(hqv) - (vw)\sinh(hqw)\cosh(hqv)) = 0,$$

(A)

$$\mu q\frac{1-v^2}{vw}(\cosh(hqv)\sinh(hqw) - (vw)\sinh(hqv)\cosh(hqw)) = 0.$$

These are essentially the same secular equations as analyzed in [8]. On the other side, as noted above, our expressions for the wave amplitudes appear to differ from those of a standard representation. However, it can be shown that, for the frequencies coinciding with eigenvalues of the secular equations, the amplitudes become equivalent to the standard form.

5. Summary

The main advantage of the approach is that it offers a simple and direct route to the irreducible form of the secular equation. This simplification has allowed to obtain a complete analytic solution describing the long wavelength region of the vibration spectrum [7] of a two-layered system. In this case, the set of independent material parameters is 8-dimensional: the longitudinal and transverse sound velocities in the two media, respective mass densities and thicknesses of the layers. These systems are quite common in a broad range of applications;

however, experimental or numerical exploration of the full parametric space is hopeless in view of understanding and engineering of their properties. Nevertheless, the above approach reveals an unexpected evolution with the layer thickness of the slowest (flexural) mode of the velocity spectrum and other features [9], which could be exploited for specific purposes. The approach also provides an interesting new perspective of extension to confined systems of different geometries. It may also be of interest in implementing various approximation schemes, since, unlike other approaches, some of the boundary conditions are satisfied identically from outset and approximation errors can only show up, e.g., in a mismatch of the fields at interfaces.

References

[1] S. Cojocaru, Mold. J. Phys. Sci. 17, 75 (2018).

[2] B. A. Auld, Acoustic Fields and Waves in Solids, 2nd ed., Krieger, Malabar, FL, 1990.

[3] L. M. Brekhovskikh and O. A. Godin, Acoustics of Layered Media I, Springer, New York, 1990.

[4] J. L. Rose, Ultrasonic Waves in Solid Media, Cambridge University Press, Cambridge, 2004.

[5] J. L. Rose, Ultrasonic Guided Waves in Solid Media, Cambridge University Press, New York, 2014).

[6] H. Ezawa, Ann. Phys. (N.Y.) 67, 438 (1971).

[7] S. Cojocaru, Wave Motion 92, 102430 (2020).

[8] E. Kausel, P. Malischewsky, and J. Barbosa, Wave Motion 56, 22 (2015).

[9] S. Cojocaru, Unusual Size Dependence of Acoustic Properties in Layered Nanostructures, In: I. Tiginyanu, V. Sontea, and S. Railean (Eds.) 4th Int. Conf. on Nanotechnologies and Biomedical Engineering, ICNBME 2019, IFMBE Proc., vol 77, Springer, Cham. https://doi.org/10.1007/978-3-030-31866-6_5

MODELING OF A NANOCYLINDER

Serghei A. Baranov[1, 2]

[1]*Institute of Applied Physics, str. Academiei 5, Chisinau, MD-2028 Republic of Moldova*
[2]*Shevchenko Pridnestrov'e State University, str. 25 Oktyabrya 128, Tiraspol,
Republic of Moldova*
E-mail: baranov@phys.asm.md

Abstract

The results of the theory of modeling for obtaining nanocylinders have been described. A case of a nanocylinder whose diameters are shorter than the Tolman length has been considered. This important issue is taken into account in studying a nanocylinder for which, in the simplest model, the thickness of the interfacial layer cannot be determined because it supposedly has a small size. At the same time, it has been shown that the introduction of a special form of anisotropy energy makes it possible to analytically describe the origin of an interfacial layer whose sizes can be regarded as sizes comparable to the Tolman length.

Keywords: nanocylinder, Tolman length, Heisenberg model, Euler–Lagrange equations, instantons or skyrmions

Rezumat

Sunt descrise rezultatele teoriei modelării pentru obținerea nanocilindrilor. Am considerat un caz în care nanocilindrul are diametre mai mici decât lungimea Tolman. Această întrebare importantă este luată în considerare atunci când se studiază nanocilindrul pentru care în cel mai simplu model nu s-a putut distinge grosimea stratului interfacial datorită dimensiunii sale presupuse mici. În același timp, se arată că introducerea unei forme speciale de energie anizotropică permite o descriere analitică a originii unui strat interfacial ale cărui dimensiuni pot fi considerate ca dimensiuni comparabile cu lungimea Tolman.

Cuvinte cheie: nanocilindru, lungime Tolman, model Heisenberg, ecuații Euler-Lagrange, instantane sau skyrmions

1. Introduction

The modern statistical mechanics of curved interfaces, mainly spherical and cylindrical, is equally important to the simple thermodynamics of planar interfaces (maybe even more important). However, this statistical mechanics theory needs a more subtle analysis than the

thermodynamics of flat geometry, for which a great progress has been achieved in understanding the properties (for details see [1–5]).

The first studies of the effect of only one curvature on the properties of drops (Jung and Laplace) date back to the nineteenth century [1, 2]. Laplace considered a drop of radius *R* enclosing a homogeneous liquid-like phase (interior phase) separated from a homogeneous bulk vapor phase (exterior phase) by a mathematical dividing surface, where the density changes abruptly from a constant value inside the drop to a constant value outside; to provide the stability of the drop against the surface tension (regarded as a mechanical force) of the vapor–liquid interface, it is necessary to set up a pressure difference over the interface to balance the contracting force and maintain the system in equilibrium, i.e., the condition of mechanical equilibrium, which is referred to as the Laplace law (see [1–10]).

On the other hand, the curved interface theory with a Tolman's intermediate phase was based on sound thermodynamic arguments in the late 1940s (see [6]); however, it received little attention in electrochemistry (see, for example, [3–5]). After that, this theory was developed in [7–10]. We will not discuss all reviews; we can only mention many original papers and reviews [11–20]. Those studies are close to our research.

Below, we will consider a new theory [21–24] that takes into account the cylindrical shape and the intermediate phase. Moreover, the size of the intermediate phase can be arbitrary.

.

2. A Small Long Cylinder

We consider a case of the application theory [21–23], where nanoparticles have the form of a long cylinder. We used a cylindrical coordinate system for which the characteristic spin function [21, 22] is represented by angle function $\theta(r)$ about the cylinder axis *z*.

The free energy in this model can have the following form [21, 22]:

$$H_{g,c} = \frac{A}{2}\left[\theta'^2 + \frac{\sin^2\theta}{r^2}\right] + k_1 \frac{\sin^4\theta}{r^2} + ..., \tag{1}$$

where $\theta(r)$ is the angle between the cylinder axis and the magnetization vector; *r* is the radial coordinate, and k_1 is the second anisotropy constant.

The model kinetic energy in (1) is a classical analog of the exchange energy in the Heisenberg model for the two-dimensional space at the continuum approximation [21], which in our case corresponds to the infinite cylinder model [21, 22]. In this case, the kinetic energy in (1) coincides in form with the kinetic energy of the particle (in cylindrical coordinates). This fact is not casual because the model under consideration permits exact analytical solutions in the form of quasi-particles (nonlinear waves), which are referred to as instantons (or skyrmions [21, 22]). Note that, in our case, these quasi-particles are topological compositions, rather than dynamic particles. Therefore, in our case, the virtual kinetic energy of a topological instanton is meant by the kinetic energy.

We introduce a relative coordinate

$$\rho = \frac{r}{R_c}, \tag{2}$$

where R_c is the drop equilibrium radius.

In this case, there is a condition of $0 \leq \rho \leq 1$. The proposed continuum model of energy (1) actually appears to be a Heisenberg model, in which the interacting spins have the meaning of energy states of the particles associated with the constant exchange interaction A (with the dimension for the exchange energy [J/m]).

Using (1), it is simple to derive the Euler–Lagrange equation:

$$\theta''(\rho) + \frac{\theta'(\rho)}{\rho} - \frac{\sin\theta\cos\theta}{\rho^2} - k_1\frac{\sin^3\theta\cos\theta}{\rho^2} - ... = 0. \tag{3}$$

For simplicity, it is sufficient to use only a particular solution of this equation describing the nucleation process under simple boundary conditions:

$$\theta(\rho) = \begin{cases} \pi, & \rho = 0, \\ \dfrac{\pi}{2}, & \rho = 1. \end{cases} \tag{4}$$

The solutions of equations (3) and (4) are as follows:

$$\tan\left(\frac{\theta}{2}\right) \sim \frac{1}{\rho}\left[1 - k_1\rho^2 - ...\right], \tag{5}$$

$$k_1 < 1$$

$$\text{(if} \quad k_1 = 0, \quad \text{then} \quad \tan\left(\frac{\theta}{2}\right) = \frac{1}{\rho}), \tag{5a}$$

which is convenient for further analysis.

Let us introduce the model surface energy to obtain the Euler–Lagrange equations for the scale-invariant theory as well:

$$\theta_a''(\rho) + \frac{\theta_a'(\rho)}{\rho} - \frac{a^2\sin\theta_a\cos\theta_a}{\rho^2} = 0, \tag{6}$$

where a^2 is the ratio of the anisotropy energy to exchange interaction constant A. The a^2 parameter is determined in [21, 22]:

$$a^2 = \frac{B}{A} + 1, \tag{7}$$

with the determined anisotropy function (model as the Rapini modified potential (see [21, 22]):

$$\frac{B\sin^2\theta_a}{2\rho^2}, \tag{8}$$

where B is the positive energy quantity whose dimension coincides with A.

For agreement with the previous solution, we assume that, in (6), anisotropy does not occur at $B = 0$ and occurs at $B > 0$. The solution of equation (6) is as follows:

$$\tan\left(\frac{\theta_a}{2}\right) = \frac{1}{\rho^a}. \tag{9}$$

Note that solutions (5) and (9) analytically join; therefore, the indices are later omitted.

Let us consider one general solution (9). The diagram of this solution is shown in Figs. 1a and 1b.

It is easy to show that the $\theta(r)$ function has no point of inflection at $a = 1$ and $0 \leq \rho \leq 1$. This point appears only at $a > 1$. This means that the surface layer in our model can exist only at $a > 1$. In this case, a certain volume whose energy is the surface energy of the cylindrical particle can be chosen as a surface layer. For definiteness, we suppose, for example, that the surface layer begins to clearly manifest itself from a value of $a > 4$. Thus, we suppose that at $a = 1$ there is no anisotropy in the system, and the Tolman length actually coincides with the drop sizes. If $a \gg 1$, then, in the proposed model, the specific anisotropy is higher than the exchange interaction, and in the drop there appears a parameter (Tolman length) that characterizes the dimension of the interfacial region.
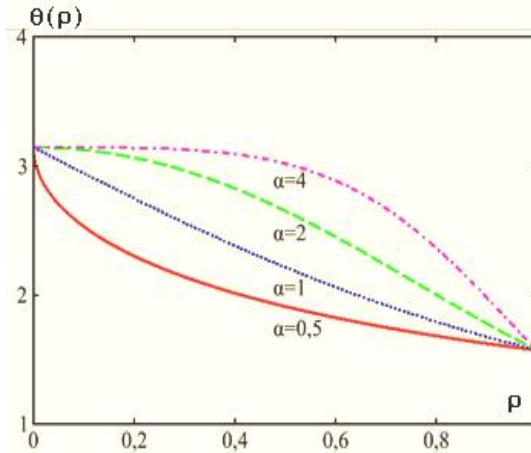
Fig. 1a. Diagrams of solution (9) at different values of parameter a (see [22]).
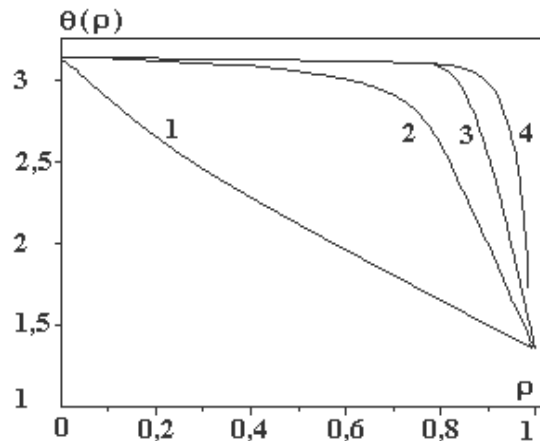
Fig. 1b. Diagrams of solution (9) at the different values of parameter a: $a = (1)$ 1, (2) 10, (3) 50, and (4) 100 (see [21]).

The case of $a < 1$ corresponds to the negative surface energy (in Fig. 1a, this case is shown for $a = 0.5$); it is not discussed in detail in this paper, because it is associated with the condensed phase instability.

The change in the free energy from the particle center to the particle surface can be estimated. This estimation allows the physical interpretation of the introduced parameters of the model and their comparison with conventional energy characteristics used to describe the nucleation process.

Let us initially consider the layer-by-layer change in this free energy of a cylindrical drop. Let us return to the formula for the energy that was used to derive the equation of motion. It is as follows: $E(r) = T + U$. Taking into account solution (9), we find that the kinetic energy is equal to the potential energy: $T = U$. This important result for the closed dynamic system is associated with the virial theorem for the finite motion; in our case, it is the test to verify whether this approach to the problem solution is correct. For the total full energy we have:

$$E(\rho) = T + U = 4A \left(\frac{a}{\rho} \right)^2 \frac{\rho^{2a}}{(1+\rho^{2a})^2}. \tag{10}$$

It follows from (10) that, at $a = 1$ and $r < 1$, the equality $E(r) = A$ is satisfied. If $B > 0$, then the cylinder surface energy tends to $Aa^2 \sim B$; the higher the B value, the sharper the limit. Thus, just this parameter B can be associated with the parameter of the specific thermodynamic surface energy that occurs in the thermodynamic theories (Gibbs, Tolman, etc.) provided that the dimension of these energies is different.
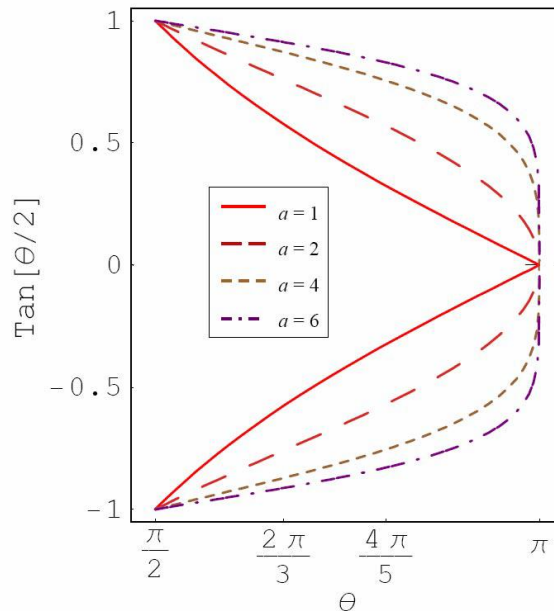
Fig. 2a. Plot for $\tan(\theta/2)$ as function of θ for different a values.
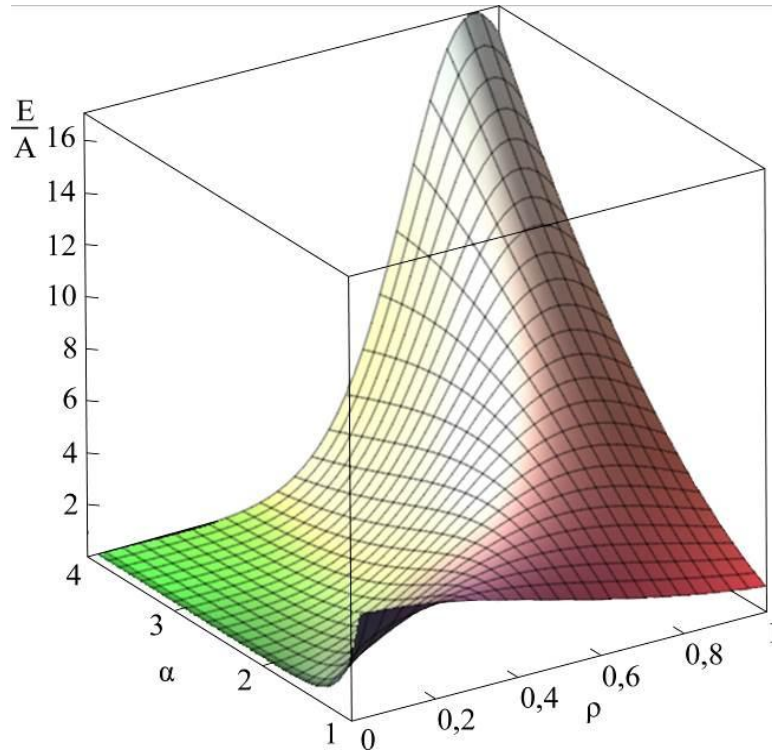
Fig. 2b. Dependence of energy on parameters *a* and ρ (see [22]).
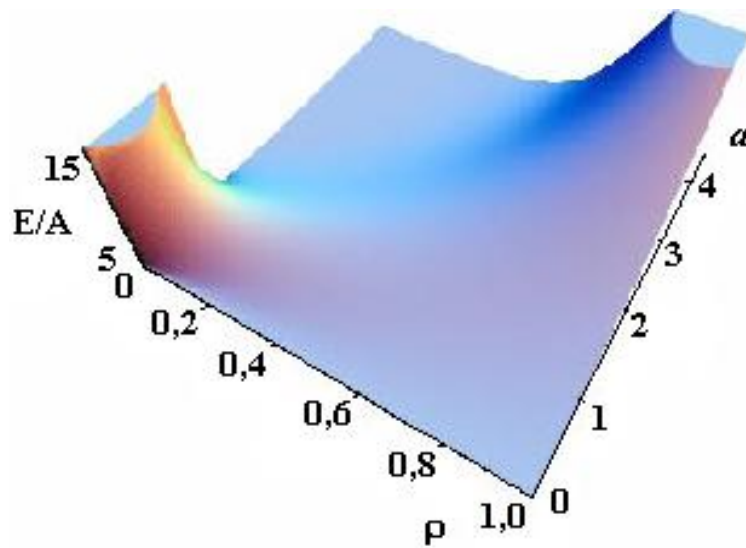
Fig. 2c. Dependence of energy on parameters *a* and ρ (see [21]).

A sharp rise in free energy (see Figs. 2b, 2c) depending on parameter *a* is identified with

the phase transition, which takes place in the system in the case of infinitely small anisotropy (for details see [21, 22]). To determine the total energy of the particle assigned to the cylinder length unit, an integral of $E(r)$ over the cylinder volume should be taken. Let us begin with a qualitative analysis of the model. Note that, for a particular case of $a = 1$ and $B = 0$, this integral should be equal to A (with an accuracy to the multiplier). In this case, there is no other energy in the system; here A is the only internal model energy of the system. In another limiting case, a certain high value of a is sufficient for the total energy to tend to the anisotropy energy B. In the general case, the total full specific energy (for the cylinder length unit) will be as follows:

$$W = 2\pi \int_0^1 E(\rho)\rho d\rho = 8\pi a^2 A \int_0^1 \frac{\rho^{2a-1} d\rho}{(1+\rho^{2a})^2} = 2\pi a A.$$

(11)

In the Cahn–Hilliard theory [22, 23], the activation barrier energy is in proportion to the geometric mean of two energy parameters:

$$E_c \sim \sqrt{AB}.$$

(11a)

Unlike the proposed theory, the Cahn–Hilliard theory is not scale-invariant, and the quantity B has a dimension of J/m^3. In our case, the integral formula derived from (11) for the activation energy has the same form; that is, the coincidence of these theories can be stated in calculating the mean activation energy (in the volume unit). Thus, we can deduce that the proposed theory qualitatively coincide with the Cahn–Hilliard theory. In terms of the Cahn–Hilliard theory, we obtain the same analytic structures [23]:

$$\text{tg}\theta(\rho)/2 = \exp\left[\pm(\rho-\rho_0)/r_{cc}\right].$$

(12)

(A)   (B)
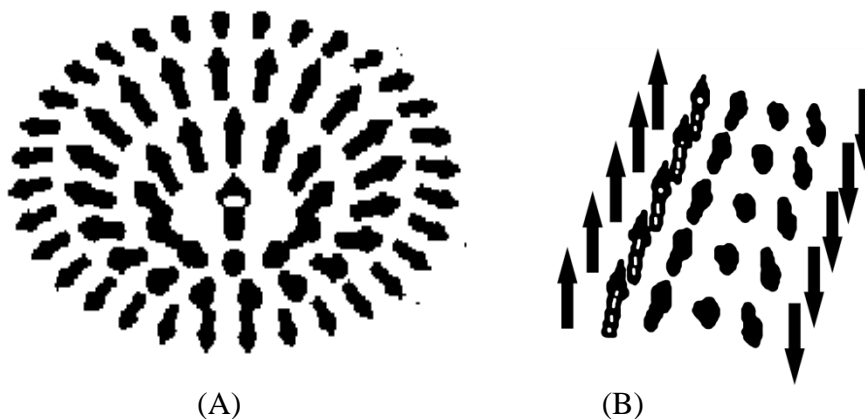
Fig. 3. Schematics representations of solution (9): (A) and (12): (B) in the form of a domain wall of energy vectors.

3. Physical Application

The previously introduced parameter a^2 (see (7)) can formally be less than $a = 1$ (in Fig. 1a, this case is shown for $a = 0.5$). This case can correspond to negative anisotropy energy, which can, for example, prevent the formation of a nanoparticle. Technologically, it is possible to initiate the formation of a nanoparticle, yet limit the nanoparticle growth.

Therefore, it is of interest to consider the case where

$$B = -A,$$
(13)

This physical situation can take place in the case when a nanoparticle nucleus with a size of $\rho_0 < 1$ (for definiteness, $\rho_0 = 0.1$) has already been formed; however, the development of it to an equilibrium state with $\rho = 1$ is hindered by the created (artificially) anisotropy:

$$\frac{-A\sin^2\theta_a}{\rho^2}.$$
(14)

We believe that this anisotropy manifests itself only starting from some sizes corresponding to the value

$$\rho_0 = 0.1$$
(15)

Then, for this case, the equation is greatly simplified:

$$\theta''(\rho) + \frac{\theta'(\rho)}{\rho} = 0.$$
(16)

A particular solution for equation (16) can have the form (in our case, we use condition (16) to compare it with the solution in the form of formula (9)):

$$\pi - \theta = c\ln(\rho/\rho_0),$$
(17)

where

$$c = \pi / (2\ln(1/\rho_0)), \quad \text{(for } \rho > \rho_0.\text{)}.$$

Function graph $c\ln(\rho/\rho_0)$ is shown in Fig. 4.
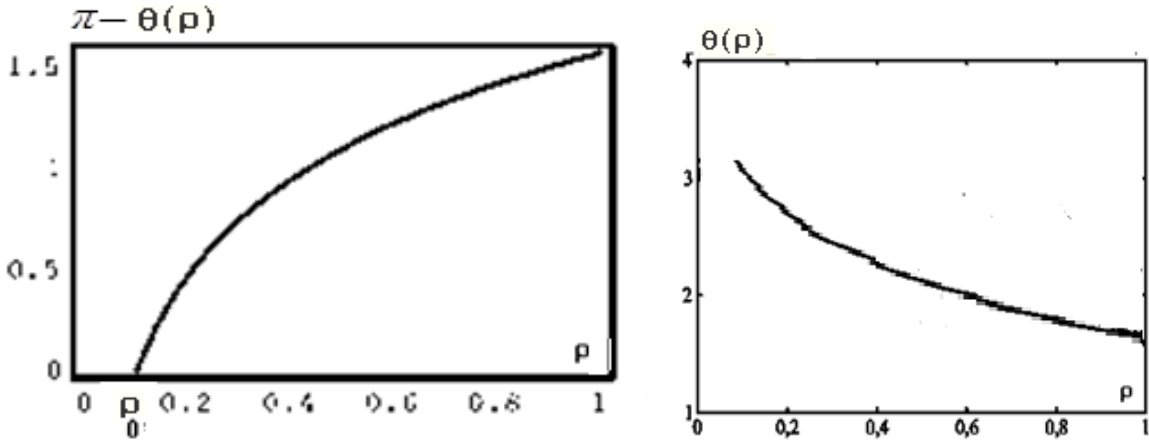
Fig. 4. Functions graphs of solution (17).

3. Electrochemical Application
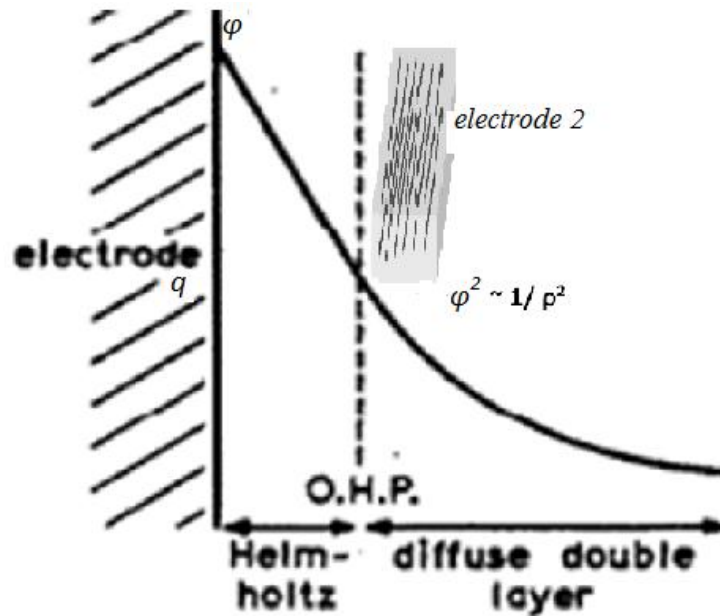
Fig. 5. Scheme of the physical process of nucleation for the case of electrochemical nucleation. The charge is q, the potential is φ. The capacity of the double layer is C. Electrode *2* (grid) can control the electrodeposition by changing the potential and electrical capacity of the near-electrode layer.

We can study the electrochemical nature of the examined anisotropy for the case of

electrochemical nucleation. This anisotropy can be generated using the distribution of the electric field in the near-electrode layer, because the dimensions of the particles become comparable to the dimensions of the layer.

Let the surface energy change $d\sigma$ in the nucleation process according to the Lippman equation [25]:

$$-d\sigma = qd\varphi, \qquad (18)$$

where q and φ are the charge and potential on the surface. In the approximation of the constant capacity of the double layer C

$$q = C\varphi. \qquad (19)$$

Note that constant capacity C is defined as a specific amount, namely, capacitance per unit area as surface energy σ is defined as the amount of energy per unit area.

For the change in surface energy σ, we obtain

$$\sigma = C(\varphi)^2/2. \qquad (20)$$

The change in the surface energy can be attributed to the anisotropy introduced above. Actually, if we assume that an asymptotic functional dependence occurs,

$$(\varphi)^2 \sim 1/\rho^2, \qquad (21)$$

then we finally obtain for parameter a^2

$$a^2/r_c \sim C/2, \qquad (22)$$

where $r_c \sim 10^{-6}\,\text{cm}$ is the equilibrium value of the nanoparticle dimension.

For the evaluation, we take the specific capacity of a mercury electrode that is known to be on the order of

$$C/2 \sim 10^7 \ (1/\text{cm}) \ \ (\text{CGS}). \qquad (23)$$

If we confine ourselves to the upper limit of the r_c value, then, for the evaluation of dimensionless quantity a^2, we obtain

$$a^2 \sim 10. \qquad (24)$$

In general, the consideration results are qualitative.

4. Mathematical Application

In terms of the classical theory [8–10, 22–24], we can obtain (see Fig. 6)

$$\tan\left(\frac{\theta}{2}\right) \sim \frac{H}{R}$$

. $\qquad$ (25)
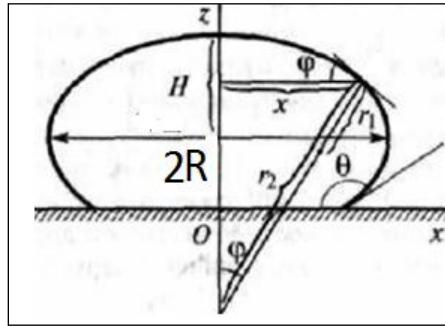
Fig. 6. Dimensionless profiles of a sessile microdrop.

From formulas (5)–(9), we can obtain the dependence

$$\tan\left(\frac{\theta}{2}\right) = \frac{1}{\rho} \qquad \text{and}$$

$$\tan\left(\frac{\theta_a}{2}\right) = \frac{1}{\rho^a}.$$

These formulas (18) and (5)–(9) have the same analytic structures.

In terms of the Cahn–Hilliard theory, we obtain same analytic structures (12). Another dependence, which can correspond to (5)–(9), is obtained in [26].

5. Conclusions

(i) We have obtained results associated with the van der Waals gradient theory, which can be resumed in the following way. If in the formation of a nanoparticle there is only one energy form that plays the role of exchange interaction *A*, then, in the context of the proposed model, the additive separation of the system energy into the surface energy and the nanoparticle volume energy is incorrect. However, in this case, we can introduce the average energy of the whole nanoparticle and, from simple geometric considerations, derive the Rusanov linear formula for the surface energy (see [22]). Typically, the Rusanov formula is assumed universally applicable. This fact is not confirmed when our model of the anisotropy energy is complicated.

(ii) The concept of anisotropy energy, which is introduced into the theory in the form of the proposed model as a modified Rapini potential, leads to the appearance of surface energy. Note that, in the conventional Rapini potential, there is no multiplier of the form of $1/r^2$ [21, 22]. Anisotropy energy can have the meaning of double electric layer energy (in electrochemistry); in addition, in the case of the formation of extremely small equilibrium particles with a differentiated surface energy, the electric capacity of the nanosystem where this nanoparticle is

formed should be increased. Thus, it can be assumed that the nano-nucleation process can be efficiently controlled.

References

[1] S. Ono and S. Kondo, Molecular Theory of Surface Tension in Liquids, in Structure of Liquids, series Encyclopedia of Physics, Springer, Berlin, Heidelberg, 1960, vol. 3/10, pp. 134–280.

[2] J. S. Rowlinson and B. Widom, Molecular Theory of Capillarity, Oxford University Press, Oxford, 1989.

[3] M. J. Jaycock and G. D. Parfitt, Chemistry of Interfaces, Halstead Press, John Wiley & Sons, New York, 1981.

[4] A. W. Adamson and A. P. Gast, Physical Chemistry of Surfaces, Wiley-Interscience Publication, John Wiley & Sons, 1997.

[5] A. I. Rusanov and V. A. Prokhorov, Interfacial Tensiometry, Elsevier, Amsterdam, 1996.

[6] R. C. J. Tolman, Chem. Phys. 17 (3), 333 (1949).

[7] S. Sh. Rekhviashvili and E. V. Kishtikova, Tech. Phys. 56 (1), 143 (2011).

[8] S. Sh. Rekhviashvili, Colloid J. 82(3), 342 (2020)

[9] A. A. Sokurov, Vestnik KRAUNC, Ser. Fiz.-Mat. Nauk 23 (3), 140 (2018).

[10] S. Sh. Rekhviashvili and A. A. Sokurov, Turk. J. Phys. 42, 699 (2018).

[11] T. V. Bykov and X. C. Zeng, J. Chem. Phys. 111 (23), 10602 (1999).

[12] T. V. Bykov and X. C. Zeng, J. Chem. Phys. 105 (47), 11586 (2001).

[13] I. A. Hadjiagapiou, J. Phys.: Condens. Matter 7, 547 (1995).

[14] V. I. Kalikmanov, J. Chem. Phys. 121, 8916 (2004).

[15] J. W. P. Schmelzer, G. Ropke, and V. B. Priezzhev, Nucleation Theory and Applications, JINR Publishing House, Dubna, 1999.

[16] J. W. P. Schmelzer, V. G. Baidakov, and G. Sh. Boltachev, J. Chem. Phys. 119, 6166 (2003).

[17] V. G. Baidakov and G. Sh. Boltachev, Phys. Rev. E 59 (1), 5648 (1997).

[18] V. G. Baidakov and G. Sh. Boltachev, Phys. Rev. E 59, 469 (1999).

[19] V. G. Baidakov, S. P. Protsenko, G. G. Chernykh, and G. Sh. Boltachev, Phys. Rev. E. 65, 047601 (2002).

[20] P. E. L'vov and V. V. Svetukhin, Phys. Stat. Sol. 57 (6), 1213 (2015).

[21] S. A. Baranov, in Handbook of Nanoelectrochemistry: Electrochemical Synthesis Methods, Properties and Characterization Techniques, Springer, International Publishing, Switzerland, 2015, pp. 1057–1069.

[22] S. A. Baranov, S. Sh. Rekhviashvili, and A. A. Sokurov, Surf. Eng. Appl. Electrochem. 55 (3), 286 (2019).

[23] S. A. Baranov, Surf. Eng. Appl. Electrochem., 53 (2), 124 (2017).

[24] S. A. Baranov, Mold. J. Phys. Sci. 19 (1–2), 182 (2020).

[25] P. Delahay, J. Chem. Educ. 43, 1, 54 (1966).

[26] A. Milchev and K. Binder, J. Chem. Phys. 117, 6852 (2018).

GLASS-COATED MICROWIRES FOR COMPOSITES

Serghei A. Baranov[1, 2]

[1]*Institute of Applied Physics, str. Academiei 5, Chisinau, MD-2028 Republic of Moldova*
[2]*Shevchenko Pridnestrov'e State University, str. 25 Oktyabrya 128, Tiraspol, Republic of Moldova*
E-mail: baranov@phys.asm.md

(Received March 29, 2021)

Abstract

In this paper, solutions for two problems are proposed. One of the problems is associated with increasing the strength of objects, for instance, the strength of windows in industrial buildings and dwelling houses. The other problem is related to electromagnetic shielding. Both of these problems are related to the protection form terrorist acts, since terrorists make use of concentrated electromagnetic pulses to destroy computers or other electronic equipment. The proposed solutions are based upon the manufacturing of glass windows reinforced with cast glass-coated amorphous micro- and nanowires (CGCAMNWs) having a special composition and structure, which increases their tensile strength against mechanical destruction, on the one hand, and imparts them with shielding properties against electromagnetic radiation, on the other hand. The CGCAMNW materials are of interest from both theoretical and practical points of view.

Keywords: glass-coated amorphous micro- and nanowires, Taylor–Ulitovsky method

Rezumat

În această lucrare sunt propuse soluții pentru două probleme. Una este asociată cu ridicarea durabilității obiectelor, de exemplu a durabilității ferestrelor în clădiri industriale și case de locuit. A doua problemă este legată de ecranarea electromagnetică. Ambele probleme au legătură cu protejarea contra actelor de terorism, deoarece teroriștii utilizează impulsurile concentrate de radiație electromagnetică pentru distrugerea calculatoarelor și altor echipamente electronice. Soluțiile propuse se bazează pe confecționarea ferestrelor din sticlă întărite cu micro- și nano-fire amorfe turnate în înveliș de sticlă (MNFATAS) cu compoziții și structuri specifice, care ridică durabilitatea lor mecanică, pe de o parte, și le conferă proprietăți de ecranare contra radiației electromagnetice, pe de altă parte. MNFATAS prezintă interes atât din punct de vedere teoretic, cât și din punct de vedere al aplicațiilor practice.

Cuvinte cheie: micro- și nanofire amorfe, înveliș de sticlă, metoda Taylor–Ulitovsky

1. Introduction

One of the dangerous consequences of acts of terrorism is a traumatism of people owing to shattering of window glass of administration, industrial, and apartment houses. Therefore, an urgent problem is to improve the glass strength by decreasing the probability of forming and spreading the splinters during shattering.

In addition, modern acts of terrorism can occur with use of concentrated beams of radio-frequency pulses in order to disable computers and other electronic devices, running of life-support systems of cities, etc.

Furthermore, the radio-electronic intelligence service using directional electromagnetic radiation for reading information typed on the computer keyboard or displayed in the monitor, for example, via window opening, is concerned with modern acts of terrorism and espionage activity.

It is known that conventional glass almost completely passes electromagnetic radiation in the entire frequency range. Therefore, the problem of producing radio-screening glasses is also urgent.

The above problems can be solved in complex with the use of glass reinforced with glass-coated microwires prepared by the solution casting technique of the Taylor–Ulitovsky method [1–4].

The reinforcement of glass with glass-coated microwires using an adhesive film increases the durability of the glass under shock and static loadings and prevents splinter scattering in the case of glass shattering.

In addition, this glass considerably reduces the transitivity of electromagnetic radiation in a wide frequency range—from a few hundreds of megahertz to a few tens of gigahertz.

The reinforcement of glass with microwires does not reduce the light transmission ability in the entire gamut of colors, as in conventional glass, and does not worsen the transparency of the glass. Glass-coated microwires are almost imperceptible.

Another possible application of microwires in the antiterrorist purposes, also for providing a hardening and screening effect, is the reinforcement of vests and helmets made of plastic, such as Kevlar, with microwire elements.

The microwire represents a construction composed of a continuous metal core coated with a continuous glass coating.

For a more precise comparison of the theory with the experiment, a set of experimental measurements is required; they are also discussed in the paper.

The resulting microwires with an optimum chemical composition were tested for reinforcing window glass. A grid of high-strength microwires was preconstructed using linear and orthogonal winding. After that, a melt was poured into special molds to reinforce window glass to obtain a sheet blank with a thickness of about 1–3 mm.

.

2. Casting of Glass-Coated Amorphous Magnetic Microwires

Cast glass-coated amorphous micro- and nanowires (CGCAMNWs) are prepared using a rapid solidification technique, the so-called quenching and drawing procedure, or a modified Taylor–Ulitovsky method [1–4], as shown in Fig. 1.
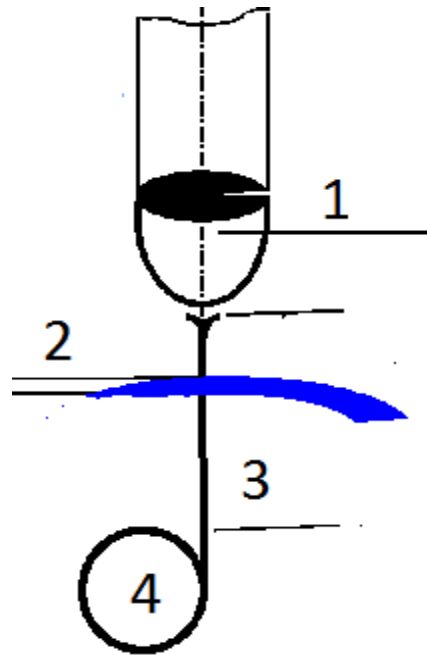
Fig. 1. Casting of CGCAMNWs (see [1–4] and below):
(*1*) glass tube with a metal droplet, (*2*) water, (*3*) glass-coated microwire, and
(*4*) rotating receiving bobbin.

In this process, an alloy in an amount of a few grams is placed inside a glass tube held directly over suitable heating means, for example, a high-frequency inductor heater. The alloy is heated up to the melting point to form a droplet. The portion of the glass tube adjacent to the melting metal softens to envelope the metal droplet. A glass filament is drawn from the softened glass portion and collected onto a receiving bobbin. Under certain drawing conditions, the molten metal can fill the glass capillary; thus, a microwire in which a metal core is covered continuously with glass is formed. The glass consumption in the process is compensated by continuous delivery of the glass tube in the inductor zone, whereas the formation of the metallic core is restricted to the initial amount of the droplet. The microstructure and, accordingly, properties of a microwire considerably depend on the cooling rate, which can be controlled by a cooling mechanism when the metal-filled capillary passes through a stream of a cooling liquid (water or oil) on its way to the receiving coil.

The main advantages of this method for the production of cast glass-coated microwires are as follows [1–4]:

(i) The formation of continuous long pieces of a microwire up to 10^4 m (in the case of a drip process). For a continuous process (see Fig. 1), the microwire length is not limited.

(ii) A wide range of variations in the geometric parameters (typically the metallic core diameter D_m is in a range of 0.5–70 μm, and the glass-coating thickness is in a range of 1–50 μm).

(iii) The control and adjustment of the geometric parameters (inner metallic core diameter D_m and glass thickness) during production.

(iv) The reproducibility of the physical properties and geometric parameters of the microwires in large-scale production.

3. Production of Glass Reinforced with Microwires

Glass reinforced with a microwire represents a three-layered construction consisting of two pieces of glass glued using a special adhesive film.

The adhesive film consists of an adhesive base on two sides of which pieces of a microwire are put in mutual perpendicular directions.

In the case of an electromagnetic wave incident on the interface between two media, a portion of the field is reflected from the surface; another portion permeates and spreads inside the other medium; the third portion interacts with the medium and is absorbed (transformed into heat). The coefficient of screening of the medium $/G_{\text{eff}}/$ can be written as follows:

$$/G_{\text{eff}}/ = P_{\text{r}}/P_{\text{s}}, \tag{1}$$

where P_{r} is the power of the incident wave and P_{s} is the power of the past wave.

Since an electromagnetic wave contains electrical and magnetic components, the interaction of an electromagnetic wave and a medium can be electrical in the case of a conducting medium and magnetic in the case of a screen with a high magnetic permeability.

(i) For screening household and working buildings, inside which electromagnetic radiation is not located, for constructions and devices requiring protection against external electromagnetic radiation, it is reasonable to apply reflecting screens containing a microwire made of conducted materials (copper, silver, and alloys based on them). Depending on the screened object, the screens can be pliable and elastic, such as fabrics containing a microwire, and rigid, such as plastics, polymers, and glass or paper products.

(ii) For screening household and working buildings, in which, in addition to protection from external radiation, it is required to inhibit (weaken) electromagnetic radiation and reradiation from an internal source of radiation, it is reasonable to apply microwire-reinforced reflecting–absorbing screens having a high impedance at the working frequencies of the source. For example, in buildings with a powerful source operating at an extremely high radiation frequency, it is reasonable to apply microwire-reinforced materials having a resonant absorption frequency of the working source.

(iii) It is reasonable to use reflecting–absorbing multilayered electromagnetic shields for screening people (service personnel) working under conditions of high-level electromagnetic radiation.

(iv) Description of the design and technology of production of shielding. To provide functionality in electromagnetic screens, a microwire should be located as a grid construction. In this case, the microwire is located in a plane of the screen in two mutually perpendicular directions. The grid construction steps and the types and number of microwires in a construction are determined from requirements for the level of loosening the radiation power, the frequency range of screening, and expediency of applying the shielding.

In implementing the stage of working out the technology for the preparation of triplex glass reinforced with microwires, technological equipment and process modes for gluing the glasses will be developed.

4. Absorption Properties

The design of GCAMNW composites was described in [8–11]. We have following typical configurations:
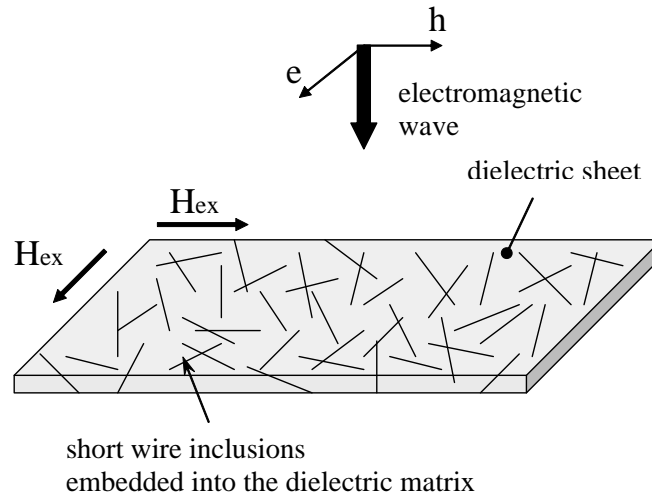

Fig. 2. Composite shielding for radio absorption protection with GCAMNWs made with a stochastic mixture of microwires in the polymeric matrix.
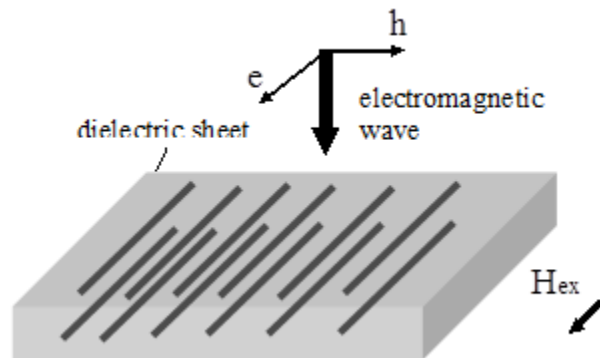

Fig. 3. Composite shielding for radio absorption protection with GCAMNWs in the form of a grating.

Natural ferromagnetic resonance (NFMR) occurs if the sample is subjected to a microwave field without application of any biasing field other than the anisotropy field of the microwire [8–13].

Permeability dispersion is as follows:

$$\mu(\omega) = \mu'(\omega) + i\,\mu''(\omega). \tag{2}$$

The peak in μ" (and a zero crossing of μ'):
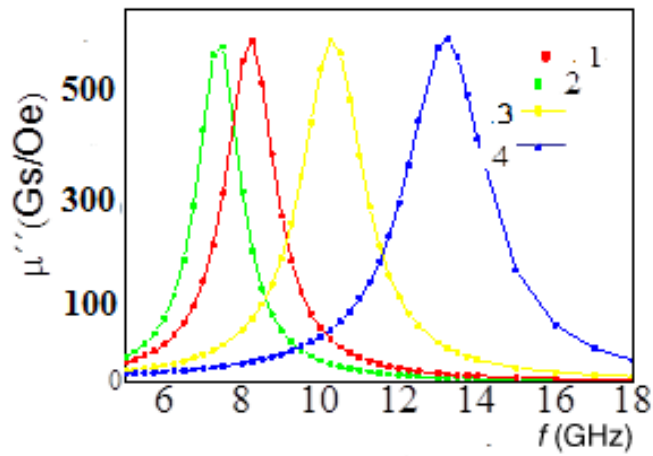
Fig. 4. Imaginary relative permeability of components around NFMR for (*1*) $Co_{70}Fe_{5,5}B_{14,5}Si_{10}$, (*2*) $Co_{70}Mn_7B_{13}Si_{10}$, (*3*) $Co_{59}Fe_{15}B_{16}Si_{10}$, and (*4*) $Fe_{69}C_5B_{16}Si_{10}$ microwires.

.
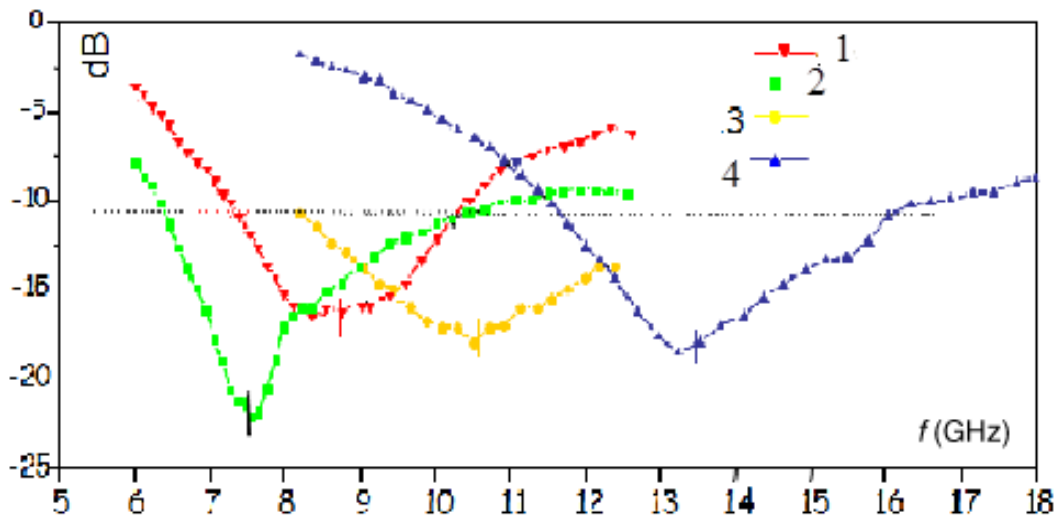
Fig. 5. Typical absorption characteristics of shielding by composite in an HF field of components around NFMR for (*1*) $Co_{70}Fe_{5,5}B_{14,5}Si_{10}$, (*2*) $Co_{70}Mn_8B_{12}Si_{10}$, (*3*) $Co_{59}Fe_{15}B_{16}Si_{10}$, and (*4*) $Fe_{69}C_5B_{16}Si_{10}$ microwires (see [5–11]).
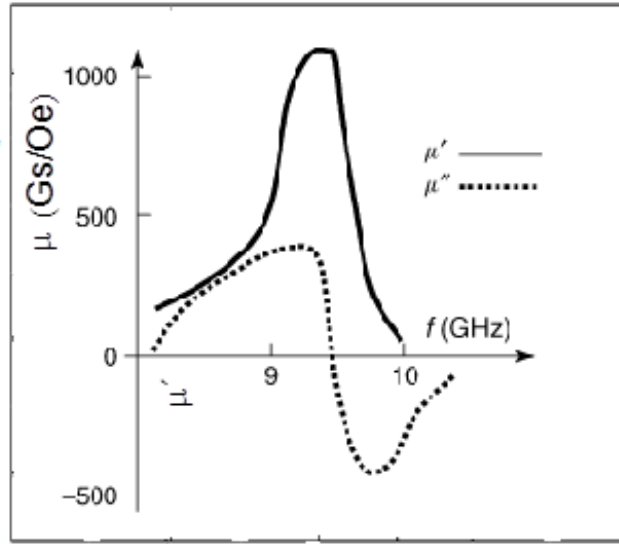
Fig. 6. Frequency dispersion of the real and imaginary parts of relative permeability around the NFMR frequency for the $Fe_{68}C_4B_{16}Si_{10}Mn_2$ microwire (see [1, 2, 5–13]).

Figures 4–6 show resonance frequencies of 7.5, 8.5, 10.5, and 13.5 GHz and resonance widths of 1.5, 2, 3, and 4 GHz.

Near μ'' resonance is expected to be described as follows:

$$\mu'' / \mu_{dc} \sim \Gamma \Omega / [(\Omega - \omega)^2 + \Gamma^2], \qquad (3)$$

where μ_{dc} is the static magnetic permeability and Γ is the width of the resonant curve. Very near resonance, where $\Gamma > (\Omega - \omega)$, Eq. (3) reduces to

$$\mu'' / \mu_{dc} \sim \Omega / \Gamma \sim (10 \div 10^2). \qquad (4)$$

Monitoring the geometry of the microwire (i.e., wire diameter) and the magnetostriction through the microwire composition makes it possible to prepare microwires with desirable permeability dispersion and for absorption materials: (i) determining the resonant frequency in a range of 1–12 GHz and (ii) controlling the maximum of the imaginary part of magnetic permeability.
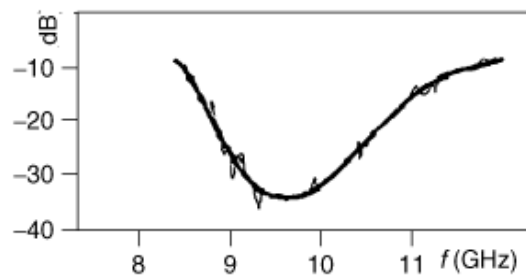
Fig. 7. Typical absorption characteristics of shielding by a microwire composite with NFMR in an HF field in a frequency range of 10 GHz.

Figure 7 also shows the frequency absorption spectrum of shielding with $Fe_{69}C_5B_{16}Si_{10}$ microwires. The varying attenuation is attributed to the lack of an ideal angular distribution of microwires, the length of which does not always fit into the shielding thickness.

Pieces of microwires were embedded in planar polymeric matrices to form a composite shielding for radio absorption protection. Experiments were performed employing a commercial polymeric rubber with a thickness of about 2–3 mm. Microwires were spatially randomly distributed over the matrix before its solidification. The concentration was maintained below 8–10 g of microwire dipoles (1–3 mm long) per 100 g of rubber [1, 5–7]. A typical result obtained in an anechoic chamber is shown in Fig. 6 for shielding with embedded $Fe_{69}C_5B_{16}Si_{10}$ microwires.

It is evident that an absorption level of at least 10 dB is obtained in a frequency range of 8–12 GHz with a maximum attenuation peak of 30 dB at about 10 GHz. In general, optimum absorption is obtained using microwires with metallic nuclei with a diameter of $2r = 1$–3 μm ($2R \sim 20$ μm ($x > 10$)) and a length of $L = 1$–3 mm. These pieces of microwires can be treated as dipoles whose length L is comparable to the half value of effective wavelengths $\Lambda_{eff}/2$ of the absorbed field in the composite material (i.e., in connection to a geometric resonance).
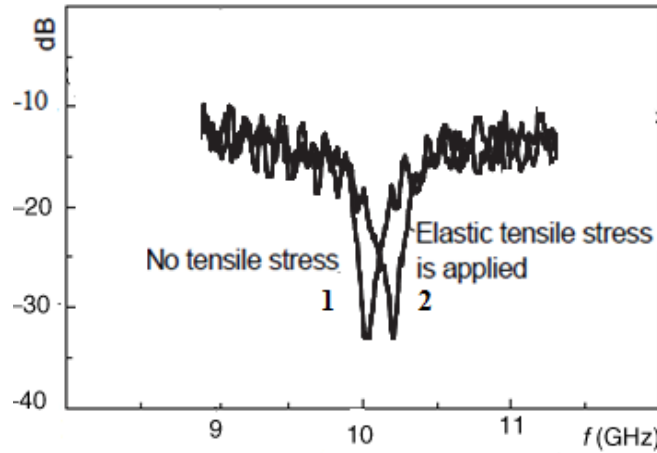
Fig. 8. (*1*) Average absorption characteristics of a shielding containing a microwire composite exhibiting NFMR in a microwave frequency range of 10–10.2 GHz for $Fe_{68}C_4B_{16}Si_{10}Mn_2$ microwires ([2, 5–12]) and (*2*) absorption curve in the case of an external pressure (see [5–12]).

5. Theory for Absorption Materials

The propagation of an electromagnetic wave through absorption shielding with microwire-based elements is characterized by transmittance $/T/$ and reflectance $/R_r/$ (coefficients given in [2, 5–13]):

$$|T| = (\alpha^2 + \beta^2)/[(1+\alpha)^2 + \beta^2]; \quad |R_r| = 1/[(1+\alpha)^2 + \beta^2], \tag{5}$$

where $\alpha = 2X_r/Z_0$ and $\beta = 2Y/Z_0$, with $Z_0 = 120\,\pi/Q$, and the complex impedance $Z = X_r + iY$.

Absorption function G is correlated with the generalized high-frequency complex conductivity Σ (or high-frequency impedance Z).

Here, we use the analogy between the case of a conductor in a waveguide and that of a diffraction grating. The absorption function given by

$$|G| = 1 - |T|^2 - |R_r|^2 = 2\alpha / [(1+\alpha)^2 + \beta^2] \tag{6}$$

has a maximum

$$|G_m| = 0.5 \geq |G|,$$

for simultaneous $\alpha = 1$ and $\beta = 0$, for which

$$|T|^2 = |R_r|^2 = 0.25.$$

The minimum $|G| = 0$ occurs at $\alpha = 0$ and β of any positive number.

Theoretical estimations taking into account only the active résistance of microwires result in attenuation in a range of 5–10 dB, which is much lower than experimental results, which for a spacing of microwires of $Q = 10^{-2}$ m ranges between 18 and 15 dB, while for a spacing of $Q = 10^{-3}$ m it increases up to 20–40 dB. Thus, it becomes clear that shielding exhibits anomalously high absorption factors, which cannot be attributed solely to the resistive properties of microwires.

Let us consider the effective absorption function [2, 5–13]:

$$/G_{eff}/ \sim \Gamma_{eff} \Omega_{eff} / [(\Omega_{eff} - \Omega)^2 + \Gamma_{eff}^2], \tag{7}$$

where $\Gamma_{eff} \geq \Gamma$ and $\Omega \sim \Omega_{eff} = 2\pi c/\Lambda$.

A microwave antenna will resonate when its length L satisfies to the condition

$$L \sim \Lambda / 2(\mu_{eff})^{\frac{1}{2}} . \tag{8}$$

Absorptions maximum (see Fig. 7) occurs for $\Omega_{eff} \sim 10$ GHz ($\Lambda \sim 3$ cm) and $\mu_{eff} \sim 10^2$ [2, 5–13].

This corresponds to

$$L \sim 1.5\text{–}2 \text{ mm}, \tag{9}$$

where the microwire concentration is much less than the percolation threshold. A higher concentration of dipoles leads to an increase in absorption $/G_{eff}/$ and an increase in reflectance $|R_{r1}|$, which can be simply estimated as [2, 5–13]:

$$|R_{r1}| \sim 1 - 2\sqrt{(\Omega/2\pi \Sigma_m)} , \tag{10}$$

where $\Omega/2\pi \sim 10^{10}$ Hz.

The formula is applicable, and calculation of small reflectance $/R_{r1}/$ is possible, only if

$$\Sigma_m \sim 10^{11} \text{Hz} \tag{11}$$

for concentration below the percolation threshold (as $\Sigma_2 \sim 10^{15}$ Hz).

6. Conclusions

Microwave electromagnetic response has been analyzed for composites consisting of dipoles and a diffraction grating of amorphous magnetic glass-coated microwires in a dielectric. These materials can be employed for radio absorbing screening. The spontaneous NFMR phenomena observed in glass-coated microwires has opened the possibility of developing novel broad-band radio absorbing materials.

The described studies provide the following basic conclusions [8]:

(a) Cast GCAMNWs exhibit NFMR whose frequency depends on the composition, geometrical parameters, and deformation of the microwire. The NFMR phenomenon observed in

glass-coated magnetic microwires opens up the possibility of developing new radio-absorbing materials with a wide range of properties. An important feature of cast microwires with an amorphous magnetic core is the dependence of the NFMR frequency on the deformation (stress effect). The calculations have shown that the shift of the NFMR frequency caused by the stress effect achieves 20% before the degradation of the composite.

(b) The general technology of magnetic wire composites is cost-effective and suitable for large-scale applications.

Here, the electromagnetic properties of composites with magnetic wires showing NFMR phenomena have been discussed. A striking property of these materials is that the spectra of the effective electromagnetic parameters (permittivity and permeability) can be actively tuned.

The technology of glass coated amorphous microwires provides the preparation of continuous wires.

References

[1] S. A. Baranov, V. S. Larin, and A. V. Torcunov, Crystals 7, 136 (2017).

[2] S. A. Baranov, An Engineering Review about Microwire, Lambert (Academic publishing), 2017.

[3] H.-X. Peng, F. Qin, and M.-H. Phan, Ferromagnetic Microwire Composites: From Sensors to Microwave Applications, Springer, Switzerland, 2016.

[4] F. Qin and H.-X. Peng, Progr. Mater. Sci. 58 (2) (2013).

[5] S. A. Baranov, M. Yamaguchi, K. L. Garcia, and M. Vazquez, Surf. Engin. Appl. Electrochem. 44(6), 245 (2008).

[6] S. A. Baranov, Tech. Phys. Lett. 24, 549 (1998).

[7] S. A. Baranov, Mold. J. Phys. Sci. 14 (3–4), 201 (2015).

[8] E. Adar, A. M. Yosher, and S. A. Baranov, J. Phys. Res. Appl. 3, 118 (2020).

[9] E. Adar, S. A. Baranov, N. A. Sobolev, and A. M. Yosher, Mold. J. Phys. Sci. 19 (1–2), 89 (2020).

[10] S. A. Baranov, Biomed J. Sci. Tech. Res. 32 (5), 25413 (2021)

[11] S. A. Baranov, Global J. Sci. Front. Res., A 20 (14) (2021).

[12] M. J. Malliavin, O. Acher, C. Boscher, F. Bertin, and V. S. Larin, J. Magn. Magn. Mat.. 196–197, 420 (1999)

[13] A.N. Antonenko, S.A. Baranov, V.S. Larin, and A.V. Torkunov, J. Mat. Sc. and Eng. A 248, 248 (1997)

FABRICATION OF *p*-NiO/*n*-ZnO:Ga HETEROSTRUCTURES FOR A RECTIFIER DIODE AND A UV PHOTODETECTOR VIA RF MAGNETRON SPUTTERING AND SPRAY PYROLYSIS SYNTHESIS

Lidia Ghimpu[1], Victor Suman[1], Dumitru Rusnac[2], and Tamara Potlog[2]

[1]*D. Ghitu Institute of Electronic Engineering and Nanotechnologies, Academiei str.3/3, Chisinau, MD-2028 Republic of Moldova*
[2]*Moldova State University, A. Mateevici str. 60, Chisinau, Republic of Moldova*
E-mail: lidia.ghimpu@gmail.com

Abstract

In this paper, a *p–n* thin film NiO/ZnO heterojunction for a rectifier diode and a UV photodetector is prepared and characterized. Nickel oxide (NiO) and gallium-doped zinc oxide (ZnO:Ga) thin films are grown by RF magnetron sputtering and spray pyrolysis techniques, respectively. The crystal structure of the thin films is studied by the X-ray diffraction (XRD) method. The transmittance and reflectance are studied by UV–VIS spectroscopy. The *p–n* electrical parameters are estimated from current–voltage characteristics. The effects of duration of thermal annealing at 450°C on the characteristics of the NiO/ZnO:Ga device are evaluated. The non-annealed diode shows the best rectification coefficient of 10^5 at ± 1 V. The *p–n* photodetection capability is studied under UV illumination. At a reverse bias of –3 V under 365-nm UV illumination, the device shows a current intensity of $\sim 6.2 \times 10^{-12}$ A. The observed increase in the reverse current intensity by about two orders of magnitude under a UV lamp with a spectral irradiance of 10 W m^{-2} μm^{-1} indicates a promising application in UV light detection.

Keywords: RF magnetron sputtering, spray pyrolysis, UV–VIS spectroscopy, electrical properties.

Rezumat

În această lucrare, a fost descrisă fabricarea și caracterizarea diodei redresoare și senzorului UV pe baza heterojoncțiunii cu straturi subțiri *p*-NiO/*n*-ZnO. Straturile subțiri de oxid de nichel (NiO) și oxid de zinc (ZnO:Ga) au fost obținute prin metoda pulverizării în regim de radiofrecvență (RF) și, respectiv, metoda pulverizării pirolitice. Structura cristalină a straturilor subțiri a fost investigată prin metoda difracției cu raze X (XRD). Transmitanța și reflectanța au fost studiate prin spectroscopie UV-VIS. Parametrii electrici ai heterojoncțiunii *p-n* au fost estimați din caracteristicile curent-tensiune. Au fost evaluate efectele duratei tratării termice la 450°C asupra caracteristicilor structurii NiO/ZnO:Ga. Dioda redresoare netratată a arătat cel mai bun coeficient de redresare de 10^5 la aplicarea tensiunii ± 1 V. Capacitatea de detecție a senzorului pe baza heterojoncțiunii *p-n* a fost studiată la iluminarea UV. Curentul de întuneric al joncțiunii la polarizare inversă de -3V este $\sim 6,2 \times 10^{-12}$ A. O creștere a curentului invers cu

aproximativ două ordine de mărime la iluminare cu lampa UV cu iradiere spectrală 10 Wm^{-2}µm^{-1} prezintă o aplicație promițătoare în detectarea luminii UV.

Cuvinte cheie: pulverizare cu magnetron RF, piroliză prin pulverizare, spectroscopie UV–VIS, proprietăți electrice

1. Introduction

Metal oxide thin films have attracted much interest because of their electrical and optoelectronic characteristics and various applications. Zinc oxide and NiO have attracted attention as promising candidates for heterojunction thin film devices. The most important native defects that affect ZnO are attributed to the presence of interstitial zinc and oxygen and oxygen and zinc vacancies, which are intrinsic defects [1]. Niobium oxide is inherently of the *p*-type because of the presence of native acceptor defects generated by nickel vacancies. Both materials have good band alignment [2, 3]. Zinc oxide and NiO have been extensively studied for use in electronic and optoelectronic devices, such as light emitting diodes, sensors, photodetectors, and thin film *p–n* junctions [2–4]. The *p–n* type photodetector has many advantages, in particular, low bias current, high impedance, capability for high frequency operation, and compatibility of the fabrication technology with planar-processing techniques [5]. Up to now, a variety of *n*-type metal oxide thin films has been studied for *p–n* junction diode or ultraviolet (UV) photodetector applications. Among them, amorphous indium gallium zinc oxide (a-IGZO) has been widely studied because of its high mobility, good uniformity, low temperature process, and high optical transparency [6]. The amorphous nature of the IGZO thin film makes it a good choice for multi-layer devices due to the smooth interface, which is quite helpful to device performance [7]. Similar to *n*-type materials, *p*-type metal transparent oxides do not exist widely in nature. Among the available *p*-type metal oxide thin films, nickel oxide has been given considerable attention due to its *p*-type conductivity and transparency [8–11]. A UV detector based on lithium-doped NiO and ZnO was reported by Ohta et al. [12]. The literature survey reveals that there is no detailed report on analysis of the *p–n* junction parameter for gallium-doped ZnO and undoped NiO. In this paper, we describe the preparation and characterization of a heterojunction rectifier diode and a UV photodetector based on undoped NiO deposited by RF magnetron sputtering and Ga-doped ZnO grown by the spray pyrolysis technique.

2. Experimental

Nickel oxide deposition was conducted on a RF magnetron sputtering system using a Ni target of 99.5% purity. Nickel oxide was prepared at room temperature by RF magnetron sputtering at 210 W RF power. The distance from the sample to the target was 7–8 cm. The working pressure was maintained at 4×10^{-3} Pa. Different levels of carrier concentrations in the NiO layer can be achieved by introducing different amounts of O_2 gas during the sputtering deposition [13, 14]. With a higher amount of O_2 gas introduced during the sputtering deposition, a larger number of nickel vacancies, which act as acceptors, are formed in *p*-NiO thin films [13]; on the contrary, a smaller number of oxygen vacancies, which act as donors, are formed in *n*-ZnO thin films [14]. Zinc oxide layers doped with Ga were deposited by spray pyrolysis in an argon (Ar) atmosphere. The initial solution was prepared by dissolving zinc acetate [$Zn(CH_3COO)_2 \cdot 2(H_2O)$] in a methanol–water solution in a ratio of 25 : 65 to obtain a concentration of 0.2 M. In addition, to prevent the aggregation process, a few drops of concentrated acetic acid were added to the starting solution. For doping of ZnO thin films,

gallium trichloride ($GaCl_3$) was used. The vacuum thermal annealing of ZnO:Ga thin films deposited on a NiO/glass substrate was performed at 450°C for 90 min. Heterojunctions having the structure of In/*n*-ZnO:Ga /*p*-NiO/Au were prepared in the following sequence. First, a 200-nm-thick NiO film was deposited on a glass substrate by the RF magnetron sputtering method. At 3–4 sccm O_2 (99.99%) in the O_2/Ar+O_2 flow, an RF power of 210 W, and a substrate temperature of 450°C, a carrier concentration on the order of 10^{16}–10^{17} cm^{-3} was achieved in the NiO thin film. After that, a 300-nm-thick ZnO layer doped with 3% Ga was deposited by spray pyrolysis. An Al electrode was evaporated for NiO, whereas Au was used for ZnO:Ga thin films.

The structural properties of NiO, ZnO:Ga, and NiO/ZnO:Ga thin films were studied at room temperature on *a XRD Rigaku* Ultima IV *diffractometer* using Cu$K_α$ radiation ($λ$ = 1.5405 Å) at 40 kV and 30 mA. The optical transmittance values of the thin films were measured in a wavelength range of 300–900 nm using a PerkinElmer double-beam UV–VIS spectrophotometer. The current–voltage (I–V) measurements were conducted using a Keithley 2400 source meter and a Newport Oriel lamp (94023A).

3. Results and Discussion

Figure 1 shows X-ray diffraction pattern of the Ga-doped ZnO thin film thermally annealed in a vacuum and the NiO thin film grown at room temperature. The XRD studies of the ZnO:Ga thin film revealed a polycrystalline nature with the (0002) plane as the dominant orientation and a hexagonal wurtzite crystal structure, as confirmed by the standard JCPDS card number 089-1397. According to the authors of [15, 16], who studied Ga-doped ZnO thin films, the diffraction peak at 31.61^o indicate that Ga can occupy regular positions of the structure, while replacing zinc ions with tetrahedral coordination, or can be incorporated into octahedral interstices. We suppose that the observed diffraction peak corresponds to the $Zn_{1−x}Ga_xO$ phase [17]. The grain size estimated from the (0002) plane reached about 29.0 nm. The XRD results show that the NiO thin film has a polycrystalline structure with the (111) and (200) reflections corresponding to the NiO cubic lattice [18]. The average grain size of the NiO thin film is about 17.0 nm. At room-temperature growth, i.e., in the case of an unheated sample holder, the deposited atoms will have a lower mobility. This factor hinders the diffusion of atoms in an energetically convenient site and forces the atoms to nucleate in new sites of the atom; as a consequence, smaller grains are formed. The XRD pattern of the NiO/ZnO:Ga structure revealed the presence of not only ZnO and NiO phases, but also other phases, such as $NiGa_2O_4$ and NiO_2.
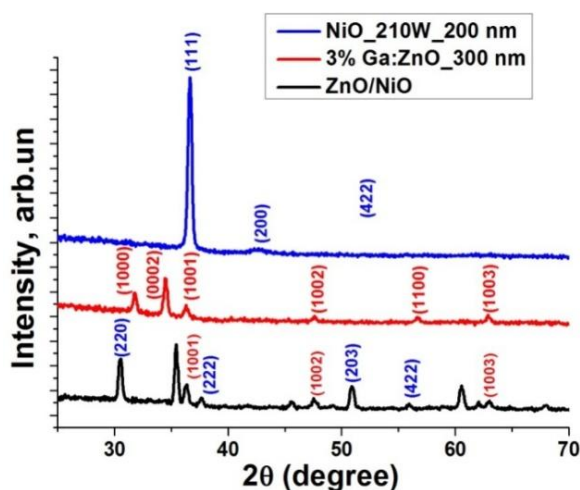

Fig. 1. X-ray diffraction pattern of the sputtered NiO thin film, the ZnO:Ga thin film thermally annealed in a vacuum, and the ZnO/NiO heterostructure.

It is well known that NiO exists in various oxidation states, such as nickel trioxide or sesquioxide (Ni_2O_3), nickelous oxide (NiO), nickel dioxide (NiO_2), nickelosic oxide (Ni_3O_4), and nickel peroxide (NiO_4). The ZnO XRD peaks are much weaker than those of NiO; this fact indicates that the ZnO thickness is ultrathin.

Table 1. Structural parameters of the sputtered NiO thin film, the ZnO:Ga thin film thermally annealed in a vacuum, and the ZnO/NiO heterostructure

| Samples	No.	2θ	d, Å	FWHM, rad	D, Å	ε	hkl
NiO	1	36.64	2.4518	0.0068	236.70	0.00518	111
	2	42.60	2.1212	0.0246	67.22	0.01578	200
ZnO	1	31.79	2.8139	0.0065	242.91	0.00579	1000
	2	34.49	2.5996	0.0063	256.14	0.00507	0002
	3	36.30	2.4740	0.0075	214.62	0.00576	1001
	4	47.60	1.9097	0.0077	216.88	0.0044	1002
	5	56.69	1.6231	0.0085	204.05	0.00398	1100
	6	62.92	1.4766	0.0078	230.03	0.00321	1003
ZnO/NiO	1	30.51	2.9290	0.0067	236.52	0.00619	$NiGa_2O_4$ 220 (cubic)
	2	35.44	2.5320	0.0059	274.28	0.00462	unknown
	3	36.32	2.4727	0.0072	222.87	0.00555	ZnO 101
	4	37.65	2.3883	0.0063	255.61	0.00467	$NiGa_2O_4$ 222 (cubic)
	5	41.74	2.1633	0.0084	195.26	0.00554	unknown
	6	45.60	1.9887	0.0074	225.39	0.00441	unknown
	7	47.59	1.9101	0.0089	188.86	0.00506	ZnO 102
	8	50.91	1.7930	0.0073	231.20	0.00388	NiO_2 203
	9	55.94	1.6431	0.0076	227.23	0.00362	$NiAl_2O_4$ 422 (cubic)
	10	60.56	1.5283	0.0078	227.22	0.00336	unknown
	11	62.07	1.4947	0.0069	258.27	0.00289	unknown
	12	62.97	1.4755	0.0088	204.22	0.00361	ZnO 103
	13	67.95	1.3790	0.0076	241.43	0.00286	ZnO 112

The optical transmittance $T(\lambda)$ and reflectance $R(\lambda)$ spectra of the NiO, ZnO:Ga, and NiO/ZnO:Ga thin films in a wavelength range of 350–800 nm are shown in Fig. 2. These spectra show that the ZnO:Ga films exhibit a reflectance exceeding 20% in the visible range and a

transparency between 40–50% in the visible region. This low transparency can be attributed to the surface defects, such as voids and pores. The NiO thin film has a moderate transmittance in the short wavelength range of the UV–Vis region, which gradually increases in the NIR region. The transmittance of the NiO thin film in the visible region is between 30–40%. The transmittance of the NiO/ZnO:Ga structure is about 40% in the UV-VIS region; it gradually decreases in the NIR region. From the transmittance and reflectance spectra of ZnO:Ga, NiO, and NiO/ZnO shown in Fig. 2, the optical band gap was estimated by plotting the $(\alpha h v)^2 = f(h v)$ dependence. An extrapolation of the linear region to the photon energy axis allowed us to determine the bandgap energy, as shown in Fig. 3.
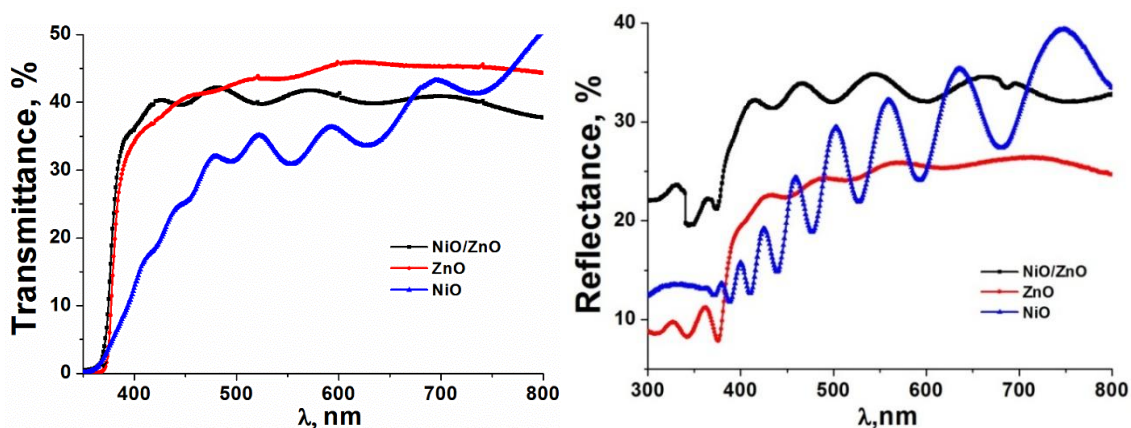
Fig. 2. Optical transmittance and reflectance spectra of the sputtered NiO thin film, the ZnO:Ga thin film thermally annealed in a vacuum, and the ZnO/NiO heterostructure.
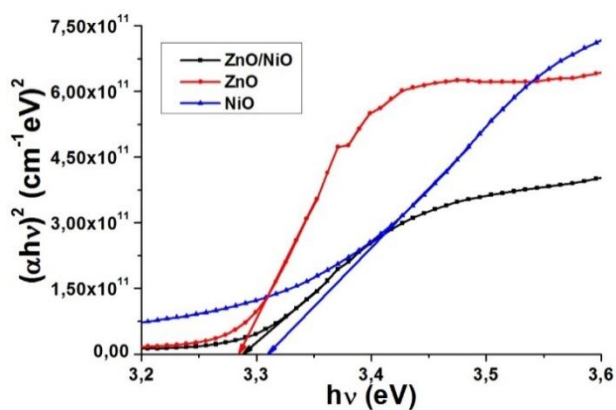
Fig. 3. The $(\alpha h v)^2 = f(h v)$ dependence of the sputtered NiO thin film, the ZnO:Ga thin film thermally annealed in a vacuum, and the ZnO/NiO heterostructure.

The optical band gaps of the ZnO :Ga, NiO thin films were calculated and indicated a direct transition. The band gap extracted from the $(\alpha h v)^2 = f(h v)$ dependence for the NiO thin film shows a value of 3.32 eV, while for ZnO:Ga and NiO/ZnO:Ga it shows the same value of

3.28 eV. The optical band gap values of these films are in the same range as those reported for bulk materials.

To study the effect of the thin film resistivity on the rectifying characteristics of the NiO/ZnO:Ga heterojunction, the ZnO:Ga thin films were annealed at 450°C in an O_2 atmosphere for different durations. As shown in Fig. 4a, an obvious tendency to decreasing can be observed for the forward current of the NiO/ZnO:Ga heterojunction with an increase in the annealing time. It is evident that annealing in an O_2 atmosphere causes an increase in the resistivity of the ZnO:Ga thin film. In addition, it is revealed that the longer the annealing time, the more resistant the ZnO:Ga thin film. If a forward bias is applied to the heterostructure, in addition to the voltage falling across the depletion region, part of the voltage will drop across the highly resistive ZnO:Ga region. In this case, it is reasonable to expect a smaller forward current. In addition, the highly resistive ZnO:Ga region also restricts the current passing through the entire heterostructure. Thus, a tendency to decreasing is observed for the forward current with an increase in the resistivity of the ZnO:Ga thin film. The best rectifying performance with a rectification coefficient of 10^5 at ±1 V was obtained for the NiO/ZnO:Ga heterojunction without annealing in an O_2 atmosphere.
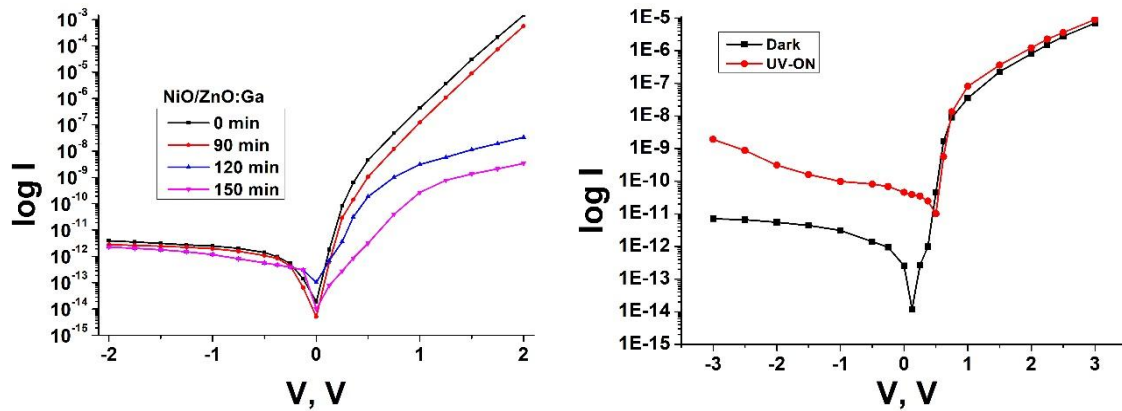
Fig. 4. (a) Current-voltage characteristics of the NiO/ZnO:Ga heterojunction with the ZnO:Ga thin film annealed in a vacuum for 0, 90, 120, and 150 min and (b) I–V characteristics under 365-nm UV light illumination for a heterojunction with the *non-annealed (0 min)* ZnO:Ga thin film.

Figure 4b illustrates the photoelectric response to the UV illumination of the *p*-NiO/*n*-ZnO:Ga heterojunction. The reverse dark current measured at –3 V is ~6.2×10^{-12} A. This finding shows the typical behavior of a *p–n* junction; that is, a higher acceptor concentration in the *p*-NiO layer leads to a lower reverse current. It is obvious that the UV illumination of the *p*-NiO/*n*-ZnO:Ga heterojunction causes an increase in the reverse current by about two orders and thereby shows a promising application in UV light detection. The phenomena could be attributed to the effect of the UV-induced hole trapping in the *p*-NiO layer. The UV illumination produces electron–hole pairs in both the *p*-NiO and *n*-ZnO:Ga layers. If some of the UV-generated holes are trapped in the deep-levels in the *p*-NiO layer, the I–V characteristic of the *p-n* junction will be affected by the hole trapping. The hole trapping will partially compensate for the negative space charge in the *p*-NiO side of the depletion region of the *p–n* junction, while reducing the built-in electric field and the barrier height of the *p–n* junction.

4. Conclusions

Thus, the *p*-NiO/*n*-ZnO:Ga thin film heterojunctions have been prepared for both rectifier diode and UV photodetector applications. For the diode application, the conductivities of both the NiO and ZnO:Ga thin films have a strong effect on the rectifying characteristic of the heterojunction diode. The best rectifying performance has been obtained for the diode with both highly conductive NiO and ZnO:Ga thin films. The evolution of the electrical properties studied by the I–V measurements has shown that vacuum annealing suppresses the rectifying nature of the annealed heterojunctions. The photocurrent to dark current ratio for the *p*-NiO/*n*-ZnO:Ga thin film heterojunction upon applying a 1 V reverse bias is about 35.

References

[1] S. P. Ghosh, K. C. Das, N. Tripathy, G. Bose, et al., IOP Conf. Ser.: Mater. Sci. Eng. 115, 012035 (2016).

[2] N. Park, K. Sun, Z. Sun, Y. Jing, and D. Wang, J. Mater. Chem. C. 1, 7333 (2013).

[3] S. Huang, N. Yu, T.Wang, and J. Li, Func. Mater. Lett. 11, 1850045 (2018).

[4] A. Adhikary, S. Ahsan, M. Hossain, B. Hossain, S. Newaz, F. Ahmed, and Ik-Bu Sohn, Opt. Eng. 59, 117108 (2020).

[5] K.Dy, J. Ryu, J. Manders, J. Lee, and F. So, Appl. Mater. Interfaces 6, 1370 (2014).

[6] P. Liu, T. P. Chen, X. D. Li, Z. Liu, J. I. Wong, Y. Liu, and K. C. Leong, ECS Solid State Lett. 2, Q21 (2013).

[7] K. Kobayashi, M. Yamaguchi, Y. Tomita, and Y. Maeda, Thin Solid Films 516, 5903 (2008).

[8] H.-L. Chen, Y.-M. Lu, and W.-S. Hwang, Surf. Coat. Technol. 198, 138 (2005).

[9] P. Salunkhe et al., Mater. Res. Express 7, 016427 (2020).

[10] M. Yang, H. Pu, Q. Zhou, and Q. Zhang, Thin Solid Films 520, 5884 (2012).

[11] H. Lee, Y. T. Huang, M. W. Horn, et al., Sci. Rep. 8, 5590 (2018).

[12] H. Ohta, M. Hirano, K. Nakahara, H. Maruta, T. Tanabe, M. Kamiya, T. Kamiya, and H. Hosono, Appl. Phys. Lett. 83, 1029 (2003).

[13] H. K. Li, T. P. Chen, S. G. Hu, X. D. Li, Y. Liu, P. S. Lee, X. P. Wang, H. Y. Li, and G.. Q. Lo, Express 23, 27683 (2015).

[14] E. Chong, Y. S. Chun, S. H. Kim, and S. Y. Lee, El. Eng. Technol. 6, 539(2011).

[15] M. Razeghi, J. H. Park, R. McClintock, D. Pavlidis, F. H. Teherani, D. J. Rogers, B. A. Magill, G. A. Khodaparast, Y. Xu, J. Wu, et al., Proc. SPIE, 10533 (2018).

[16] H. Aida, K. Nishiguchi, H. Takeda, et al., Jpn. J. Appl. Phys. 47, 8506 (2008).

[17] S. Annathurai, S. Chidambaram, M. Rathinam, and G. K. Prasanna Venkatesan, J. Mater. Sci.: Mater. Electron. 30, 5923 (2019).

[18] N. Park, K. Sun, Z. Sun, Y. Jing, and D. Wang, J. Mater. Chem., C 1, 7333 (2013).

COORDINATION COMPLEX [Eu(μ₂-OC₂H₅)(btfa)(NO₃) (phen)]₂·phen

WITH HIGH LUMINESCENT EFFICIENCY

Mihail S. Iovu[1], Victor I. Verlan*[1], Ion P. Culeac[1], Olga Bordian[1], Vera E. Zubareva[2], Ion Bulhac[2], Marius Enachescu[3], Nichita A. Siminel[1], and Anatol V. Siminel[1]

[1]*Institute of Applied Physics, Academiei str.5, Chisinau, MD-2028 Republic of Moldova*
[2]*Institute of Chemistry, Academiei str.3, Chisinau, MD-2028 Republic of Moldova*
[3]*University Politehnica Bucharest, Splaiul Independentei 313, Bucharest, 060042 Romania*
E-mail: vverlan@gmail.com

Abstract

Experimental results on the bis[(μ₂-etoxi)(benzoyl trifluoroacetonato)(nitrato)(1,10-phenantroline)europium(III)]1,10-phenantroline europium(III) coordination complex (hereafter, [Eu(μ₂-OC₂H₅)(btfa)(NO₃)(phen)]₂·phen) are described. The complex is characterized by photoluminescence (PL) and infrared spectroscopy. Photoluminescence spectra of the complex exhibit strong emission with specific narrow emission bands associated with the $^5D_0\rightarrow{^7}F_j$ ($j = 0–4$) transitions. The pattern of emission band splitting and the luminescence time decay suggest the presence of at least two different sites of the Eu^{3+} ion in a low-symmetry environment. The absolute PL quantum yield of the complex is determined to be 49.2%.

Keywords: rare-earth compounds, europium (III) complex, luminescence, quantum yield.

Rezumat

Sunt prezentate rezultate experimentale pentru complexul coordinativ al europiului III) - [Eu(μ₂-OC₂H₅)(btfa)(NO₃)(phen)]₂phen. Complexul a fost caracterizat prin spectroscopia de fotoluminescență și spectroscopia în infraroșu. Spectrele de fotoluminescență ale complexului reprezintă benzi de emisie puternice asociate cu tranzițiile $^5D_0\rightarrow{^7}F_j$ (j=0-4). Caracterul despicării benzilor de emisie, cât și timpul de relaxare al luminescenței indică prezența a cel puțin două site-uri diferite ale ionului Eu^{3+} în mediu cu simetrie redusă. A fost determinat randamentul cuantic absolut al complexului de 49,2%.

Cuvinte cheie: compuși de pământ rar, complex Europium (III), luminescență, randament cuantic.

1. Introduction

Rare-earth compounds, and specifically their coordination complexes, attract a lot of interest because of their fundamental physical properties and numerous applications in different

fields in optoelectronics, biotechnology, biochemistry, medicine, and other industries [1–3]. Complexes with trivalent europium ion Eu^{3+} exhibit high fluorescence efficiency upon UV excitation, emission spectra in the visible range with high color purity and a large Stokes shift, long-lived luminescence, etc. [4–6]. This luminescence is characterized by long lifetimes and sharp spectral lines. In biomedical field, europium(III) complexes are extensively used for the development of high-performance sensors, luminescent labels in immunoassays, bioanalysis, etc. [7]. Europium ions are characterized by a simple structure of $^{2S+1}L_J$ multiplets with non-degenerate first excited and ground levels, $^5D_0$ and $^7F_0$. Because of these specific properties of trivalent europium ion, it can be used as a luminescent probe to acquire information on the local symmetry in crystalline host matrices or glasses as well as complexes with organic ligands [8–10].

In the recent years, increased research efforts have been focused on new lanthanide complexes with potential development toward material sciences, chemical and biomedical applications, quantum storage devices, etc. [11, 12]. Previously, we reported preliminary results on Eu(III) coordination compound bis[(μ$_2$-etoxi)(benzoyl trifluoroacetonato)(nitrato)(1,10-phenantroline)europium(III)]1,10-phentroline, hereafter [Eu(μ$_2$-OC$_2$H$_5$)(btfa)(NO$_3$)(phen)]$_2$·phen [13]. This work reports a further study of photoluminescence (PL) properties of europium(III) coordination complex [Eu(μ$_2$-OC$_2$H$_5$)(btfa)(NO$_3$)(phen)]$_2$·phen.

2. Preparation and Characterization of the Complex

Europium(III) coordination complex [Eu(μ$_2$-OC$_2$H$_5$)(btfa)(NO)$_3$(phen)]$_2$·phen has been synthesized as described elsewhere [14]. Samples were characterized by infrared (IR) and PL spectroscopy. Infrared spectra were registered using a PerkinElmer Spectrum 100 FTIR Spectrometer at a resolution of 1 cm^{-1}. Infrared spectra were recorded on a dry powder between KBr pellets (4000–650 cm^{-1}) or in Nujol mull (4000–400 cm^{-1}) between KBr pellets. Photoluminescence emission spectra were recorded using a single emission monochromator MDR-23 and different excitation sources (337 or 405 nm) close to ligand absorption maximum. Photoluminescence spectral measurements were carried out using a Thorlabs LD Model CPS405 4.5 mW as an excitation source. A 337-nm pulsed nitrogen laser at a repetition rate of 10–100 Hz and a pulse width of 10 ns was used for PL relaxation measurements. Photoluminescence signal was detected in a photon counting mode using a Hamamatsu H8259-01 module with a C8855-01 counting unit connected to a PC. The spectral resolution for PL measurements was as low as 0.125 nm. For both the PL spectra and the quantum yield measurements, the emission spectra were corrected for the instrument spectral sensitivity. The luminescence time decay was recorded using a nitrogen pulsed laser as a light source at a repetition rate of 10 Hz. The H8259-01 PMT module with a C8855-01 pulse-counter provides time-resolved measurements at a resolution of 50 μs, which is sufficient for registration of PL relaxation in a range of 50 μs to 10 ms.

The [Eu(μ$_2$-OC$_2$H$_5$)(btfa)(NO)$_3$(phen)]$_2$·phen complex exhibits a bright-red emission under UV irradiation. Figure 1 shows a photographic image of a powder sample under day-light illumination compared with the sample under UV irradiation. Measurements of absolute PL quantum yield were performed using the absolute method of integration sphere [15]. The integration sphere was 150 mm in diameter. The inner spherical cavity wall was coated with MgO (extremely high diffuse reflectance) using a burning magnesium ribbon in an O$_2$ stream. The sphere was mounted in front of an MDR-23 monochromator. Absolute quantum yield Q is

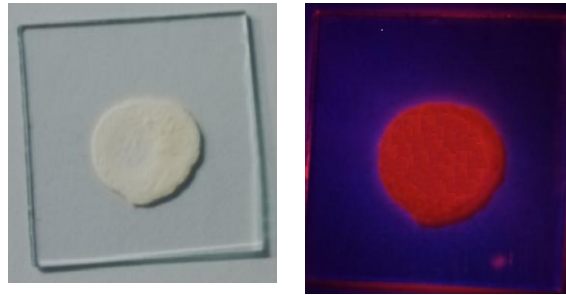defined as the ratio of the number of emitted photons N_{em} to the number of absorbed photons [16]:

Fig. 1. Photographic image of a powder sample: (left) under day-light illumination and (right) under UV irradiation.

$$Q = N_{em}/N_{abs}.$$

Figure 2 illustrates the experimental approach for measuring the absolute quantum yield. First, the excitation spectrum is registered when the substrate is placed under a direct excitation beam in a sample holder. The total area under this spectrum (S_0) is proportional to the number of excitation photons minus those absorbed in the substrate. In the next step, the excitation spectrum is registered when the substrate with a PL compound is placed under an excitation beam in a sample holder. The area under this spectrum (S_1) is proportional to the number of excitation photons minus those absorbed in the substrate and the compound. The PL emission spectrum was registered with a probe (substrate with the sample powder) placed inside a sample holder. The area under the PL spectrum (S_2) is proportional to the number of emission photons under direct and diffuse excitation. Finally, the PL spectrum is registered when the probe is excited only by indirect excitation light diffusively reflected from the integrating sphere walls (S_3). The quantum yield is determined as $Q = (S_2 - S_3)/(S_0 - S_1)$ [15, 16].
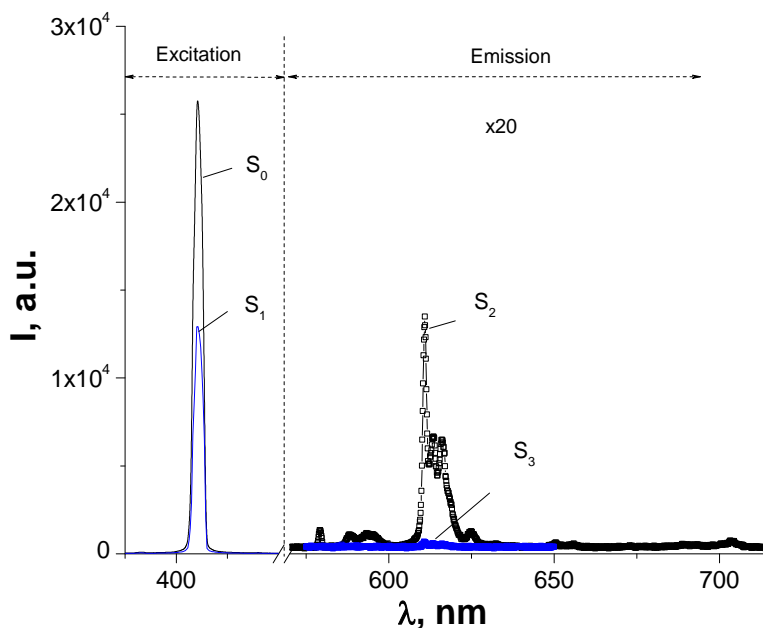

Fig. 2. Illustration of the spectra for the determination of quantum yield: S_0 is the excitation spectrum registered with the substrate under an excitation beam in a sample holder; S_1 is the excitation spectrum registered with a probe under an excitation beam; S_2 is the PL emission spectrum registered with the probe under an excitation beam; and S_3 is the PL emission spectrum registered when the probe is excited by indirect excitation light diffused by the integration sphere walls.

3. Infrared Transmission Spectra

Infrared spectra were registered using a PerkinElmer Spectrum 100 FTIR Spectrometer with at a resolution of 1 cm^{-1}. Infrared spectra were recorded on a dry powder between KBr pellets (4000–650 cm^{-1}) or in Nujol mull between KBr pellets (4000–400 cm^{-1}). Absorption bands in the IR spectrum were identified by comparing with the reference data [17, 18]. The absorption bands corresponding to the basic structural units of the [Eu(μ_2-OC$_2$H$_5$)(btfa)(NO)$_3$(phen)]$_2$·phen complex are listed in Table 1.

Table 1. Ligands absorption bands in the complex related to the basic structural units

Ligand	Structural unit	ν, cm^{-1}
btfa	ν(C=O)	1610
	ν_{as}(CF$_3$)	1180
	ν_s(CF$_3$)	1135
	δ(CH)	731; 700
o-phen	ν(C=N)	1637
	ν(C=C)	1675; 1498; 1441
OC$_2$H$_5$	ν_{as}(CH$_2$/CH$_3$)	1459
	ν_{as}CH$_2$/CH$_3$)	1377
	Scissor oscillation CH$_2$	1470
	δ(CH$_2$)	1466
NO$_3$	NO$^-_3$	1489; 1290; 1026

4. Photoluminescence Emission Spectra

Photoluminescence emission spectra were registered for both the powdered samples and the samples dissolved in a dimethylformamide solution under excitation of a 405-nm or 337-nm laser beam. The PL emission spectrum registered at 300 K in the powder sample (λ_{exc} 405 nm) is shown in Fig. 3a. Upon UV excitation, the Eu^{3+} complex exhibits well-known characteristic transitions ^{5}D$_0 \rightarrow ^7$F$_j$ (j = 0, 1, 2, 3, 4) with typical narrow band components. The complex shows strong emission bands in the solid state; less intense bands are registered in the dimethylformamide solution (Fig. 3b).

Mihail S. Iovu, Victor I. Verlan, Ion P. Culeac, Olga Bordian, Vera E. Zubareva, Ion Bulhac,
Marius Enachescu, Nichita A. Siminel, and Anatol V. Siminel

Less resolved Stark splitting and wider peaks of the emission bands are known to be a common feature of Eu(III) complexes in solution [21]. This difference in the degree of splitting suggests different degrees of distortion of the ligand crystal field in different media. With a decrease in temperature, the peak intensity of the basic emission bands increases and the resolution of emission band splitting also increases. Assignment of the emission lines is consistent with the predicted number of transition bands, which is based on the selection rules for low-symmetry complexes [19]. The strongest emission is related to the transition between excited state $^5D_0$ and ground state manifold $^7F_2$ due to an efficient energy transfer from higher excited states to $^5D_0$ [20]. Along with the transitions from the first excited state $^5D_0$, a number of extremely weak transitions from the higher excited state level $^5D_1$ can be observed (Fig. 3a): $^5D_1-^7F_0$ (526.8 nm), $^5D_1-^7F_1$ (533–543 nm), $^5D_1-^7F_2$ (551–573 nm), and $^5D_1-^7F_3$ (583 nm).
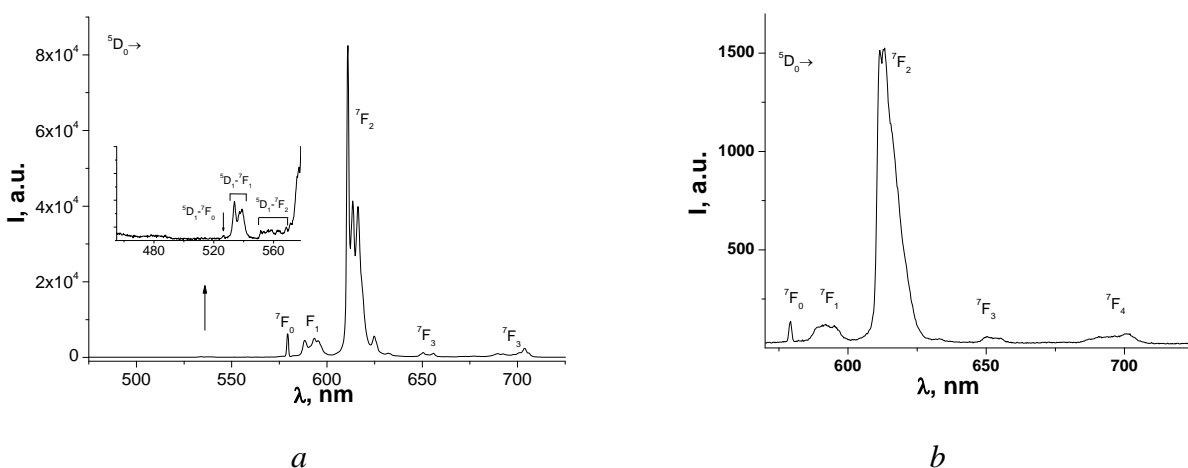
Fig. 3. Illustration of the PL spectrum of the europium(III) complex under 405-nm excitation ($T = 300$ K): (a) PL spectrum for the powder sample; the integrated intensity ratio is $R = 9.02$ and (b) PL spectrum of the complex in a dimethylformamide solution; the integrated intensity ratio is $R = 14.4$.

The band at ~580 nm represents the forbidden electric dipole transition $^5D_0\rightarrow^7F_0$, from the $^5D_0$ excited state to the $^7F_0$ ground state. The $^5D_0\rightarrow^7F_0$ transition is forbidden by the selection rules and commonly can be observed only in low-symmetry complexes, if the lanthanide ion is located on a site with C_{nv}, C_n, or C_s symmetry [8, 19]. It is one of the most remarkable features in the luminescence spectrum of the $[Eu(\mu_2\text{-}OC_2H_5)(btfa)(NO)_3(phen)]_2 \cdot phen$ complex. Since both the emitting $^5D_0$ and ground state $^7F_0$ of the transition are non-degenerate and cannot be split by the ligand field, the number of its components exactly indicates the number of different Eu^{3+} ion sites [19]. The band at 580 nm has a small line width, which at 300 K equals 32 cm^{-1} for the powder sample and 45 cm^{-1} for the solution sample (Figs. 3, 4). Although the low-resolution spectrum for the $^5D_0\rightarrow^7F_0$ transition reveals an almost symmetrical single line (Fig. 5), its

relatively wide full width at half maximum suggests that it can contain two closely spaced components. In fact, deconvolution of the emission band $^5D_0{\rightarrow}^7F_0$ (Fig. 5) reveals two lines, and this is consistent with the assumption of existence of two different sites of the Eu^{3+} ion.

The $^5D_0{\rightarrow}^7F_1$ transition with the emission band at 587–600 nm is a purely magnetic dipole transition; it represents the crystal field splitting of the $^7F_1$ level. An important feature of this transition is that its integrated intensity is relatively insensitive to the local crystal field induced by ligands surrounding the Eu^{3+} ion. Therefore, the $^5D_0{\rightarrow}^7F_1$ transition is used as a reference in comparing the absolute emission intensities within the Eu(III) spectrum [8, 10]. The pattern of splitting of the $^5D_0{\rightarrow}^7F_1$ transition provides information to which crystal system the complex corresponds. In the case of complexes with low symmetry (orthorhombic or lower symmetries) the maximum splitting of three lines appears [8, 19]. In Fig. 6, we can distinguish the $^5D_0{\rightarrow}^7F_1$ splitting into more than six components (peaks and shoulders), which can be attributed to the existence of at least two distinct, although chemically quite similar, emitting Eu^{3+} centers in the complex [22, 23].

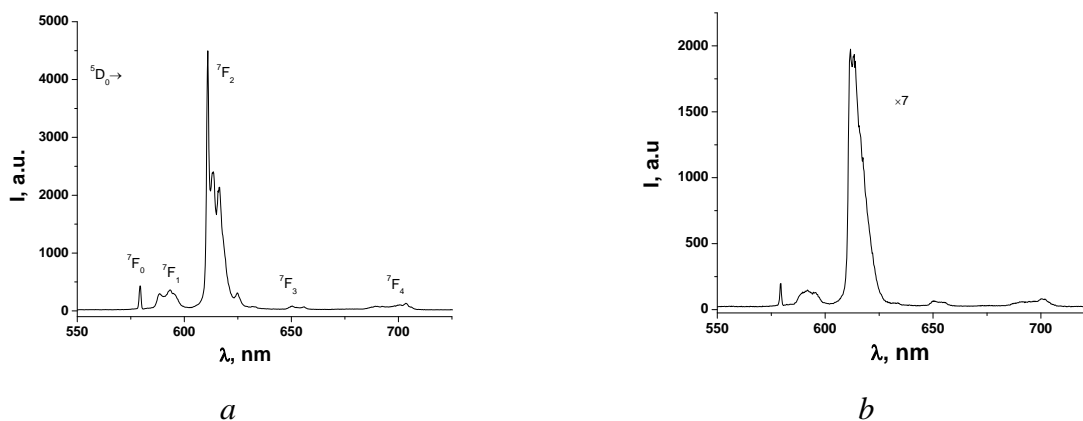|	
a	*b*

Fig. 4. Photoluminescence spectrum of the europium(III) complex under 337-nm excitation ($T = 300$ K): (a) PL spectrum for the powder sample; the integrated intensity ratio is $R = 7.18$ and (b) PL spectrum of the complex in a dimethylformamide solution; the integrated intensity ratio is $R = 11$.
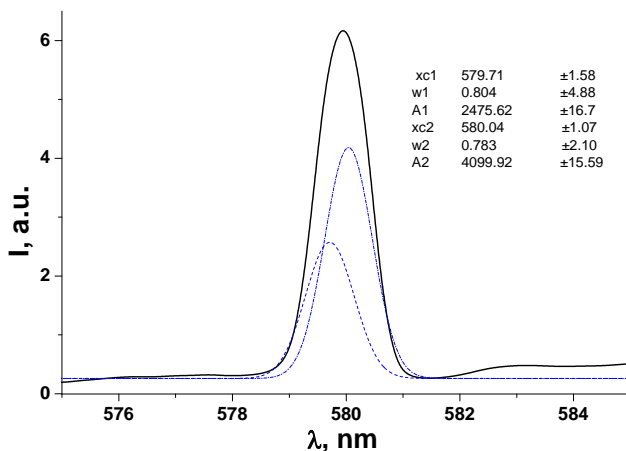

Fig. 5. Deconvolution of the emission band at ~580 nm attributed to the $^5D_0{\rightarrow}^7F_0$ transition in the case of the powder sample ($T = 300$ K, $\lambda_{exc} = 405$ nm).

Mihail S. Iovu, Victor I. Verlan, Ion P. Culeac, Olga Bordian, Vera E. Zubareva, Ion Bulhac,
Marius Enachescu, Nichita A. Siminel, and Anatol V. Siminel

The dominant feature in the PL spectrum of the $[Eu(\mu_2\text{-}OC_2H_5)(btfa)(NO)_3(phen)]_2\cdot phen$ compound is the $^5D_0\rightarrow^7F_2$ electric dipole transition with the emission band at 610–630 nm (Fig. 6). It is this transition that is responsible for the typical bright red luminescence observed in most of the europium(III) compounds. Since its intensity is sensitive to the local symmetry of the Eu^{3+} ion and the nature of the ligands, the $^5D_0\rightarrow^7F_2$ transition is considered as a "hypersensitive" transition [8–10]. The PL spectrum of the $[Eu(\mu_2\text{-}OC_2H_5)(btfa)(NO)_3(phen)]_2\cdot phen$ compound shows that the $^5D_0\rightarrow^7F_2$ transition is much more intense than the $^5D_0\rightarrow^7F_1$ magnetic dipole transition (Figs. 4, 6). The asymmetric ratio R, which is defined as an integrated intensity ratio $I_2(^5D_0\rightarrow^7F_2)/I_1(^5D_0\rightarrow^7F_1)$ is equal to 9.02 for the powdered sample; for the sample dissolved in a dimethylformamide solution, the ratio is 14.4 (λ_{exc} = 405 nm). This high magnitude of asymmetric ratio R suggests that the Eu(III) ion is not at an inversion center [19]. At a low temperature of 10.7 K, the $^5D_0\rightarrow^7F_2$ transition splitting into at least ten components and shoulders can be observed; this multiple splitting is consistent with the existence of at least two sites of the Eu(III) ion.
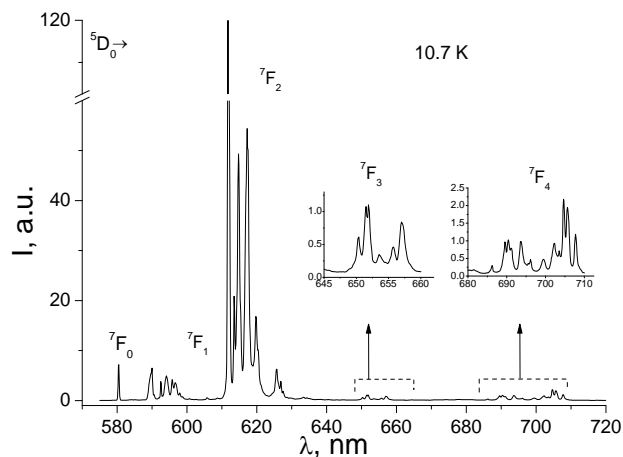

Fig. 6. Photoluminescence spectrum for the powder $[Eu(\mu_2\text{-}OC_2H_5)(btfa)(NO)_3(phen)]_2\cdot phen$ sample measured at 10.7 K. The insets show the splitting of the $^7F_3$ and $^7F_4$ bands. The excitation light is 405 nm.

The other two emission bands corresponding to the $^7F_3$, and $^7F_4$ levels, which are electric dipole transitions, are extremely weak. The $^5D_0\rightarrow^7F_3$ transition at 640–655 nm is a forbidden electric dipole transition, which is the weakest in the spectrum of the compound. This transition can only gain intensity via J-mixing [10]. Another electric dipole transition is the $^5D_0\rightarrow^7F_4$ emission band at 680–710 nm. The $^5D_0\rightarrow^7F_4$ transition is slightly higher than the $^5D_0\rightarrow^7F_3$ transition. It is considered to be sensitive to the Eu^{3+} environment, because the intensity of the $^5D_0\rightarrow^7F_4$ transition is determined not only by symmetry factors, but also by the chemical composition of the host matrix [23–25].

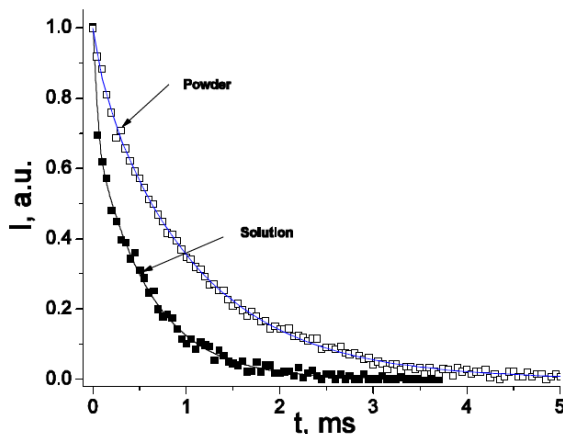**Fig. 7.** Photoluminescence decay profiles for the powder and dissolved sample of the
$[Eu(\mu_2\text{-}OC_2H_5)(btfa)(NO_3)(phen)]_2 \cdot phen$ complex at 300 K registered at 611 nm under 337-nm pulsed
excitation [13].

Photoluminescence decay curves of the complex were registered at 300 K for the
$^5D_0 \to {}^7F_2$ transition at 611 nm. Temporal characteristics of the PL exhibit a bi-exponential decay
for both the powder sample and the sample dissolved in a dimethylformamide solution (Fig. 8).
The PL decay curves can be fitted by the two-exponential function:

$$I(t) = A_1 \exp(-t/\tau_1) + A_2 \exp(-t/\tau_2),$$

where A_1 and A_2 are pre-exponential factors; τ_1 and τ_2 are the time constants.

The lifetime constants for Eu^{3+} obtained from the plot in Fig. 8 are $\tau_1 = 0.67$ ms and
$\tau_2 = 0.82$ ms for the powdered sample and $\tau_1 = 0.28$ ms and $\tau_2 = 0.57$ ms for the complex
dissolved in a dimethylformamide solution [13]. The absolute quantum yield of PL measured in
the powder samples by the integration sphere was determined to be 49.2%, while the sensitization
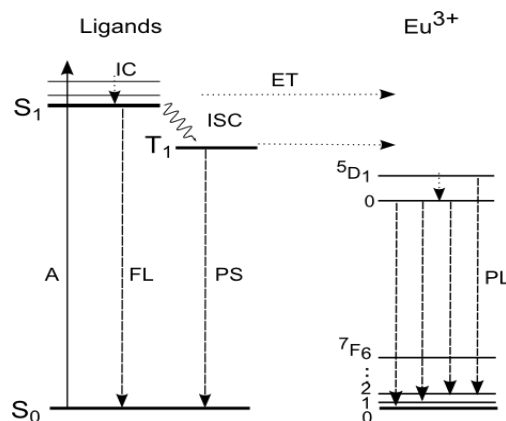efficiency was 89.3%.

Fig. 8. Illustration of the mechanism of energy transfer from the organic ligand to the Eu^{3+} ion: S_0,
S_1, and T_1 are the singlet ground state, singlet excited state, and triplet state, respectively. A is
absorption, FL is fluorescence, PS is phosphorescence, IC is internal conversion, ISC is intersystem
crossing, and ET is energy transfer.

Mihail S. Iovu, Victor I. Verlan, Ion P. Culeac, Olga Bordian, Vera E. Zubareva, Ion Bulhac,
Marius Enachescu, Nichita A. Siminel, and Anatol V. Siminel

Photoluminescence spectra can be interpreted in terms of energy transfer from organic ligands to the Eu(III) ion [10, 23]. Figure 8 illustrates the mechanism of energy transfer from organic ligands to the Eu(III) ion. Under UV radiation, the organic ligand of the complex is excited from the singlet ground state S_0 to a vibration level of the first excited singlet state S_1. There are three possible deactivation transitions of excited electrons from the singlet S_1 state. These transitions are as follows: (i) radiative transitions from excited singlet state S_1 to ground state S_0, which contribute to the ligand molecule fluorescence and the excitation of $4f$ shell electrons through the Foerster mechanism; (ii) non-radiative transitions from singlet state S_1 to triplet state T_1; and (iii) a Dexter transition of excited electrons from the S_1 level to the $4f$ shell levels of the Eu^{3+} ion. Triplet state T_1 can be deactivated similarly to the S_1 state, which results in the phosphorescence of the ligand molecule (Foerster mechanism), or through intramolecular energy transfer from the T_1 state to the $4f$ level of the Eu^{3+} ion (Dexter mechanism), which results in Eu^{3+} luminescence emission [19–22].

Further studies will be performed to extend the described preliminary PL results. Currently, research is progressing on powder pattern X-ray diffraction measurements aimed at the structural characterization of the compound.

5. Conclusions

The $[Eu(\mu_2\text{-}OC_2H_5)(btfa)(NO)_3(phen)]_2 \cdot phen$ complex has been characterized by IR and PL spectroscopy. Upon UV excitation, the Eu^{3+} complex exhibits well-known characteristic transitions $^5D_0 \rightarrow ^7F_j$ ($j = 0$–4) with typical narrow emission bands. Although the $^5D_0 \rightarrow ^7F_0$ transition represents a single line, its full width at half maximum is relatively large of about 32 cm^{-1}; this fact suggests that it can contain two closely spaced components. Both the emission spectra and the PL decay characteristics indicate the presence of two different sites of the Eu^{3+} ion. The absolute PL quantum yield and the sensitization efficiency have been determined to be 49.2 and 89.3%, respectively. We believe that this high luminescence material can be useful for various applications in optoelectronics.

References

[1] Lanthanide Luminescence: Photophysical, Analytical and Biological Aspects, Springer Series on Fluorescence, Methods and Applications, Ed. by Pekka Hanninen and Harri Harma, Springer-Verlag, Berlin, Heidelberg, vol. 7, 2011. DOI: 10.1007/4243-2010-3

[2] J.-C. G. Bunzli, A.-S. Chauvin, C. D. B. Vandevyver, Song Bo, and S. Comby, Ann. N. Y. Acad. Sci. 1130, 97 (2008). DOI: 10.1196/annals.1430.010 9

[3] S. V. Eliseeva, and J.-C. G. Bunzli, Chem. Soc. Rev. 39, 189 (2010).

[4] Lanthanide Probes in Life, Chemical and Earth Sciences: Theory and Practice, Ed. by J.-C.G. Bunzil and G.R. Choppin, Elsevier, Amsterdam–Oxford–New York–Tokyo, 1989.

[5] A. P. Demchenko, Introduction to Fluorescence Sensing, Second Edition, Springer International Publishing, Switzerland, 2015. ISBN 978-3-319-20779-7 ISBN 978-3-319-20780-3 (eBook), DOI: 10.1007/978-3-319-20780-3

[6] Fluorescence Spectroscopy in Biology. Advanced Methods and their Applications to Membranes, Proteins, DNA, and Cells, Springer Series on Fluorescence, vol. 3: Methods and Applications, Ed. by M. Hof, R. Hutterer, and V. Fidler, Springer-Verlag, Berlin, Heidelberg, 2005.

[7] P. R. Selvin, Annu. Rev. Biophys. Biomol. Struct. 31, 275 (2002), DOI: 10.1146/annurev.biophys.31.101101.140927

[8] K. Binnemans, Coord. Chem. Rev. 295, 1 (2015).

[9] J.-C. G. Bünzli and G. O. Pradervand, J. Chem. Phys. 85, 2489 (1986), DOI: 10.1063/1.451057

[10] G. Blasse and B.C. Grabmaier, Luminescent Materials, Springer-Verlag, Berlin, Heidelberg, 1994.

[11] (a) Guangfu Li, Dongxia Zhu, Xinlong Wang, Zhongmin Su, and Martin R. Bryce, Chem. Soc. Rev. 49, 765 (2020); (b) J. J. Baldoví and A. Kondinski, Inorganics 6 (4), 101 (2018); DOI:10.3390/inorganics6040101; (c) D. Aguilà, L. A Barrios, V. Velasco, O. Roubeau, A. Repollés, P. J. Alonso, J. Sesé, S. J. Teat, F. Luis, and G. Aromí, J. Am. Chem. Soc. 136 (40), 14215 (2014), DOI: 10.1021/ja507809w; (d) Monatsh. Chem. Chem. Mon. 145 (12), 1913 (2014).

[12] L. Armelao, D. Belli Dell'Amico, L. Bellucci, G. Bottaro, S. Ciattini, L. Labella, G. Manfroni, F. Marchetti, C.A. Mattei, and S. Samaritani, Eur. J. Inorg. Chem. 2018 (40), 4421 (2018). DOI:10.1002/ejic.201800747

[13] V. I. Verlan, I. P. Culeac, O. Bordian, V. E. Zubareva, I. F. Bulhac, M. S. Iovu, M. Enachescu, N. A. Siminel, and V.V. Nedelea, Luminescence Properties of a Novel Eu^{3+} Dinuclear Coordination Compound. In: I. Tiginyanu, V. Sontea, and S. Railean (Eds.), 4th Int. Conf. on Nanotechnologies and Biomedical Engineering, ICNBME 2019, IFMBE Proc., vol. 77, Springer, Cham. DOI:10.1007/978-3-030-31866-6-33

[14] (a) O. Bordian, V. Verlan, I. Culeac, M. Iovu, I. Bulhac, and V. Zubarev, Synthesis, Absorption and Photoluminescence Properties of the New Coordination Compound $Eu(DBM)_3(Ph_3PO)_1H_2O$, Advanced Topics in Optoelectronics, Microelectronics, and Nanotechnologies IX, Ed. by M. Vladescu, R. Tamas, and I. Cristea, Proc. of SPIE, vol. 10977, 109771E, 2018 SPIE CCC code: 0277-786X/18/$18, DOI: 10.1117/12.2323761;

(b) O. Bordian, V. Verlan, I. Culeac, M. Iovu, I. Bulhac, V. Zubarev, and M. Enachescu, Certificat de prioritate OSIM, Romania, A/0000 din 07-01-2019, Compus coordonativ al Eu(III) de tip dinuclear cu liganzi micsti avind proprietati de luminiscenta si procedeu de obtinere.

[15] K. Rurack, Fluorescence Quantum Yields: Methods of Determination and Standards, Springer Series on Fluorescence, 2008, vol. 5, pp. 101–145, Springer-Verlag, Berlin, Heidelberg, Published online: March 11, 2008, DOI:10.1007⁄4243 2008 019

[16] A.K. Gaigalas and L. Wang, J. Res. Natl. Inst. Stand. Technol. 113, 17 (2008).

[17] L. J. Bellamy, The Infrared Spectra of Complex Molecules, Methuen & Co. LTD, Willey, London, New York, 1971.

[18] K. Nakamoto, Infrared and Raman Spectra of Inorganic and Coordination Compounds, Wiley, New York, 1978, p. 239.

[19] J.-C.G. Bunzli, Lanthanide probes. In: Lanthanide Probes in Life, Chemical and Earth Sciences: Theory and Practice, Ed. by J.-C.G. Bunzil and G. R. Choppin, Elsevier, Amsterdam–Oxford–New York–Tokyo, 1989, Ch. 7.

[20] J. Georges and J. M. Mermet, Spectrochim. Acta, Part A, 49 (3), 397 (1993).

[21] L. N. Puntus, I. S. Pekareva, K. A. Lyssenko, A. S. Shaplov, E. I. Lozinskaya, A. T. Zdvizhkov, M. I. Buzin, and Y. S. Vygodskii, Opt. Mater. 32, 707 (2010).

Mihail S. Iovu, Victor I. Verlan, Ion P. Culeac, Olga Bordian, Vera E. Zubareva, Ion Bulhac,
Marius Enachescu, Nichita A. Siminel, and Anatol V. Siminel

[22] M. H. V. Werts, Luminescent Lanthanide Complexes: Visible Light Sensitised Red and Near-Infrared Luminescence, University of Amsterdam, Thesis (2000), Library of the University of Amsterdam, Digital Academic Repository, Amsterdam, The Netherlands.

[23] K. Binnemans, R. Van Deun, C. Gorller-Walrand, S. R. Collinson, F. Martin, D. W. Bruceand, and C. Wickleder, Phys. Chem. Chem. Phys. 2, 3753 (2000), DOI: 10.1039/b003379k

[24] J.-C. G. Bunzli and S. V. Eliseeva, Basics of Lanthanide Photophysics, In: Lanthanide Luminescence: Photophysical, Analytical, and Biological Aspects, Ed. by P. Hanninen and H. Harma, Springer Series on Fluorescence (2010), Springer-Verlag, Berlin, Heidelberg, 2010, DOI:10.1007/4243-2010-3

[25] Ye Jin, Jiahua Zhang, Shaozhe Lu, Haifeng Zhao, Xia Zhang, and Xiao-jun Wang, J. Phys. Chem. C 112, 5860 (2008).

26. I. P. Culeac, V. I. Verlan, O. Bordian, V. E. Zubareva, I. F. Bulhac, M. S. Iovu, M. Enachescu, N. A. Siminel, and A.V. Siminel, Synthesis and characterization of novel photoluminescent Eu(III) dinuclear coordination compound, submitted for publication in J. Phys. Chem.

STRUCTURAL AND OPTICAL PROPERTIES OF ZnO:Ga THIN FILMS DEPOSITED ON ITO/GLASS SUBSTRATES FOR OPTOELECTRONIC APPLICATIONS

Dumitru Rusnac[1], Ion Lungu[1], Lidia Ghimpu[2], Gleb Colibaba[1], and Tamara Potlog[1]

[1]Moldova State University, A. Mateevici str. 60, Chisinau, Republic of Moldova
[2]D. GhituˑInstitute of Electronic Engineering and Nanotechnologies, Academiei str.3/3, Chisinau, MD-2028 Republic of Moldova
E mail: lidia.ghimpu@gmail.com

Abstract

Doped (with GaCl$_3$), undoped ZnO and ITO/ZnO:Ga nanostructured thin films are synthesized using the spray pyrolysis method. The doped ZnO thin films are synthesized at the atomic ratio of Ga/Zn added in the starting solution fixed at 1, 2, 3, and 5. Gallium-doped ZnO films synthesized on glass/ITO substrates are annealed at 450°C in different environments: vacuum, oxygen, and hydrogen. X-ray diffraction (XRD), Energy-dispersive X-ray spectroscopy (EDX), atomic force microscopy (AFM), and current–voltage (I–V) measurements are applied to characterize the structural properties, composition, surface morphology, and electrical properties of ZnO:Ga nanostructured thin films. X-ray diffraction analysis shows that ZnO:Ga films deposited on glass substrates have a dense and homogeneous surface with a hexagonal structure. The ZnO:Ga films deposited on glass/ITO substrates are composed of two phases, namely, hexagonal ZnO and cubic ITO. The I–V characteristics show the presence of good ohmic contacts between Al and In metals and ZnO:Ga thin films regardless of the nature of the substrate and the annealing atmosphere.

Keywords: zinc oxide, gallium, annealing, structural properties, film morphology.

Rezumat

Au fost sintetizate straturi subțiri nanostructurate ZnO atât dopate cu (GaCl$_3$), cât și nedopate, precum și straturi de ITO/ZnO:Ga, folosind metoda prin pulverizare cu piroliză. Straturile subțiri de ZnO dopate au fost sintetizate la raportul atomic Ga/Zn adăugat în soluția inițială fixă la 1, 2, 3 și 5 Straturile nanostructurate de ZnO dopate cu Ga obținute pe substraturi de sticlă/ITO au fost tratate termic la 450°C în diferite medii: vid, oxigen și hidrogen. S-au realizat măsurătorile de difracție cu raze X (XRD), spectroscopie cu raze X cu dispersie energetică (EDX), microscopie cu forță atomică (AFM), curent-tensiune (I-V) pentru a caracteriza proprietățile structurale, compoziția, morfologia suprafeței și proprietățile electrice ale straturilor subțiri de ZnO:Ga. Analiza XRD arată că stratul de ZnO:Ga depus pe substratul de sticlă are o suprafață densă și omogenă cu structura hexagonală. Stratul de ZnO:Ga depus pe substraturi de sticlă/ITO indică două faze, acestea fiind ZnO hexagonal și ITO cubic.

Caracteristica I-V prezintă contacte ohmice bune între metalele Al, In și straturile subțiri de ZnO:Ga, indiferent de natura substratului și de atmosfera de tratare termică.

Cuvinte-cheie: oxid de zinc, galiu, tratare termică, proprietăți structurale, morfologia straturilor subțiri.

1. Introduction

Zinc oxide has attracted great attention due to its versatile nature. Zinc oxide has a hexagonal wurtzite structure (*P63mc*) with lattice constants of $a = 3.252$ Å and $c = 5.313$ Å [1]. Zinc oxide is a wide bandgap semiconductor (3.37 eV at room temperature) that can be used in numerous applications, such as solar cells [2], flat displays, heat mirrors, thin-film transistors, and chemical sensors [3]. In particular, it is a promising alternative to indium tin oxide (ITO) in transparent conducting oxide applications due to its low cost, non-toxicity, and stability under hydrogen plasma [4, 5]. Zinc oxide thin films were synthesized by a wide variety of techniques, in particular, by chemical and physical routes, such as pulsed laser deposition [6], thermal evaporation [7], chemical vapor deposition [8, 9], electron beam evaporation [10], spray pyrolysis [11], sol–gel method [12], and magnetron sputtering on a variety of substrates [11]. The spray pyrolysis technique is one of these techniques to prepare large-scale production for technological applications. Recently, gallium (Ga) has engrossed great interest as a dopant due to enhanced structural, optical, electrical, and magnetic properties upon incorporation into a ZnO material. Gomez et al. [12] prepared gallium-doped zinc oxide (Ga:ZnO) thin films on glass substrates by the spray pyrolysis technique and found that ZnO:Ga exhibits the *n*-type conductivity with an electrical resistivity on the order of $8 \times 10^{-3}\ \Omega$ cm and an optical transmittance higher than 80% in the visible region. These results make chemically sprayed Ga:ZnO potentially applicable as transparent electrode in photovoltaic devices. According to Ramakrishna Reddy et el. [13], for higher [Ga]/[Zn] rates in solution, the Ga ions do not occupy more zinc sites, and a segregation of Ga in an oxide form takes place in the grain boundaries or interstices, which causes a decrease in the mobility and a consequent increase in the electrical resistivity. For low [Ga]/[Zn] ratios, the decrease in resistivity is attributed to an increase in the number of Ga atoms incorporated into the ZnO lattice in the Zn sites supplying one electron to the conduction band for each Ga atom until the maximum solubility of Ga into the ZnO lattice (minimum resistivity value) is reached [13]. Recently, many studies have been focused on the improvement of photoactivity by combining with other semiconductors, such as WO_3, ZnO, SnO_2, CdS, CuO, and Fe_2O_3 [14, 15]. In this study, bilayer ZnO films were grown under the same conditions on ITO layers with the same crystal structure. After deposition, the Ga-doped ZnO films were annealed in different environments: oxygen (O_2), hydrogen (H_2), and vacuum. To the best of the authors' knowledge, a similar study has not been carried out. The aim of this study is to optimize the preparation of Ga-doped ZnO deposited on ITO/glass substrate to explore their optoelectronic properties.

2. Experimental

Zinc oxide nanostructured thin films were synthesized using the spray pyrolysis method. Doped and undoped ZnO thin films were synthesized. The initial solution was prepared by dissolving zinc acetate $[Zn(CH_3COO)_2 \cdot 2(H_2O)]$ in a methanol–water solution in a ratio of 25 : 65

to obtain a concentration of 0.2 M. The solution was stirred at 50°C for 1 h. In addition, to prevent the aggregation process, a few drops of concentrated acetic acid were added to the starting solution. For doping of ZnO thin films, gallium trichloride ($GaCl_3$) was used. Glass substrates were treated ultrasonically in soapy water, acetone, ethanol, and finally in distilled water for 60 min and then dried at ~110°C for ~20 min in a hydrogen atmosphere after cleaning. The solution was sprayed at a flow rate of 12 mL/min onto cleaned soda-lime glass substrates and onto ITO substrates. Argon gas at a flow rate of 10 mL/min was used as the carrier gas. The substrate temperature was 450°C. The ZnO thin films were synthesized at an atomic ratio of Ga/Zn added in the starting solution fixed at 1, 2, 3, and 5. The vacuum thermal annealing of Ga-doped ZnO thin films deposited on a commercial ITO/glass substrate was performed at 450°C for 90 min in different environments, namely, vacuum, oxygen, and hydrogen. The structural properties of nanostructured thin films were characterized by X-ray diffraction measurements. Atomic force microscopy (AFM) experiments were performed using a Digital Instruments Dimension 3100 AFM instrument (Veeco Company) equipped with a Nanoscope IV controller. Standard silicon cantilevers with a spring constant between 4.0–4.4 mN were used in the tapping mode. Current–voltage characteristics of the device were measured using a Keithley 2400 power supply under dark conditions.

3. Results and Discussion

The XRD studies of Ga-doped ZnO thin films deposited on a glass substrate (not shown here) at the Ga/Zn fixed atomic ratio of 1, 2, 3, and 5 revealed a polycrystalline nature with the (0002) plane as the dominant orientation. The XRD studies of Ga-doped ZnO thin films suggest that all the characteristic peaks correspond to zinc oxide. The crystal-lattice parameters were determined on the basis of the most intensive (0002) crystallographic plane. The structural parameters are listed in Table 1. With a decrease in Ga concentration, the intensity of the preferred (0002) plane decreases disorderly. The highest intensity of the preferred (0002) diffraction plane is revealed for 5% Ga. In addition, it is observed that the full width at half maximum (FWHM) of the peak corresponding to the (0002) diffraction varied only slightly with an increase in the Ga doping concentration from 1 to 5 at %. The mean grain size values obtained from the Scherrer formula applied on the (0002) XRD peak of Ga-doped ZnO thin films are shown in Fig. 1. The grain sizes reached about 29.0 nm.
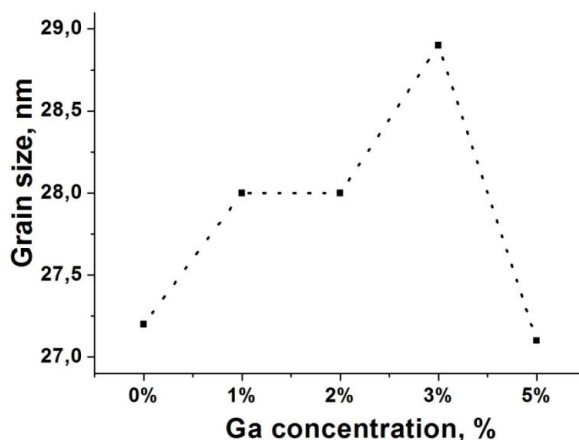

Fig. 1. Mean grain size value obtained from the Scherrer formula applied on the (0002) XRD peak of Ga-doped ZnO thin films.

The grain size of the 5%Ga-doped sample is found to be lower than that of the other doped samples, because the strain is inversely related to the grain size. According to Table 1, the internal strain values of the Ga-doped ZnO thin films do not change with an increase in the Ga concentration to 5%. The higher strain value of the 5%Ga-doped ZnO film shows that the crystallinity of the films is deteriorated. The peak broadening is a result of micro strains that appear due to the displaced atoms that are rearranged relative to their referenced lattice-points and due to the lattice defects occurring in the Ga-doped ZnO thin films. Probably, with an increase in the Ga concentration in the films, a contraction and decrease in the ZnO unit cell volume take place.

Table 1. Structural parameters of Ga-doped ZnO thin films

Samples	Gallium concentration , %	2θ (deg)	d, Å	FWHM, rad	ε (lattice strain) $\times 10^{-3}$
as-deposited ZnO	0	34.47	2.6010	0.0052	4.2
Gallium-doped ZnO thin films synthesized in an Ar atmosphere	1	34.51	2.5981	0.0054	4.3
	2	34.49	2.5996	0.0052	4.2
	3	34.50	2.5988	0.0052	4.2
	5	34.48	2.6003	0.0055	4.5

Energy-dispersive X-ray spectroscopy (EDX) measurements were performed to study the elemental composition of the Ga-doped ZnO thin films. The compositional analysis of the ZnO thin films doped with 5% Ga that were synthesized in an Ar atmosphere is shown in Fig. 2. Table 2 lists the weight and atomic percent compositions (wt % and at %) of the components of ZnO thin films. The respective patterns confirm that the average atomic percentage of Zn and oxygen deviates from the stoichiometry. The elemental analysis also proved the presence of the Ga dopant in the structure of the 5%Ga-doped ZnO thin film. Some impurities (Si, Ca) are found in the spectra; they originated from the glass substrate [16]. The presence of the Ga dopant is available for all the ZnO thin films, except for that doped with 1%.
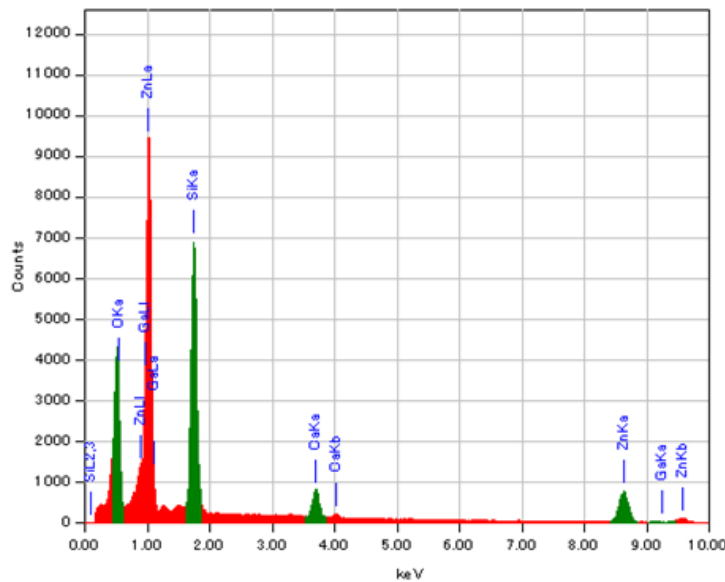

Fig. 2. Energy-dispersive X-ray spectra of the 5%Ga-doped ZnO thin film.

Table 2. Weight and atomic percent compositions (wt % and at %) of the 5%Ga-doped
ZnO thin film

Element	Weight %	Atomic %
O K	23.73	47.18
Si K	22.37	25.34
Ca K	4.05	3.22
Zn K	49.85	24.26
Ga K	0.16	0.08
Total	100.00	100.00

As described in the Introduction of this paper, ZnO is considered to be an *n*-type semiconductor, where the most of the defects are zinc interstitials (Zn_i) and oxygen vacancy (V_O). Excess zinc and oxygen deficiency in the synthesized ZnO thin films that were observed in this study can possibly be assigned to Zn_i in ZnO thin films.

Figure 3 shows XRD patterns of the ZnO thin films with a 3% Ga doping concentration that are deposited on commercial ITO/glass substrates, glass substrates, and commercial ITO deposited on a glass substrate. According to Fig.3, the XRD pattern of the ITO thin film revealed a polycrystalline nature with the preferred (400) plane. Other ITO peaks are observed at 2θ of 21.27°, 30.26°, 45.25°, 47.39°, 48.21°, 50.68°, 55.61°, and 60.25°. The ITO thin film crystallizes in a cubic structure. For the Ga-doped ZnO thin film deposited on a glass substrate, the most intense maximum is revealed at 2θ ≈ 35.2° with regard to the (0002) plane. The d_{hkl} value of 2.6129 Ǻ for Ga-doped ZnO thin films deposited on a glass substrate is higher than that of a standard ZnO powder (2.603 Å); this fact suggests that the crystalline plane distance of the Ga-doped ZnO film lengthens due to imperfections, such as lattice strains and interstitial defects. The crystal structures of the Ga-doped ZnO thin films deposited on commercial ITO/glass substrates are similar to each other and revealed weak diffraction maxima at 2θ = 47.39° and 62.71° for all the films deposited on ITO substrates, regardless of the annealing environment type, corresponding to the (1002) and (1003) diffraction planes. The XRD results revealed the polycrystalline nature of the films with a hexagonal wurtzite structure. The XRD peaks of the Ga-doped ZnO thin films deposited on commercial ITO/glass substrates are shifted toward the larger θ values; this shift leads to a decrease in the lattice parameter: $c = 5.1345$ Å compared with $c = 5.2331$ Å in the case of deposition on glass substrates. This decrease is directly related to the incorporation of Ga^{3+} ions in the Zn^{2+} substitutional sites. Then, the incorporation of the dopant into the ZnO matrix leads to a network contraction.
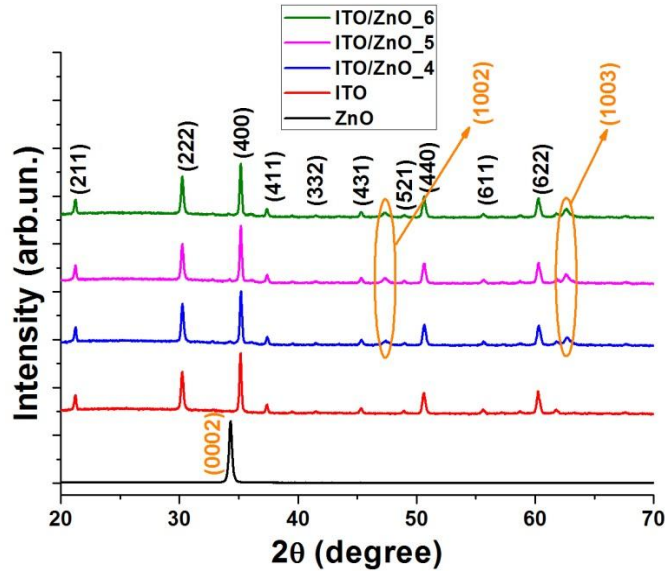
Fig. 3. X-ray diffraction patterns of the 3%Ga-doped ZnO thin films deposited on a commercial ITO/glass substrate annealed in different environments ((*4*) O_2, (*5*) H_2, (*6*) vacuum), 3%Ga-doped ZnO deposited on a glass substrate, and commercial ITO on a glass substrate.

The shift of Bragg's angles is attributed to changes in the interplanar spacing upon deposition on an ITO/glass substrate. The strain value for the 3%Ga-doped ZnO thin films deposited on a commercial ITO/glass substrate annealed in an oxygen atmosphere reached 5.4×10^{-3}. The lowest strain value (3.1×10^{-3}) was obtained for the Ga-doped ZnO thin films deposited on a commercial ITO/glass substrate annealed in a vacuum. The defects, impurities, and lattice strain lead to the presence of an intrinsic stress, whereas lattice mismatch and the thermal expansion coefficient mismatch give way to an extrinsic stress, which is developed between the film and the substrate [17].

The AFM images from Fig. 4 (left) show a columnar nanostructure and the occurrence of grain growth along the *c* axis, which is in good agreement with XRD analysis. It is observed that the grains grow uniformly with a homogenous distribution. The evolution feature can be more easily observed from the respective surface profiles of these films. The root mean square (RMS) roughness profiles of AFM images are compared in Fig. 4 (right). They indicate the formation of prominent wrinkles on the film surface. The height distribution over the surface of the Ga-doped ZnO thin films deposited on a commercial ITO/glass substrate annealed in an O_2 and H_2 atmosphere is sharp and wider compared with that in the case of the surface annealed in a vacuum.
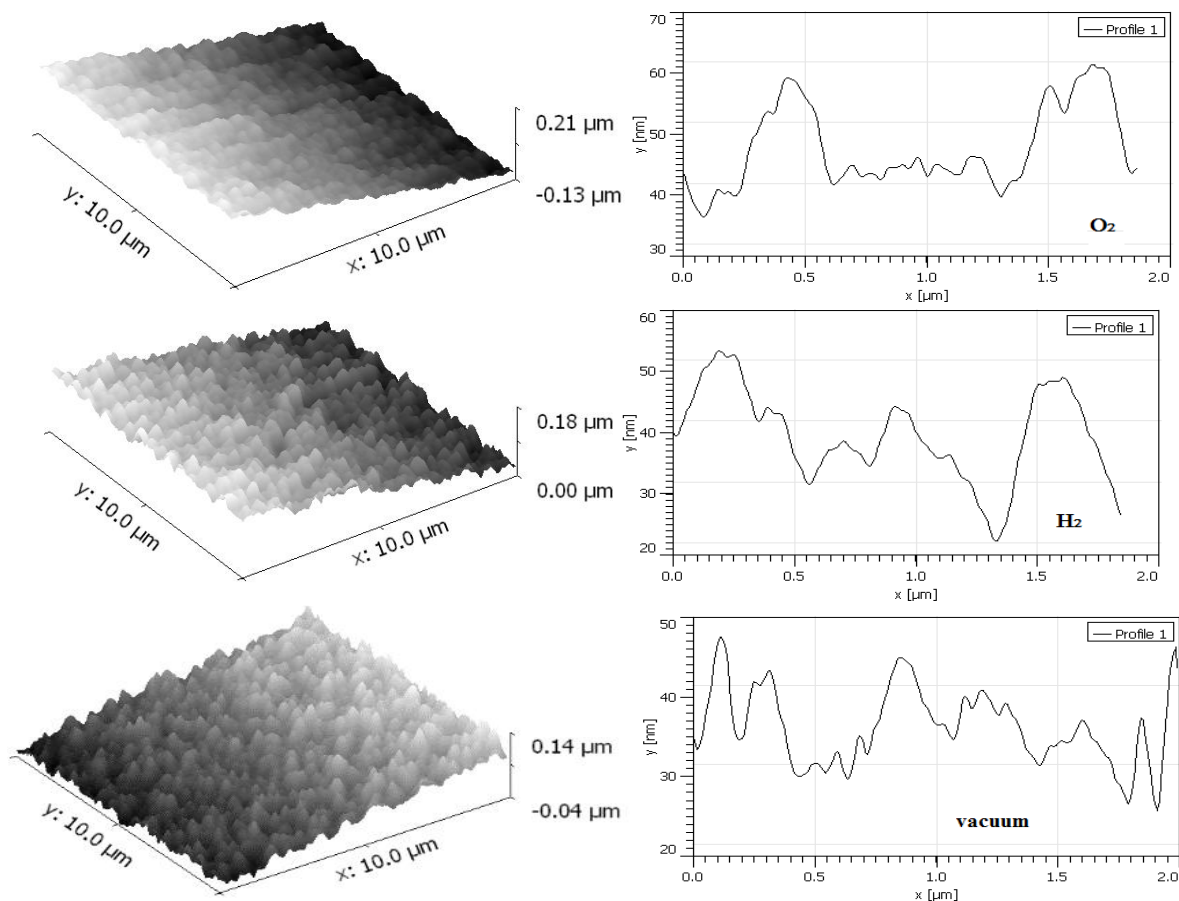
Fig. 4. Atomic force microscopy image of the 3%Ga-doped ZnO thin films deposited on a commercial ITO/glass substrate annealed in different environments and the relationship between (RMS) and profile scan.

Thus, it is evident from Fig. 4 that the interface width (RMS) values are slightly decreased for the Ga-doped ZnO thin film annealed in a vacuum.

Electrical properties play a key role in optoelectronic applications; it is well known that electrical characteristics are strongly affected by the doping content. As a result, the devices composed of glass/ITO/ZnO/metal contacts are manufactured to determine the effect of different metals on the electrical properties of the deposited ZnO thin films. Indium (In) and aluminum (Al) contacts were deposited by thermal evaporation through a mask having 2×2 mm^2 openings. Figure 5 shows the schematic representation of the fabricated glass/ITO/Ga:ZnO/Al and glass/ITO/Ga:ZnO/In samples (a) and dark current–voltage (I–V) characteristics of these devices (b).

Experimental results show good ohmic contacts between Al and In metals and ZnO thin films and the proportional increase in the current intensity to the supplied voltage for the films under both forward and reverse bias conditions. The current–voltage characteristics indicate also the increase in the slope of the I–V curves of the glass/ITO/Ga:ZnO contacts due to an increase in the Ga doping concentration in the ZnO lattice. This behavior can be attributed to the occupancy of a Ga ion on the Zn site acting as a donor, which can enhance the density of free charge carriers and the electrical conductivity of the ZnO films.
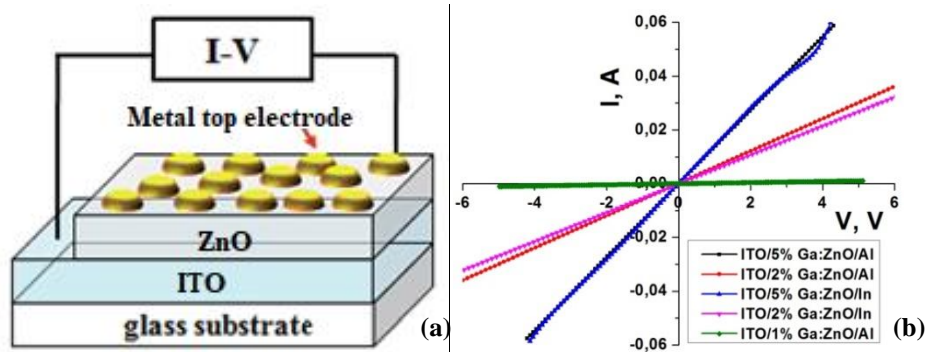
Fig. 5. Schematic representation of the fabricated glass/ITO/Ga:ZnO/Al and glass/ITO/GaZnO/In devices (a) and the dark current–voltage (I–V) characteristics of these devices (b).

The Al/ZnO and In/ZnO contacts exhibit a linear I–V variation over the voltage region ranging from −6 to 6 V, which indicates the ohmic nature of the contact. Resistivity values of the 2%Ga-doped ZnO and 5%Ga-doped ZnO thin films were determined to be 29.4 and 40.0 Ω cm, respectively. The resistivity of the 5%Ga-doped ZnO thin films is higher than that of the 2%Ga-doped films. The 1%Ga-doped film has the lowest resistivity value of all the studied films. The measured dark and illuminated I–V characteristics for the vacuum-annealed 1%Ga-doped ZnO films obtained in an Ar atmosphere are shown in Fig. 6. The wavelength of 365 nm was used for the illuminated I–V measurements. The dark current at 5 V bias voltages was 816 μA. The photocurrent under 365-nm UV light illumination was 44 mA at 5 V biases, which is obviously higher than the dark current. The UV detector operates in the photoconductive mode.
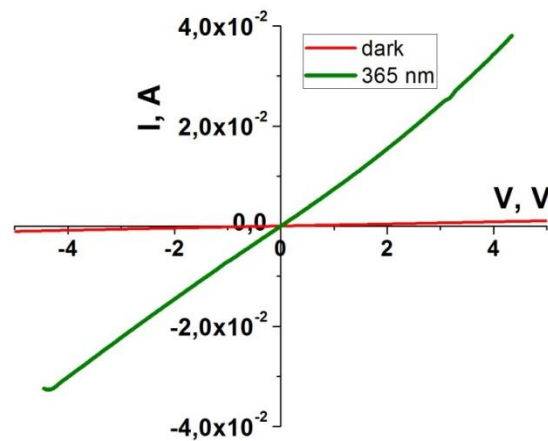

Fig. 6. Dark and illuminated I–V characteristics under 365-nm light excitation at room temperature for the vacuum-annealed ITO/Ga:ZnO/Al structure.

4. Conclusions

Nanostructured Ga-doped ZnO thin films were deposited on glass and ITO/glass substrates by spray pyrolysis in an Ar atmosphere at a substrate temperature of 450°C and then annealed at 450°C in different environments: vacuum, oxygen, and hydrogen. The key results are outlined as follows:

(1) X-ray diffraction analysis has revealed that the Ga-doped ZnO thin films have a hexagonal wurtzite phase with the preferred [0002] orientation in the case of deposition on glass substrates.

(2) X-ray diffraction analysis of Ga-doped ZnO deposited on ITO/glass substrates has shown the appearance of weak diffraction peaks corresponding to the (1002) and (1003) planes, regardless of the annealing environment type, which leads to a decrease in lattice parameter *c*.

(3) The elemental analysis has proven the presence of the Ga dopant in the structure of the 5%Ga-doped ZnO thin film. Moreover, the presence of the Ga dopant is available for all the ZnO thin films, except only for the one doped with 1%.

(4) Atomic force microscopy images of Ga-doped films deposited on ITO/glass substrates have shown a rough granular structure. The surface of the layers is affected by the nature of the annealing environment.

(5) Current–voltage characteristics have shown that the In and Al metals are good ohmic contacts for Ga-doped ZnO thin films.

(6) The UV-detection capability under 365-nm light excitation has been studied.

References

[1] U. Ozgur, Ya. I. Alivov, C. Liu, A. Teke, M. A. Reshchikov, S. Dogan, V. Avrutin, S.-J. Cho, and H. Morkoc, J. Appl. Phys. 98, 041301 (2005).

[2] Y. L. Li, D. Y. Lee, S. R. Min, H. N. Cho, J. S. Kim, and C. W. Chung, J. Appl. Phys. 47, 6896 (2008).

[3] S. Lee, S. Bang, J. Park, S. Park, W. Jeong and H. Jeon, Phys. Status Solidi 207, 1845 (2010).

[4] M. Jiang, X. Liu and H. Wang, Surf. Coat. Technol. 203, 3750 (2009).

[5] E. Vasco, C. Zaldo and L. Vázquez, J. Phys.: Condens. Matter. 13, L663 (2001).

[6] W. Mtangi, F. D. Auret, P. Janse van Rensburg, S. M. Coelho, M. J. Legodi, et al., J. Appl. Phys. 100, 094504 (2011).

[7] M. Kasuga and S. Ishihara, Jpn. J. Appl. Phys. 15, 1835 (1976).

[8] Y. S. Choi, D. K. Hwang, B. J. Kwon, J. W. Kang, Y. H. Cho, and S. J. Park, Jpn. J. Appl. Phys. 50, 10550 (2011).

[9] E. Sonmez, S. Aydin, M. Yilmaz, M. T. Yurtcan, T. Karacali, and M. Ertugrul, J. Nanomater. 2012, 950793 (2012).

[10]   M. H. Mamata, Z. Khusaimib, M. Z. Musa, M. F. Maleka, and M. Rusopa, Sens. Actuators, A 171, 241 (2011).

[11]   S.-S. Lin and J. H. Huang, Surf. Coat. Technol. 185, 222 (2004).

[12]   H. Gomez et al., Sol. Energy Mater. Sol. Cells 87, 107 (2005).

[13]   K. T. Ramakrishna Reddy, H. Gopalaswamy, and P. J. Reddy, J. Cryst. Growth 210, 516 (2000).

[14]   K. T. Ramakrishna Reddy, T. B. Reddy, and I. Forbes, Surf. Coat. Technol. 110, 151 (2002).

[15]   Y. Bessekhouad, D. Robert, and J.-V. Weber, Catal. Today 101, 315 (2005)

[16]   X. Hui-li, Z. Hui-sheng, Z.Tao, and X. Dong-chang, J. Environ. Sci. 19, 1141 (2007).

[17]   T. Prasada Rao, M. C. Santhosh Kumar, A. Safarulla, V. Ganesan, S. R. Barman, and C. Sanjeeviraja, Physica B 405, 2226 (2010).

NORMALIZED PARAMETERS OF A MAGNETORESISTIVE SENSOR IN BRIDGE CIRCUITS

Alexandr Penin[1] and Anatolie Sidorenko[1,2]

[1]D. Ghitu Institute of Electronic Engineering and Nanotechnologies, Academiei str.3/3, Chisinau, MD-2028 Republic of Moldova
[2]Technical University of Moldova, Chisinau, MD-2004 Republic of Moldova
Emails: aapenin@mail.ru,   sidorenko.anatoli@gmail.com

Abstract

Magnetoresistive sensors are considered as part of bridge circuits for measuring magnetic field strength and electric current value. Normalized or relative expressions are introduced to change the resistance of the sensor and the measured bridge voltage to increase the information content of the regime to provide the possibility of comparing the regimes of different sensors. To justify these expressions, a geometric interpretation of the bridge regimes, which leads to hyperbolic straight line geometry and a cross ratio of four points, is given. Upon a change in the sensor resistance, the bridge regime is quantified by the value of the cross ratio of four samples (three characteristic values and the current or real value) of voltage and resistance. The cross ratio, as a dimensionless value, is taken as a normalized expression for the bridge voltage and sensor resistance. Moreover, the cross ratio value is an invariant for voltage and resistance. The proposed approach considers linear and nonlinear dependences of measured voltage on sensor resistance from general positions.

Keywords: magnetoresistive sensors, bridge circuit, projective transformation, cross ratio.

Rezumat

Se analizează utilizarea senzorilor magnetorezistivi ca parte componentă a circuitelor în punte pentru măsurarea intensității câmpului magnetic și a curentului electric. Pentru a spori capacitatea informativă a regimului de lucru, a oferi posibilitatea de a compara regimurile diferitor senzori, sunt introduse expresii normalizate sau relative pentru schimbarea rezistenței senzorului și a tensiunii măsurate a punții. Pentru a fundamenta aceste expresii, se utilizează interpretarea geometrică a regimurilor de punte, ceea ce duce la geometria hiperbolică a liniei drepte și la raportul complex a patru puncte. Atunci când rezistența senzorului se schimbă, regimul de punte este determinat cantitativ de valoarea raportului complex a patru eșantioane (trei valori caracteristice și valoarea actuală) a tensiunii și rezistenței. Raportul complex, ca mărime adimensională, este luat ca expresie normalizată pentru tensiunea punții și rezistența

senzorului. În plus, valoarea raportului complex este un invariant pentru tensiune și rezistență. Abordarea propusă ia în considerare, din punct de vedere general, dependențele liniare și neliniare ale tensiunii măsurate de rezistența senzorului.

Cuvinte cheie: senzori magnetorezistivi, circuit de punte, transformare proiectivă, raport complex.

1. Introduction

Currently, magnetoresistive or spin valve sensors are commonly used to measure magnetic field strength and electric current value [1–4].

Magnetoresistive sensors are based on a number of quantum mechanical effects. Thus, the anisotropic magnetoresistive (AMR) effect is to change the electrical resistance of the ferromagnetic strips of films depending on their orientation relative to an external magnetic field. The magnetoresistive ratio is 2–3%.

Giant magnetoresistance (GMR) is observed in thin metal films consisting of alternating ferromagnetic and conducting non-magnetic layers. The effect is a significant change in the electrical resistance of this structure upon a change in the mutual direction of magnetization of neighboring magnetic layers and, accordingly, electron spins. Magnetization direction can be controlled by an external magnetic field. The device whose resistance is different for electrons with different spin directions is commonly referred to as a spin valve or a valve. It is considered to be open if magnetizations in its layers are oriented in parallel and closed in the opposite case. In most applications, the magnetoresistive ratio is 4–25%.

Tunnel magnetoresistance (TMR) is manifested by the flow of current between two layers of ferromagnets separated by a thin dielectric layer (about 1 nM). At the same time, the total resistance of the device, in which the current flows due to the tunnel effect, depends on the mutual orientation of the magnetization fields of the two magnetic layers and, accordingly, electron spins. The resistance is higher in the case of an antiparallel magnetization of layers. The magnetoresistive ratio is more than 200%.

Manufacturers offer a wide range of sensors of different types [5, 6]. A commonly used full sensor bridge circuit (four identical sensors) ensures the maximum sensitivity and linearity of the transient characteristic.

All magnetoresistive sensors listed are characterized by a typical dependence of the resistance value on the external magnetic field strength. The zero strength value corresponds to the initial resistance. Increasing the intensity in one or another direction of the magnetic field leads to an approximately linear change in the resistance. At fairly high strength values, saturation of the characteristic is manifested and the resistance of the sensor takes the minimum and, accordingly, maximum value.

If the sensor operates as part of the bridge, then the dependence of the measuring diagonal voltage on the resistance of this sensor is used [7]. In the case of a full bridge circuit (four sensors), it is necessary to ensure the opposite direction of the magnetic field for the upper and lower sensors in each branch. After that, the linear dependence of the change in the measuring diagonal voltage on the change in the resistance of the same sensors is obtained [8]. Similarly, it is obtained for a half bridge circuit, when two sensors are located in the same branch.

In the case of measuring the current value in a conductor, the opposite direction of

magnetic field is provided due to bending of this conductor [9]. This complexity of the construction is excluded in the half bridge circuit [10]. In this circuit, the sensors are located in different branches (one sensor is upper and the other is lower). However, in this case, a nonlinear (fractional linear) dependence of the change in the measuring diagonal voltage on the change in the resistance of the sensors is manifested. The same dependence is shown for a bridge with one sensor.

Thus, it was found in practice that changes in the voltage and resistance value set in kind of increments. With small changes in these values (relative to the initial resistance value) and, accordingly, the linear area of the transition characteristic, the magnetic field strength value or current value is determined. On the other hand, the characteristic values of the sensor resistance (initial, minimum, maximum) also correspond to the characteristic values of the measuring diagonal voltage. Therefore, with large changes in this voltage and resistance, it is necessary to compare the current values of these parameters with characteristic values in order to evaluate the capabilities of the regime, that is, increase its information content. Monitoring tasks now arise, namely, how to determine—in a relative form—the same current changes for different sensors or the same changes at different work points. This is important in practice if one system uses, for example, two sensors to measure the load current and voltage [11].

Generally, normalized or relative values are introduced. There is no problem with one characteristic value. Consider, for example, the simplest circuit with a voltage source, its internal resistance and variable load. In this case, the characteristic value of the load voltage will be its open circuit voltage. For the load current, the characteristic value will be the short circuit current; for the load resistance, the internal resistance of the source. The normalized values are then obtained; they make it possible to evaluate the quality or capabilities of the regime, which is important in practice. However, even in this simple circuit, a problem manifests itself. Different values of these normalized values make analysis difficult.

The considered bridge circuits relate to the electric circuits theory with variable regimes. The developed method of analyzing these circuits, which is based on projective geometry, makes it possible to solve the described problems.

2. Analysis of a Bridge Circuit with a Typical Sensor

A characteristic asymmetrical dependence of the resistance of a spin valve sensor with GMR on magnetic field strength [8] is shown in Fig. 1.

The zero strength value $H = 0$ determines the nominal R_S^0 sensor resistance. As the strength increases, the resistance decreases to saturation. In this case, saturation resistance R_S^P corresponds to the parallel case of magnetizing the sensor layers. At negative strength values, the resistance increases up to saturation. In this case, saturation resistance R_S^{AP} corresponds to the antiparallel case of magnetizing the sensor layers.
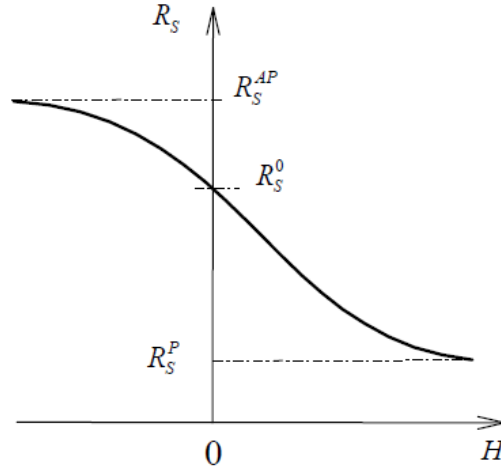
Fig. 1. Characteristic *R–H* curve of a GMR spin valve.

Magnetoresistive ratio is defined by the relative expression

$$M = \frac{R_S^{AP} - R_S^{P}}{R_S^{AP}}.$$

In the measurement practice, a linear area of characteristic is generally used. The inflection point of the characteristic most often does not correspond to the strength of $H = 0$.

Let us give the known bridge circuits [7] in Fig. 2. Reference resistances R_S^0 and the change in the resistance value ΔR are indicated in these circuits.
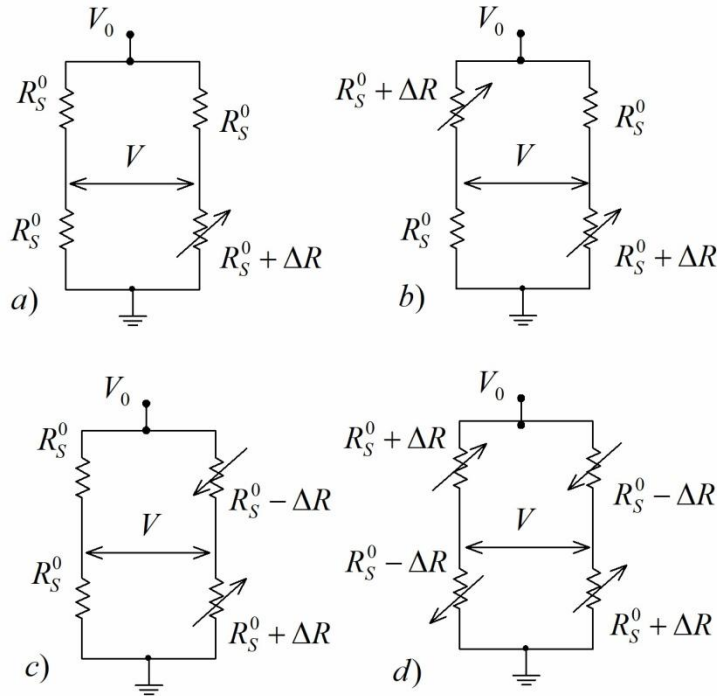
Fig. 2. Typical bridge circuits: (a) quarter bridge, (b) half bridge with unidirectional sensors, (c) half bridge with different directional sensors, and (d) full bridge.

The bridges are connected to power supply voltage sources V_0. Measuring diagonal voltages for circuits (a), (b), (c), and (d) are determined by respective expressions in Table 1.

Table 1. Measuring diagonal voltages for typical bridge circuits

Circuit (a)	Circuit (b)	Circuit (c)	Circuit (d)
$V = \dfrac{V_0}{4} \dfrac{\Delta R}{R_S^0 + \Delta R/2}$	$V = \dfrac{V_0}{2} \dfrac{\Delta R}{R_S^0 + \Delta R/2}$	$V = \dfrac{V_0}{2} \dfrac{\Delta R}{R_S^0}$	$V = V_0 \dfrac{\Delta R}{R_S^0}$

It is evident that there is a linear and fractional linear dependence of the measuring diagonal voltage on the change in the sensor resistance. In practice, linear bridges are usually used. In the case of nonlinear bridges, various schematic techniques are used to linearize the dependence.

Let us now consider the specific problems.

Case of the linear dependence of bridge voltage

We use the following measuring diagonal voltage:

$$V = \frac{V_0}{2} \frac{\Delta R}{R_S^0}. \tag{1}$$

The normalized expression is obtained at once to change the resistance ΔR relative to the reference or nominal value R_S^0. This expression provides additional or qualitative information about the current or real regime. If the change in resistance is not large and a linear area of the characteristic is used, then this is quite satisfactory in practice. However, formula (1) does not contain saturation resistances R_S^P and R_S^{AP}. Therefore, if we work in a wide area of the characteristic, this expression does not give direct information about the capabilities of the current or real measurement. Moreover, formally, we can go beyond the area of change in the sensor resistance, as shown for clarity in Fig. 3.
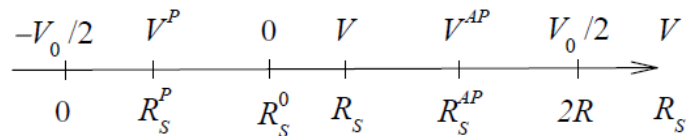

Fig. 3. Correspondence the values of the sensor resistance and voltage.

On the other hand, for these three characteristic values R_S^0, R_S^P, and R_S^{AP} of the sensor resistance, the question of a reasonable normalized expression for changing the resistance arises.

Case of the fractional linear dependence of bridge voltage

Let us present the expression of the measuring diagonal voltage for the circuit shown in Fig. 2a in the normalized form:

$$V = \frac{V_0}{2} \frac{\Delta R}{2R_S^0 + \Delta R} = \frac{V_0}{2} \frac{\Delta R / R_S^0}{2 + \Delta R / R_S^0}. \tag{2}$$

However, this formula does not contain saturation resistances R_S^P and R_S^{AP} either. Therefore, the same questions as for expression (1) and Fig. 3 arise.

3. Geometry of a Straight Line

Further, we consider some provisions about different geometries of a straight line or determining the segment length [12] according to Fig. 4.
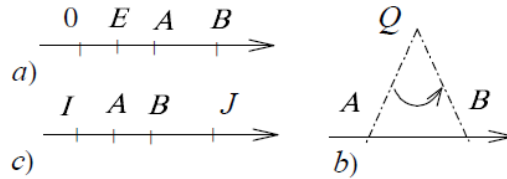

Fig. 4. Three different geometries on a straight line: (a) parabolic Euclidean (ordinary), (b) elliptical Riemann, and (c) hyperbolic Lobachevsky geometry.

For parabolic geometry, the unit of length or scale $0E$ is fixed on a straight line, and the distance d_{AB}^E between points A and B is determined by the formula

$$d_{AB}^P = \frac{AB}{0E}. \tag{3}$$

In the case of elliptical geometry, some point Q is fixed outside the straight line, and the distance is just the "normal" angle $\angle AQB$; that is,

$$d_{AB}^E = \angle AQB.$$

Hyperbolic geometry is defined in a more complex way. In addition to points A and B, two points I and J are fixed. These extreme or base points define an infinitely remote boundary or absolute as points A and B move. Next, the cross ratio (double proportion) of four points is composed:

$$m = (I\ A\ B\ J) = \frac{AI}{AJ} \div \frac{BI}{BJ}. \tag{4}$$

In this case, the distance is as follows:

$$d_{AB}^{H} = \log\left(\frac{AI}{AJ} \div \frac{BI}{BJ}\right). \tag{5}$$

If one of points A and B tends to the base point, then the cross ratio is 0 or ∞. In this case, the respective distance is $d_{AB}^{H} = \rightarrow \mu\infty$.

4. Geometric Interpretation of Bridge Regimes

The contributed short information about straight line geometry makes it possible to reasonably enter the necessary expressions.

Case of a linear dependence
According to (1), the measuring diagonal voltage corresponds to the distance of parabolic geometry (3). On the other hand, saturation resistances R_S^P and R_S^{AP} correspond to base points of hyperbolic geometry. Therefore, cross ratio (4) for the three characteristic values R_S^0, R_S^P, and R_S^{AP} of the sensor resistance and the current value R_S^1 leads to a normalized expression for changing the resistance and, accordingly, for the voltage. The cross ratio values for characteristic points are shown in Fig. 5.
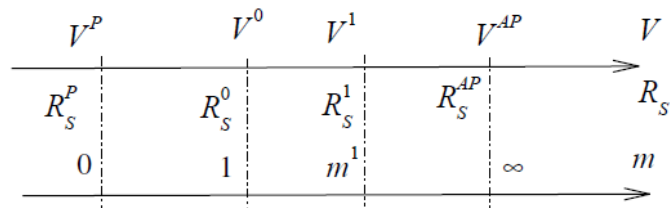

Fig. 5. Correspondence the voltage, resistance, and cross ratio values.

Cross ratio for the resistance and voltage values or samples

$$m^1 = \left(R_S^P \ R_S^1 \ R_S^0 \ R_S^{AP}\right) = \frac{R_S^1 - R_S^P}{R_S^1 - R_S^{AP}} \div \frac{R_S^0 - R_S^P}{R_S^0 - R_S^{AP}} =$$

$$\left(V^P \ V^1 \ V^0 \ V^{AP}\right) = \frac{V^1 - V^P}{V^1 - V^{AP}} \div \frac{V^0 - V^P}{V^0 - V^{AP}}. \tag{6}$$

Thus, when a sensor resistance varies from a minimum to maximum value (base values), a bridge regime is quantified by cross ratio value m. Thus, we get additional information about the capabilities of the regime and its qualitative characteristics. A cross ratio is a dimensionless value; therefore, it can be assumed that the m value is the normalized expression for the bridge voltage and sensor resistance, where all characteristic values are used. In other words, the dimensionless coordinate of a resistance value R_S^1 on a straight line relative to an initial value R_S^0 is determined by cross ratio (6) or respective distance (5).

Case of a fractional linear dependence

Let a current or initial value of the sensor resistance correspond to $R_S^1 = R_S^0 + \Delta R$. In this case, expression (2) takes the form

$$V^1(R_S^1) = \frac{V_0}{2} \frac{\Delta R}{2R_S^0 + \Delta R} = \frac{V_0}{2} \frac{R_S^1 - R_S^0}{R_S^1 + R_S^0}. \tag{7}$$

This fractional linear expression represents a projective transformation $R_S^1 \rightarrow V^1$ in the sense of projective geometry in Fig. 6. Let us apply the projective geometry method [13] to analyze a bridge with a fractional linear dependence.

The points of the resistance axis are projected onto the voltage axis from point P as the projection center. It is evident that the proportions of the segment lengths on these axes are broken. On the other hand, there is a value that is retained for this projection. This value or invariant of the transformation is a cross ratio, similar to (6), of respective four points or samples of the resistance and voltage.
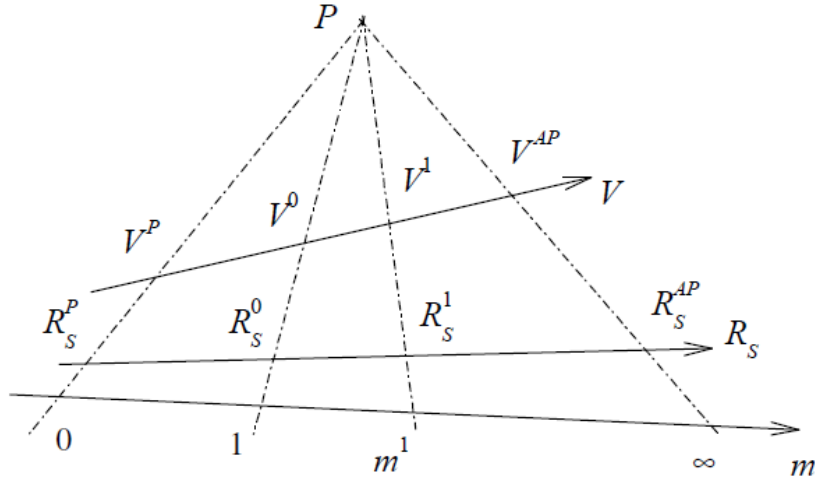

Fig. 6. Projective transformation $R_S^1 \rightarrow V^1$ defines the cross ratio value m.

Thus, this case, which is more general, corresponds to the discussed linear dependence if the projection center $P \rightarrow \infty$. In this case, the projection of points of the resistance axis onto the voltage axis is carried out by parallel lines. Next, we will consider both cases from a common perspective.

Change of the bridge regime

Let the subsequent value of the sensor resistance correspond to R_S^2 and determine the respective voltage value V^2. In this case, the subsequent cross ratio value is as follows:

$$m^2 = \left(V^P \ V^2 \ V^0 \ V^{AP}\right) = \frac{V^2 - V^P}{V^2 - V^{AP}} \div \frac{V^0 - V^P}{V^0 - V^{AP}},$$

$$m^2 = \left(R_S^P \ R_S^2 \ R_S^0 \ R_S^{AP}\right) = \frac{R_S^2 - R_S^P}{R_S^2 - R_S^{AP}} \div \frac{R_S^0 - R_S^P}{R_S^0 - R_S^{AP}}.$$

The cross ratio has a group property if a subsequent m^2 value is expressed relative to an initial m^1 value through its change m^{21} by a group operation (addition or multiplication). The expression structure shows the execution of the group multiplication operation:

$$m^2 = m^{21} \cdot m^1.$$

Next, we introduce the regime change m^{21} by the cross ratio

$$m^{21} = m^2 \div m^1 = \left(\frac{R_S^2 - R_S^P}{R_S^2 - R_S^{AP}} \div \frac{R_S^0 - R_S^P}{R_S^0 - R_S^{AP}} \right) \div \left(\frac{R_S^1 - R_S^P}{R_S^1 - R_S^{AP}} \div \frac{R_S^0 - R_S^P}{R_S^0 - R_S^{AP}} \right) =$$

$$\frac{R_S^2 - R_S^P}{R_S^2 - R_S^{AP}} \div \frac{R_S^1 - R_S^P}{R_S^1 - R_S^{AP}} = \left(R_S^P \ R_S^2 \ R_S^1 \ R_S^{AP} \right), \tag{8}$$

$$m^{21} = \left(V^P \ V^2 \ V^1 \ V^{AP} \right) = \frac{V^2 - V^P}{V^2 - V^{AP}} \div \frac{V^1 - V^P}{V^1 - V^{AP}}. \tag{9}$$

The structure of cross ratio (9) shows the mutual reduction of possible additive and multiplicative errors of measurement of voltage samples.

Next, knowing the V^2, V^1 voltage values, we find the regime change (9) and calculate the subsequent resistance value by (8)

$$R_S^2 = \frac{R_S^1 (m^{21} R_S^{AP} - R_S^P) - (m^{21} - 1) R_S^{AP} R_S^P}{R_S^1 (m^{21} - 1) - (m^{21} R_S^P - R_S^{AP})}. \tag{10}$$

The obtained transformation translates an initial point R_S^1 to a subsequent point R_S^2. The transformation parameter m^{21} forms a segment of invariable "length," and we observe the movement of this segment in Fig. 7.
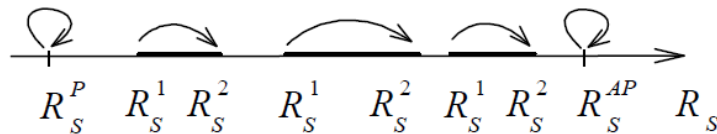

Fig. 7. Hyperbolic projective transformation determines the moving of a segment of invariable length.

Here, the change in the usual length is visible. For the base fixed points R_S^P, R_S^{AP}, this length is decreasing to zero. Let the initial point $R_S^1 = R_S^P$. In this case, the subsequent point

$$R_S^2 = \frac{R_S^P(m^{21}R_S^{AP} - R_S^P) - (m^{21} - 1)R_S^{AP}R_S^P}{R_S^P(m^{21} - 1) - (m^{21}R_S^P - R_S^{AP})} = \frac{-R_S^P R_S^P + R_S^{AP}R_S^P}{-R_S^P + R_S^{AP}} = R_S^P.$$

Similarly, if $R_S^1 = R_S^{AP}$, then $R_S^2 = R_S^{AP}$. Expression (10) and Fig. 7 show how to set the same changes at different initial or work points, compare regimes of different sensors, etc.

The described approach provides the basis for consideration of symmetric characteristics $R(H)$ [6], in particular, for superconducting spin valves [14].

5. Conclusions

(i) The geometric method provides a general approach for determining and comparing the regime of different bridge circuits in a normalized or relative form.

(ii) Normalized mode parameter expressions include all the characteristic regime values.

(iii) The proposed invariant expressions in the form of a cross ratio represent a qualitative estimate of the real regime and exclude a variety of different values of the regime parameters.

(iv) Additive and multiplicative errors of measurement of voltage samples are mutually reduced for the cross ratio.

References

[1] E. G. Vidal, D. R. Muñoz, S. I. Arias, J. S. Moreno, S. Cardoso, R. Ferreira, and P. Freitas, Materials 10 (10), 1134 (2017).

[2] S. Zuo, K. Nazarpour, and H. Heidari, IEEE Electron Device Lett. 39 (11), 1784 (2018).

[3] S. J. Nibir, H. Niakan, and B. Parkhideh, Characterization of magnetoresistors for contactless current sensing in power electronic applications, in 2017 IEEE Energy Conversion Congress and Exposition (ECCE), IEEE, 2017, pp. 433–438.

[4] C. Musuroi, M. Oproiu, M. Volmer, and I. Firastrau, Sensors 20 (1), 323 (2020).

[5] TMR Current Sensors, http://www.dowaytech.com/en/1394.html

[6] Magnetic Sensors, https://www.nve.com/sensors.php

[7] Practical Design Techniques for Sensor Signal Conditioning, Ed. by W. Kester, Analog Devices Inc. USA, Prentice Hall, Upper Saddle River (NJ), 1999, p. 366.

[8] Y. H. Su, C. C. Lu, J. T. Jeng, J. H. Hsu, M. Y. Liao, J. C. Wu, and C. R. Chang, IEEE Trans. Nanotechnol. 17 (1), 11 (2017).

[9] R. Mattheis, M. Diegel, and R. Weiss, IEEE Trans. Magnet. 52 (10), 1 (2016).

[10] J. T. Jeng, X. T. Trinh, C. H. Hung, and C. C. Lu, Sensors, 19 (8), 1882 (2019).

[11] J. G. Deak, I. Jin, W. Shen, and S. Xue, Patent US 9,341,686 B2, May 17 (2016).

[12] I. M. Yaglom, A Simple Non-Euclidean Geometry and Its Physical Basis: An Elementary Account of Galilean Geometry and the Galilean Principle of Relativity, Springer Science & Business Media, Berlin, 2012, p. 303.

[13] A. Penin, Analysis of Electrical Circuits with Variable Load Regime Parameters: Projective Geometry Method, 3rd ed., Springer International Publishing, Cham, Switzerland, 2020, p. 520.

[14] V. I. Zdravkov, D. Lenk, R. Morari, A. Ullrich, G. Obermeier, C. Müller, and L. R. Tagirov, Appl. Phys. Lett. 103 (6), 062604 (2013).